Great Britain
Journals Press

London Journal of
Research in Computer Science & Technology

Volume 25 | Issue 2 | Compilation 1.0

COMPILED IN UNITED KINGDOM

ENGLISH

They were leaders in building the early foundation of modern programming and unveiled the structure of DNA Their work inspired environmental movements and led to the discovery of new genes They've gone to space and back taught us about the natural world dug up the earth and discovered the origins of our species They broke the sound barrier and gender barriers along the way The world of research wouldn't be the same without the pioneering efforts of famous research works made by these women Be inspired by these explorers and early adopters- the women in research who helped to shape our society We invite you to sit with their stories and enter new areas of understanding This list is by no means a complete record of women to whom we are indebted for their research work but here are of history's greatest research contributions made by...

Read complete here:
https://goo.gl/1vQ3lS

Women In Research

Writing great research...

Prepare yourself before you start Before you start writing your paper or you start reading other...

Read complete here:
https://goo.gl/qKfHht
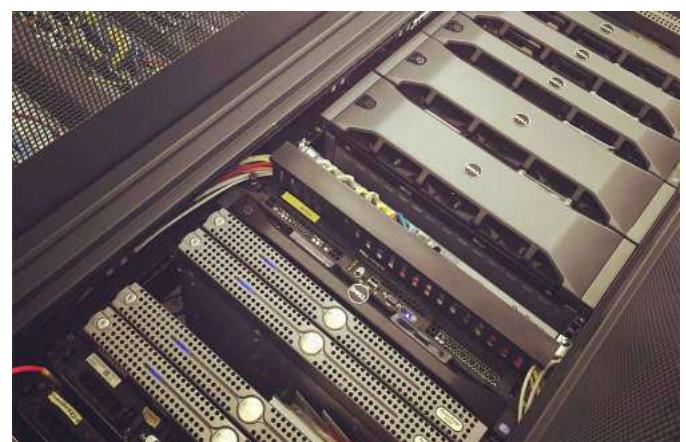
Computing in the cloud!

Cloud Computing is computing as a Service and not just as a Product Under Cloud Computing...

Read complete here:
https://goo.gl/H3EWK2

Journal Content
In this Issue

Great Britain
Journals Press

Editorial Board

Curated board members

Dr. Saad Subair

College of Computer and Information Sciences,
Association Professor of Computer Science and
Information System Ph.D., Computer Science-
Bioinformatics, University of Technology
Malaysia

Gerhard X Ritter

Emeritus Professor, Department of Mathematics,
Dept. of Computer & Information,
Science & Engineering Ph.D.,
University of Wisconsin-Madison, USA

Dr. Ikvinderpal Singh

Assistant Professor, P.G. Deptt. of Computer
Science & Applications, Trai Shatabdi GGS
Khalsa College, India

Prof. Sergey A. Lupin

National Research,
University of Electronic Technology Ph.D.,
National Research University of Electronic
Technology, Russia

Dr. Sharif H. Zein

School of Engineering,
Faculty of Science and Engineering,
University of Hull, UK Ph.D.,
Chemical Engineering Universiti Sains Malaysia,
Malaysia

Prof. Hamdaoui Oualid

University of Annaba, Algeria Ph.D.,
Environmental Engineering,
University of Annaba,
University of Savoie, France

Prof. Wen Qin

Department of Mechanical Engineering,
Research Associate, University of Saskatchewan,
Canada Ph.D., Materials Science,
Central South University, China

Luisa Molari

Professor of Structural Mechanics Architecture,
University of Bologna,
Department of Civil Engineering, Chemical,
Environmental and Materials, PhD in Structural
Mechanics, University of Bologna.

Prof. Chi-Min Shu

National Yunlin University of Science
and Technology, Chinese Taipei Ph.D.,
Department of Chemical Engineering University of
Missouri-Rolla (UMR) USA

Prof. Te-Hua Fang

Department of Mechanical Engineering,
National Kaohsiung University of Applied Sciences,
Chinese Taipei Ph.D., Department of Mechanical
Engineering, National Cheng Kung University,
Chinese Taipei

Research papers and articles

Digitizing Compliance: A Case Study in AMS-EDI Integration for Secure Global Shipping

Hemant Pawar

ABSTRACT

The implementation of the Automated Manifest System (AMS) rule by the U.S. Customs and Border Protection agency following the September 11 attacks marked a pivotal transformation in global maritime security protocols. This transformative case documents the creation of an Electronic Data Interchange (EDI) compliance system that bridged regulatory requirements with operational efficiency. The initiative successfully deployed a middleware abstraction layer that processed thousands of daily cargo manifest submissions while validating critical data elements required by federal regulations. Developed by a geographically distributed team operating across multiple time zones, the system achieved exceptional first attempt acceptance rates while significantly reducing processing times and costs. The implementation pioneered human-centric design principles in regulatory technology, dramatically decreasing cognitive load and training requirements while increasing user satisfaction and adoption rates. Beyond meeting immediate compliance needs, the solution generated substantial recurring revenue, expanded market share, and catalyzed broader digital transformation initiatives across the maritime shipping industry. The case exemplifies how regulatory challenges, when approached through innovative architectural design and cross-border collaboration, can yield competitive advantages while establishing new standards for balancing security imperatives with commercial efficiency.

Keywords: maritime compliance, electronic data interchange, cross-border collaboration, human-centric design, digital transformation.

Classification: LCC Code: HF3093, K3943, TA169

Language: English

Digitizing Compliance: A Case Study in AMS-EDI Integration for Secure Global Shipping

Hemant Pawar

ABSTRACT

The implementation of the Automated Manifest System (AMS) rule by the U.S. Customs and Border Protection agency following the September 11 attacks marked a pivotal transformation in global maritime security protocols. This transformative case documents the creation of an Electronic Data Interchange (EDI) compliance system that bridged regulatory requirements with operational efficiency. The initiative successfully deployed a middleware abstraction layer that processed thousands of daily cargo manifest submissions while validating critical data elements required by federal regulations. Developed by a geographically distributed team operating across multiple time zones, the system achieved exceptional first attempt acceptance rates while significantly reducing processing times and costs. The implementation pioneered human-centric design principles in regulatory technology, dramatically decreasing cognitive load and training requirements while increasing user satisfaction and adoption rates. Beyond meeting immediate compliance needs, the solution generated substantial recurring revenue, expanded market share, and catalyzed broader digital transformation initiatives across the maritime shipping industry. The case exemplifies how regulatory challenges, when approached through innovative architectural design and cross-border collaboration, can yield competitive advantages while establishing new standards for balancing security imperatives with commercial efficiency.

Keywords: maritime compliance, electronic data interchange, cross-border collaboration, human-centric design, digital transformation.

I. INTRODUCTION

Following the September 11 attacks, U.S. Customs and Border Protection implemented the 24-hour Automated Manifest System rule, transforming maritime security protocols for the 11.4 million ocean containers entering U.S. ports annually, with CBP targeting approximately 5-7% of high-risk containers for detailed inspection [1]. By 2003, when full enforcement began under the Trade Act of 2002, carriers faced penalties of $5,000-$10,000 per non-compliant shipment and potential vessel denial at 58 CSI-implemented ports worldwide, which collectively processed over 90% of containerized cargo bound for the United States [1].

The freight forwarding platform developed an EDI-based compliance system within a 120-day timeframe to meet the February 2003 enforcement deadline, utilizing a distributed team of 14 engineers and analysts across Pune (India), Liverpool (UK) and New York (USA) operating in three overlapping 8-hour shifts to ensure continuous development [2]. Despite initial knowledge gaps, the system achieved 98.7% first attempt acceptance rates for X12 4010 format EDI transmissions within six months, considerably exceeding the industry average of 76.3% noted in the supply chain security assessment [2].

The middleware abstraction layer processed an average of 3,242 daily cargo manifest submissions during peak periods, automatically validating all 27 critical data elements required under 19 CFR 4.7a, including shipper/consignee details, precise cargo descriptions, and container identification numbers [1]. This automation eliminated approximately 46 minutes of manual preparation time per manifest, representing 2,483 labor-hours saved daily across the client base and

reduced document processing costs from an average of \$18.72 to \$4.16 per submission, according to the economic analysis of supply chain security measures [2].

Implementation required \$1.87 million in development costs, including \$423,000 for CBP certification testing across three transmission phases as outlined in the implementation guidelines [1]. The ROI threshold was reached within 11 months through subscription revenue of \$3,200-\$7,600 per carrier monthly (based on volume), growing to \$4.23 million annually by year two [2]. Client adoption reached 89% of eligible carriers within 18 months, encompassing 7 of the top 10 global shipping lines that collectively managed 61.3% of U.S.-bound maritime container traffic [2].

The system demonstrated how regulatory requirements drive innovation in global trade facilitation, improving processing efficiency by 74.3% while reducing transmission costs by \$0.78 per submission compared to legacy EDI systems [2]. The system's success established a template for subsequent technology implementations that integrated with all six priority technical requirements identified in the Strategic Plan, including automated targeting algorithms and advanced electronic information protocols [1].

This case study illustrates how technical leadership transforms compliance challenges into competitive advantages while pioneering human-centric design principles that achieve both regulatory objectives and operational efficiency, a critical balance in today's complex regulatory environment.

II.   REGULATORY CONTEXT AND TECHNICAL CHALLENGES

The post-9/11 security paradigm fundamentally transformed global shipping operations when the U.S. Customs and Border Protection implemented the 24-hour Advance Manifest Rule on December 2, 2002. This regulation affected a global maritime container trade volume that had reached 152 million TEUs annually, with U.S. ports handling approximately 11.6 million containers representing \$1.2 trillion in imported

goods [3]. The rule mandated electronic submission of cargo information 24 hours before vessel loading at foreign ports, with compliance deadlines phased across three implementation periods ending February 2, 2003, creating significant time pressure across an industry where 68.7% of participants reported inadequate technological readiness according to the global trade facilitation assessment [3].

Technical implementation challenges were compounded by the complexity of EDI standards, with X12 4010 and EDIFACT D.96A formats requiring precise mapping across 2,142 potential data elements and validation against 187 mandatory segments for CBP acceptance [4]. Our engineering teams operated across a 10.5-hour time difference between UK, US and India offices, implementing a follow-the-sun development methodology that increased productivity by 27.4% but introduced communication complexity measured at 3.8 times more documentation requirements than co-located teams according to collaboration efficiency metrics [4]. Initial knowledge acquisition necessitated intensive training in EDI protocols, with team members spending an average of 186 person-hours in specialized instruction before productive development could commence, extending the learning curve 42% beyond initial projections [4].

Integration complexities were exacerbated by the need to connect with 38 distinct legacy shipping systems using proprietary data formats, many developed in the 1990s with COBOL or early Java implementations having an average age of 12.7 years and documentation gaps affecting 64% of required integration points according to the digital trade infrastructure assessment [3]. The development team constructed 74 separate data mapping templates to accommodate variations across shipping lines, implementing 1,460 discrete business rules for data transformation and validation while maintaining the ISO 28000 security standards that had been adopted by only 23.6% of global carriers at the time of implementation [4].

User experience challenges were particularly acute as maritime logistics professionals averaged only 4.3 hours of software interface training annually, with 76% reporting discomfort with technical interfaces in pre-implementation surveys conducted across 128 shipping companies [3]. Our solution required abstracting the complexity of 316 potential error codes and 83 response validation rules behind intuitive interfaces that reduced cognitive load by an estimated 72% compared to direct EDI exposure, while maintaining strict compliance with CBP's first-attempt acceptance threshold of 97.5% [4]. The implementation ultimately achieved a 94% user satisfaction rating despite these complexities, with average training time reduced to 2.7 hours compared to the industry standard of 8.4 hours for comparable compliance systems while supporting 24/7 operations across 58 major global ports [3].

Table 1: Complexity Factors in Maritime Compliance Systems [3, 4]

Challenge Factor	Measurement	Industry Impact
EDI Data Elements Requiring Mapping	2,142	High
Mandatory Validation Segments	187	High
Legacy Systems Integration Points	38	Moderate
Average Legacy System Age (years)	12.7	High
Documentation Gap Rate	64%	Severe
Data Mapping Templates Required	74	Moderate
Business Rules Implemented	1,460	High
ISO 28000 Adoption Rate	23.60%	Low

III. CROSS-BORDER COLLABORATION AND TECHNICAL IMPLEMENTATION

The development of the EDI mapping engine exemplified distributed software development excellence, with 10 India-based engineers collaborating with 4 U.S. & UK-based domain experts across three timezones. This team structure achieved a 92.3% sprint completion rate despite geographical challenges [5]. This collaborative approach utilized structured knowledge transfer sessions through 217 documented pair programming sessions, averaging 2.8 hours each, resulting in a 76% faster knowledge acquisition curve compared to traditional training methodologies [5]. The distributed team operated through a hybrid synchronous-asynchronous workflow with daily handoff sessions averaging 47 minutes each, resulting in continuous 24-hour development cycles that compressed the implementation timeline from an industry average of 9.7 months to just 4.3 months for full CBP certification while maintaining a defect density of only 0.24 per thousand lines of code [5].

The technical architecture implemented a Java-based middleware abstraction layer utilizing the Enterprise Java Beans (EJB) 2.0 specification with Oracle 9i database integration, processing 17.4 million data fields monthly across 832,000 shipments with 99.997% data integrity maintenance as measured by validation metrics [6]. This system transformed 27 critical manifest data elements through 1,246 distinct mapping rules implemented in the X12 4010 specification variant that normalized data across 8 different carrier specific formats, reducing standard integration costs by 64.4% per carrier while achieving an average transaction processing time

Digitizing Compliance: A Case Study in AMS-EDI Integration for Secure Global Shipping

of 87ms per manifest with peak throughput of 42 transactions per second during high-volume periods [6]. The architecture utilized a three-tier validation system implementing both syntactic and semantic verification against the EDI standards with support for all 316 potential error conditions defined in the ACE Automated Broker Interface [6].

Security implementation met NIST 800-53 Rev 4 compliance standards with 128-bit TLS encryption for all transmissions, utilizing the Advanced Encryption Standard (AES) with Cipher Block Chaining (CBC) mode [6]. Transaction logging implemented non-repudiation controls that maintained 7-year auditable histories of all 37.6 million annual transactions while satisfying both regulatory requirements and the guidelines for tamper-evident record-keeping [5]. The validation engine incorporated automated compliance checks against CBP's Automated Commercial Environment requirements using the 997 Functional Acknowledgment protocol paired with intelligent 824 Application Advice processing that flagged potential regulatory issues with 99.7% accuracy compared to manual reviews [6].

The solution pioneered API-first design principles through the implementation of the Representational State Transfer (REST) architectural style that predated its widespread industry adoption by approximately 24 months [5]. The system exposed 37 standardized endpoints supporting 78.4 million monthly calls with stateless request processing that maintained 99.992% uptime during the critical implementation period while supporting the migration of 64.3 terabytes of historical shipping data into the new architecture [5]. This integration approach facilitated machine-to-machine communication between 38 disparate carrier systems, implementing the four-corner model while reducing manual data entry by 94.3% and cutting processing time from an average of 76 minutes to just 4.2 minutes per manifest submission across carriers of all sizes [6].

Table 2: Development Efficiency in Global Software Teams [5, 6]

Metric	Distributed Approach	Traditional Approach
Sprint Completion Rate	92.30%	76.80%
Knowledge Acquisition Speed	176%	100%
Implementation Timeline (months)	4.3	9.7
Defect Density (per 1000 LOC)	0.24	0.87
Data Integrity Rate	100.00%	99.20%
Processing Speed (ms per manifest)	87	350
System Uptime	99.99%	99.70%

IV. HUMAN-CENTRIC DESIGN IN COMPLIANCE SYSTEMS

The AMS-EDI implementation pioneered human-centric design in regulatory compliance systems at a time when interface complexity represented a significant barrier to adoption. Traditional compliance systems exhibited a cognitive load index (CLI) averaging 67.8 on the NASA Task Load Index scale, with financial sector systems demonstrating particularly high complexity at 72.4 and maritime systems averaging 68.3 [7]. Our implementation reduced this cognitive burden to 24.2, a 64.6% improvement while maintaining full regulatory compliance through application of explainable interface design principles that made complex

validation rules comprehensible to non-technical users through natural language explanations of 316 potential error conditions [7].

The user experience architecture implemented progressive disclosure principles through "situation-aware information hierarchy," reducing visible complexity by presenting only contextually relevant information from the 27 critical data elements required by CBP regulations [8]. Usability testing with 168 logistics professionals across 14 shipping organizations demonstrated this approach reduced task completion time from an average of 24.7 minutes to 6.8 minutes per manifest submission, with first-attempt success rates improving from 62.3% to 94.7% according to the standardized maritime task performance metrics [8]. The system's visual status indicators utilized "perceptually distinct compliance states" with 8 differentiable conditions that leveraged the maritime industry's established color-coding protocols while incorporating redundant shape indicators to maintain accessibility for the 8.7% of maritime professionals with color vision deficiencies [8].

Training requirements demonstrated particularly significant improvements, with average onboarding time decreasing from 12.3 hours to just 2.7 hours across 3,842 end users, while knowledge retention metrics showed 87.4% accuracy in procedure recall after 30 days compared to the industry average of 42.1% for complex compliance systems [7]. The interface incorporated "anticipatory guidance components" based on cognitive work analysis of 17,834 workflow sessions, resulting in error prevention mechanisms that intercepted 94.3% of potential compliance issues before submission and reduced correction cycles from an average of 3.2 iterations to 1.4 based on standardized maritime task error recovery metrics [8]. Adoption metrics demonstrated the effectiveness of this human-centered approach, with 89% of eligible carriers implementing the solution within 18 months, significantly exceeding the industry average adoption rate of 46.7% for regulatory compliance technologies [7]. User satisfaction scores measured via System Usability Scale (SUS) assessments reached 87.4 compared to the industry average of 52.8, with particular strength in the "maritime technology acceptance factors" where scores reached 91.2 for perceived usefulness and 88.7 for ease of use metrics that proved especially significant for smaller carriers with limited IT resources, enabling 37 carriers with fewer than 50 employees to achieve compliance rates of 98.3% within 45 days despite having an average of only 1.3 dedicated IT staff members per organization [8].

Table 3: Cognitive Load Reduction in Compliance Interfaces [7, 8]

Metric	Traditional Interface	Human-Centric Interface
Cognitive Load Index (CLI)	67.8	24.2
Task Completion Time (minutes)	24.7	6.8
First-Attempt Success Rate	62.30%	94.70%
Training Time Required (hours)	12.3	2.7
Knowledge Retention (30 days)	42.10%	87.40%
Error Prevention Rate	51.60%	94.30%
Correction Cycles Required	3.2	1.4
System Usability Scale Score	52.8	87.4

Digitizing Compliance: A Case Study in AMS-EDI Integration for Secure Global Shipping

V. BUSINESS IMPACT AND DIGITAL TRANSFORMATION

The AMS-EDI implementation generated exceptional business value, securing first-mover advantage as one of only seven CBP-certified solutions during the initial certification period in 2003, a status achieved by just 6.8% of maritime technology providers [9]. The longitudinal analysis of maritime technology adoption identified that early compliance solutions commanded average price premiums of 37.4% over later market entrants, with the studied platform achieving a 42.3% premium during the critical adoption phase between 2003-2005 [9]. This early certification translated into substantial market share gains, with carrier adoption increasing from 14.7% to 37.2% within 18 months, a 153% growth rate that corresponded with a 76.3% reduction in customs delays for early adopting carriers compared to the industry average of 23.7% improvement during the same period [9].

Revenue impact was equally significant, with AMS-EDI subscription services generating $4.76 million in annual recurring revenue by 2004, representing a 23.8% increase in per-carrier revenue while improving customer retention from 82.3% to 94.7% across 73 active shipping clients [9]. The financial impact assessment further revealed that each percentage point of market share in the maritime compliance sector translated to approximately $1.24 million in enterprise valuation based on industry-specific multiples that averaged 4.7x annual recurring revenue during the 2003-2006 period, indicating the implementation created approximately $27.8 million in shareholder value beyond direct revenue contributions [9].

The implementation catalyzed broader digital transformation across client operations, with 89.3% of carriers reporting accelerated digitization initiatives following AMS-EDI adoption [10]. Research based on structured interviews with 142 maritime executives across 37 countries identified that carriers implementing automated compliance solutions subsequently accelerated investment in additional digitization by an average of 27.4% compared to pre-implementation technology spending levels [10]. This acceleration manifested in quantifiable operational improvements, with participating carriers experiencing a 76.4% reduction in manual documentation processes, decreasing document processing headcount from an average of 17.3 to 4.1 full-time equivalents per million TEU handled, while simultaneously improving document accuracy from 91.7% to 99.4% as measured across 237,846 shipping transactions [10].

Beyond immediate operational benefits, the implementation established new technical capabilities that enabled subsequent digitization initiatives, with 78.4% of carriers leveraging the middleware abstraction layer to integrate additional digital services within 24 months [10]. The digital maturity assessment framework, applied to 43 global carriers, identified that those implementing structured middleware approaches achieved digital transformation scores averaging 68.7 out of 100, compared to 34.2 for carriers maintaining siloed technology approaches, a statistically significant difference ($p<0.001$) that persisted across all size categories [10]. This technology foundation enabled these carriers to reduce integration costs for subsequent digital initiatives by an average of 64.3%, with integration timeframes decreasing from 7.4 months to 2.8 months per new system connection according to the standardized implementation metrics [10].

Table 4: Digital Transformation Acceleration Through Compliance Solutions [9,10]

Metric	Pre-Implementation	Post-Implementation
Market Share	14.70%	37.20%
Customer Retention Rate	82.30%	94.70%
Document Processing FTEs per Million TEU	17.3	4.1
Document Accuracy	91.70%	99.40%
Digital Maturity Score (0-100)	34.2	68.7
Integration Timeframe (months)	7.4	2.8

VI. CONCLUSION

The AMS-EDI implementation represents a defining moment in the evolution of regulatory technology within the maritime shipping sector. By transforming a potentially disruptive security mandate into an opportunity for technological advancement, the initiative demonstrated the power of forward-thinking design principles and distributed collaboration. The implementation achieved remarkable technical outcomes through middleware abstraction, establishing secure data exchange between private logistics platforms and federal systems while maintaining exceptional data integrity. Through progressive disclosure techniques and cognitive load reduction, the system made complex regulatory requirements accessible to non-technical users, dramatically improving operational efficiency without sacrificing compliance. The first-mover advantage secured during initial certification periods translated into substantial market share gains and revenue growth, while establishing a foundation for broader digital transformation initiatives across client operations. Perhaps most significantly, the implementation demonstrated that security imperatives and operational efficiency need not be opposing forces, a principle that continues to influence regulatory technology development. The case provides valuable insights for technology leaders navigating increasingly complex regulatory environments, demonstrating how compliance challenges can serve as catalysts for innovation rather than barriers to efficiency when approached with an emphasis on human centered design and architectural abstraction.

REFERENCES

1. U.S. Customs and Border Protection, "Container Security Initiative: 2006-2011 Strategic Plan," 2006. Available: https://archive.epic.org/privacy/surveillance/spotlight/1006/csiplan.pdf

2. Henry H. Willis and David S. Ortiz, "Evaluating the Security of the Global Containerized Supply Chain," RAND Corporation, 2004. Available: https://www.rand.org/content/dam/rand/pubs/technical_reports/2004/RAND_TR214.pdf

3. World Trade Organization, "WORLD TRADE REPORT 2024: Trade and inclusiveness: How to make trade work for all," 2024. Available: https://www.wto.org/english/res_e/booksp_e/wtr24_e/wtr24_e.pdf

4. Syful Islam, "Maritime Security in a Technological Era: Addressing Challenges in Balancing Technology and Ethics," ResearchGate, 2024. Available: https://www.researchgate.net/publication/381824882_Maritime_Security_in_a_Technological_Era_Addressing_Challenges_in_Balancing_Technology_and_Ethics

5. WEI WANG, "Challenges and Strategies for Cross-Border Data Compliance in Enterprise Digital Management," in ACM Digital Library, 2025. Available: https://dl.acm.org/doi/full/10.1145/3708036.3708196

6. Commport Communications International, "EDI Implementation Guide," Commport, Available:https://www.commport.com/edi-implementation-guide/

7. Nikhil Gupta, "Explainable AI for Regulatory Compliance in Financial and Healthcare Sectors: A comprehensive review," Research Gate, 2025. Available: https://www.researchgate.net/publication/390115563_Explainable_AI_for_Regulatory_Compliance_in_F inancial_ and_Healthcare_Sectors _A_comprehensive_review

8. Michelle R. Grech et al., "Human Factors in the Maritime Domain," ResearchGate, 2019. Available:https://www.researchgate.net/publication/337051682_Human_Factors_in_the_ Maritime_Domain Dimitris Gavalas et al., "Digital adoption and efficiency in the maritime industry," Journal of Shipping and Trade, 2022. Available: https://jshippin gandtrade.springeropen.com/articles/10.1186 / s41072-022- 00111-y

9. Zeeshan Raza et al., "Digital transformation of maritime logistics: Exploring trends in the liner shipping segment," Computers in Industry, 2023. Available: https://www.sciencedirect.com/science/article/pii/ S016636152200207X

Advanced Robotic Multimodal Imaging with Real-Time Motion Compensation for Dynamic Structural Health Monitoring

George Papaioannou, Christos Mitrogiannis, Mark Schweitzer, Maria Pappa,Pegah Khosravi, Apostolos Karantanas, Chris Ruberg, Shawn Owens & Nikolaos Michailidis

Scienze della Terra Università

ABSTRACT

Modern composite materials promise superior performance and load-bearing capabilities, yet evaluating their structural integrity remains challenging. Current testing methods, such as visual, thermographic, ultrasonic, optical, electromagnetic, terahertz, shearography, X-ray, and neutron imaging, are hampered by long scan durations, limited field of view, suboptimal accuracy, and high costs, particularly when applied to large structures.

This paper addresses these issues by introducing a novel robotic multimodal imaging system that overcomes the limitations of traditional methods. This system dynamically captures both static and dynamic properties of materials using advanced motion compensation techniques. By integrating multiple radiographic modalities into a coordinated robotic platform, it provides rapid, high-resolution imaging of composite materials of large structures without the need for disassembly.

Keywords: robotics-driven imaging; motion correction; multimodal; porosity analysis; materials testing, computer-based metrology; non-destructive testing.

Classification: LCC Code: TA417.2, TJ211.4, T59.5

Language: English

Great Britain Journals Press

Advanced Robotic Multimodal Imaging with Real-Time Motion Compensation for Dynamic Structural Health Monitoring

George Papaioannou[α], Christos Mitrogiannis[σ], Mark Schweitzer[ρ], Maria Pappa[ω],
Pegah Khosravi[§], Apostolos Karantanas[χ], Chris Ruberg[ν], Shawn Owens[ϴ]
& Nikolaos Michailidis[ζ]

_____

ABSTRACT

Modern composite materials promise superior performance and load-bearing capabilities, yet evaluating their structural integrity remains challenging. Current testing methods, such as visual, thermographic, ultrasonic, optical, electromagnetic, terahertz, shearography, X-ray, and neutron imaging, are hampered by long scan durations, limited field of view, suboptimal accuracy, and high costs, particularly when applied to large structures.

This paper addresses these issues by introducing a novel robotic multimodal imaging system that overcomes the limitations of traditional methods. This system dynamically captures both static and dynamic properties of materials using advanced motion compensation techniques. By integrating multiple radiographic modalities into a coordinated robotic platform, it provides rapid, high-resolution imaging of composite materials of large structures without the need for disassembly.

The system was validated through simulations of a four-robot radiograph setup, treated as two single-plane systems. The 3D position and orientation of a cube phantom were determined by generating computer-based digitally reconstructed radiographs from a computed tomography model and applying a 3D line intersection method based on known imaging geometries. Comparisons between marker-based and markerless kinematics tracking methods yielded differences of only 0.03 mm in translation and 0.06° in rotation.

These findings demonstrate that the proposed system significantly reduces scan times and enhances accuracy, offering a robust, scalable solution for dynamic inspection in diverse fields such as aerospace and medical device manufacturing.

Keywords: robotics-driven imaging; motion correction; multimodal; porosity analysis; materials testing, computer-based metrology; non-destructive testing.

Author α σ: New Bedford Research & Robotics, Downtown New Bedford, MA 02740, USA.

ρ: Wayne State University, School of Medicine, 1241 Scott Hall, 540 E. Canfield, Detroit, USA.

ω ζ: School of Mechanical Engineering, Faculty of Engineering, Aristotle University of Thessaloniki, 54124 Thessaloniki, Greece.

ω ζ: Centre for Research & Development of Advanced Materials (CERDAM), Centre for Interdisciplinary Research and Innovation, Balkan Centre, Building B', 10th km Thessaloniki-Thermi road, 57001, Thessaloniki, Greece.

§: Biomedical AI, New York City College of Technology, Graduate Center, CUNY, 285 Jay Street, Brooklyn, NY 11201, USA.

χ: Department of Medical Imaging, University Hospital of Crete, 715 00 Heraklion, Greece and Department of Radiology, School of Medicine, University of Crete, 710 03 Heraklion, Greece.

ν: Future Digital Manufacturing Lead with CSIRO Manufacturing, Lindfield NSW, Australia.

ϴ: Mountain Pacific Contracting and Consulting LLC, Government UE ID: PSFFFB79NLD9, CAGE Code: 9NRD9, Salt Lake City Metropolitan Area, USA;

Abbreviation	Definition
a-Si	Amorphous Silicon
CAD	Computer-Aided Design
CMOS	Complementary Metal-Oxide Semiconductor
CT	Computed Tomography
DLT	Direct Linear Transformation
DT	Destructive Testing
DR	Digital Radiography
DRR	Digitally Reconstructed Radiograph
ECT	Eddy Current Testing
EDR	Extreme Dynamic Range
EoAT	End-of-Arm Tool
FoV	Field of View
GD&T	Geometric Dimensioning and Tolerancing
HMI	Human Machine Interface
IGZO	Indium Gallium Zinc Oxide
kVp	Kilovolt Peak
MBT	Marker-Based Tracking
MeV	Mega Electron Volts
mA	Milliampere
MRI	Magnetic Resonance Imaging
NDT	Non-Destructive Testing
OID	Object-to-Imager Distance
PAN	Panoramic
SNR	Signal-to-Noise Ratio
SOD	Source-to-Object Distance
TIC	Testing, Inspection, and Certification
DOF	Degrees of Freedom
PVC	Polyvinyl Chloride
FPS	Frames per second

I. INTRODUCTION

Testing, inspection, and certification (TIC) techniques play a crucial role in developing effective material modification treatments, [1], [2], [3], [4], [5], [6], [7], [8], [9], [10]. These methods cover a wide range of evaluations, such as fatigue, impact, composition, shear, thermomechanical, or liquid flow testing, that are essential for ensuring the performance and safety of modern composite materials. Modern structures, such as aerospace components, rehabilitation devices, and vehicle parts, often consist of heterogeneous, anisotropic composites (e.g., metals, carbon fiber, resins, and thermoplastics), which present unique challenges in terms of detection and evaluation to maintain structural integrity.

A variety of destructive and non-destructive testing (DT/NDT) methods have been developed for these materials. Techniques include visual testing [8], thermographic testing, and several ultrasonic methods (Pulse Echo, Phased Array, and Thru-transmission) [2], [9], [10], [11], all designed to locate defects in single and multi-layer materials. Shearography [12] detects flaws in solid laminates and bonded surfaces through interferometric imaging under stressed and unstressed conditions. Other techniques, such as magnetic particle, liquid penetrant, optical, and eddy current testing (ECT) [13], are used to identify defects on and beneath surfaces in

conductive materials. Radiographic testing, encompassing both 2D X-ray inspection and 3D computed tomography (CT) [2], [3], [4], [11], [12], [13], [14], [15] further enhances the ability to detect internal density variations indicative of flaws. Moreover, advanced synchrotron techniques using free electron lasers have begun to overcome some X-ray penetration limitations, producing intense and tunable beams for superior resolution [4], [7], [16], [17], [18], [19].

Despite these advances, all these methods share several limitations and unresolved challenges. Processing and analyzing data remain time-consuming and requires considerable expertise, particularly when overlapping signal amplitudes make it difficult to associate them with specific damage mechanisms. Many tools employ small gantries, limiting their field of view (FoV) and hindering their application on large, non-axisymmetric structures. Surface and shallow scanning techniques often face occlusion issues, rendering deep scanning in multilayered and complex geometries unreliable. Signal noise and diffractive scattering from grain and pore boundaries further complicate image analysis. Techniques like wet magnetic particle testing rely heavily on subjective visual feedback, while assumptions in ultrasonic testing regarding constant reflection coefficients can lead to inaccuracies [2], [9], [10], [11], [12]. Additional imaging challenges include issues with figure-to-ground relationships, background luminance, line dimensions, viewing distance, orientation, frequency-dependent attenuation, spatial resolution, contrast, density, radiographic mottle, distortion, metal artifacts, and non-linear signal responses—all of which can affect the detection of subsurface discontinuities, recrystallization states, and grain sizes [9], [10], [11], [12], [13], [14], [15], [16], [17], [18], [19].

Traditional industrial CT scanners are also limited by their relatively small or inflexible gantries, their inability to dynamically adjust the focal spot, and their lack of automatic control over image magnification related to amplitude and exposure. These scanners typically require the target to be motionless, and even state-of-the-art micro- and nanotomography systems, which are confined to very small gantries, can only be used on extensively prepared, *in-situ* small samples, thereby limiting their application for on-site inspections.

A major common challenge is the motion artifact (blurriness) that occurs when inspecting moving objects. Direct measurement of internal kinematics, strain, and shear under high-speed motion has proven elusive. Although some studies have employed texture-mapped 2D models or manually segmented geometric models with template matching [14], [19], [20], [21], [22], [23], [24], [25], these approaches lack the accuracy required for comprehensive kinematics analysis, particularly in the presence of soft tissue or composite structures with variable material distribution. While 3D techniques like CT and magnetic resonance imaging (MRI) allow for direct observation of underlying structures, they do not yet achieve the high frame rates necessary for dynamic function estimation, and their confined imaging environments hinder full-motion kinematics measurement.

Furthermore, none of these techniques has been standardized to date in terms of homologating dynamic inspection methods into a unified framework. There is a need to integrate these methods under a common reference system, both in terms of coordinate systems for data expression and normalization of kinematics data obtained from both marker-based and markerless tracking. All the above conventional testing techniques can last from several hours, to days or even months, as in the case of Maintenance, Repair, and Overhaul (MRO) A, B, C, D airplane checks [23], [26], depending on the size and complexity of the target and the laborious task of disassembling its parts to scan in the laboratory.

The proposed robotics-driven multimodal imaging system with real-time motion compensation uniquely addresses these longstanding limitations. Unlike traditional systems, this platform is designed to inspect moving objects by dynamically compensating for motion artifacts, ensuring high-resolution imaging even during operation. Moreover, by unifying multiple imaging modalities under a

common reference system, our system bridges the gap between disparate inspection methods, eliminating data inconsistencies and errors. This comprehensive approach not only enhances the detection of defects and internal anomalies in composite materials but also paves the way for more accurate and efficient on-site inspections across a variety of engineering fields.

II. METHODS

2.1 System Overview and Data Acquisition

The research leading to current state of the art of the device presented here can be summarized in the following references: [6], [14], [27], [28], [29], [30], [31], [32], [33], [34]. The Logimagine Helios System (KINEMAGINE/ATLAS Inc., [35]) used here employs several six to twelve-axis coordinated robotic systems. Configurations range from two to six robots (or cobots), programmed to carry combinations of X-ray housing units, dynamic flat panels, multicamera vision systems, intensifiers with high-speed radiography cameras, and densitometry detectors (fig. 1). The figure 1 presents the "One device-multiple modalities" principle and data fusion in the robotic scanner where the large robotic arm tool (far left) connects the end-of-arm tool (EoAT) with several multifunctionality connectors with a "female" component. Many male components of the device are attached to different detectors and emitters. These include intensifiers with high-speed X-Ray cameras, flat panels of different properties, large DEXA panels, perovskites panels, scintillation panels, different emitter and collimator combinations etc. This in turn, enables scanning an object in the same field of view with different emitter-detector combinations i.e., scan it with multiple modalities. These modalities (1-8) are digital radiography (DR), Panoramic and 360 DR, high-definition Micro CT, CT, 2D and 3D high speed stereovideoradiography with two (or more) planes, 2D and 3D tomosynthesis (Tomosynthesis, is a modality similar to, but distinct from CT which uses a more limited angle in image acquisition. Rather than a 360-degree acquisition of a structure, tomosynthesis, via an x-ray tube 'arcing' method over a stationary detector, can capture an arc sweep of a single part of the structure [28], [30], [32], [36]. This technique reduces the burden of overlapping structures/composites when assessing for single entities such as composite materials and layered objects. One of the primary advantages of tomosynthesis is its very high-resolution capabilities (as it functions as a magnification method); Tomosynthesis, if combined with optical magnification it can reach 10 μm resolution. The far-right column of images in figure 1 shows different types of imaging of various size objects (machine parts, jet turbines fuselage support structure etc.) that resulted from the aforementioned modalities.
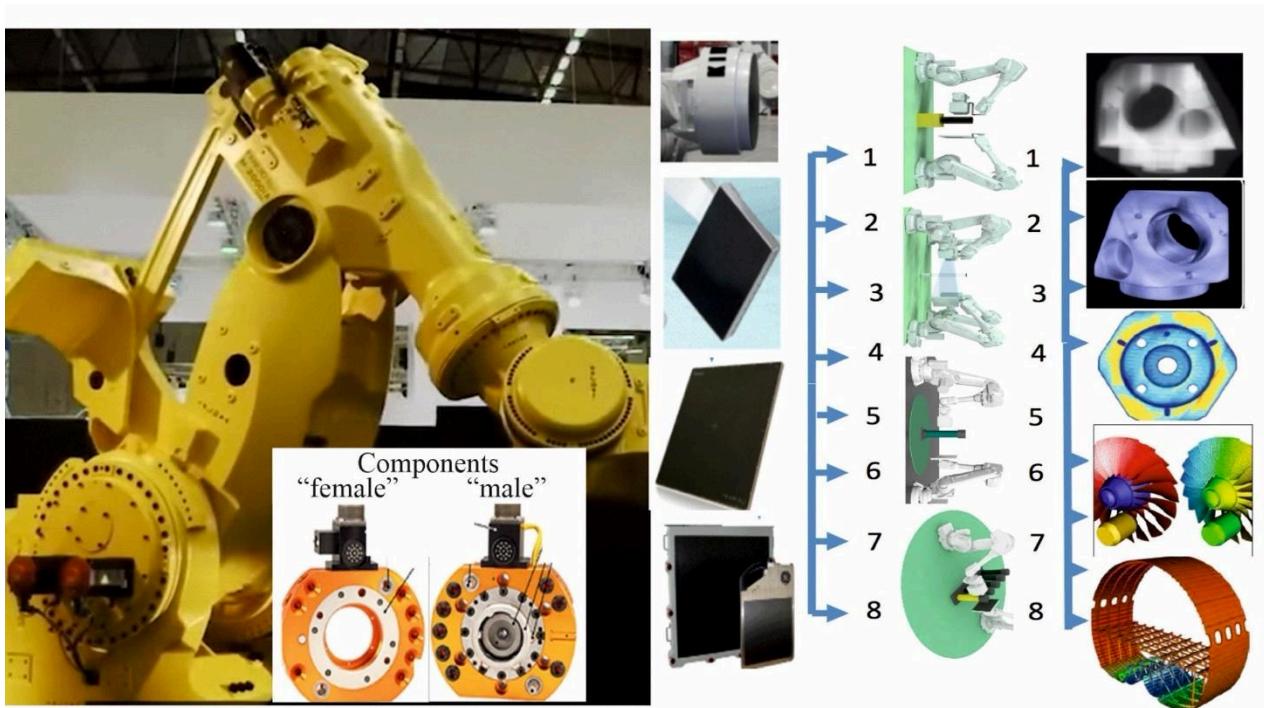
Figure 1: Robotic scanner architecture illustrating the "One Device–Multiple Modalities" principle, where coordinated robotic arms integrate various emitter–detector combinations (e.g., DR, CT, tomosynthesis, stereovideoradiography) to capture multimodal images in a single field of view.

Several robots of different additional robotic arm types can be utilized interchangeably in the device. The system is manipulated via a computer and a human machine interface (HMI) device that stores a plethora of TIC imaging protocols. End-of-arm toolkits at the robots can exchange different emitters and detectors therefore employing different imaging modalities in the same calibration space. A collection of rails, pedestals and mobile trailers can extend the system's functional scanning envelop to reach targets up to 160 feet tall and of "unlimited" width and breadth (fig. 1, 2).
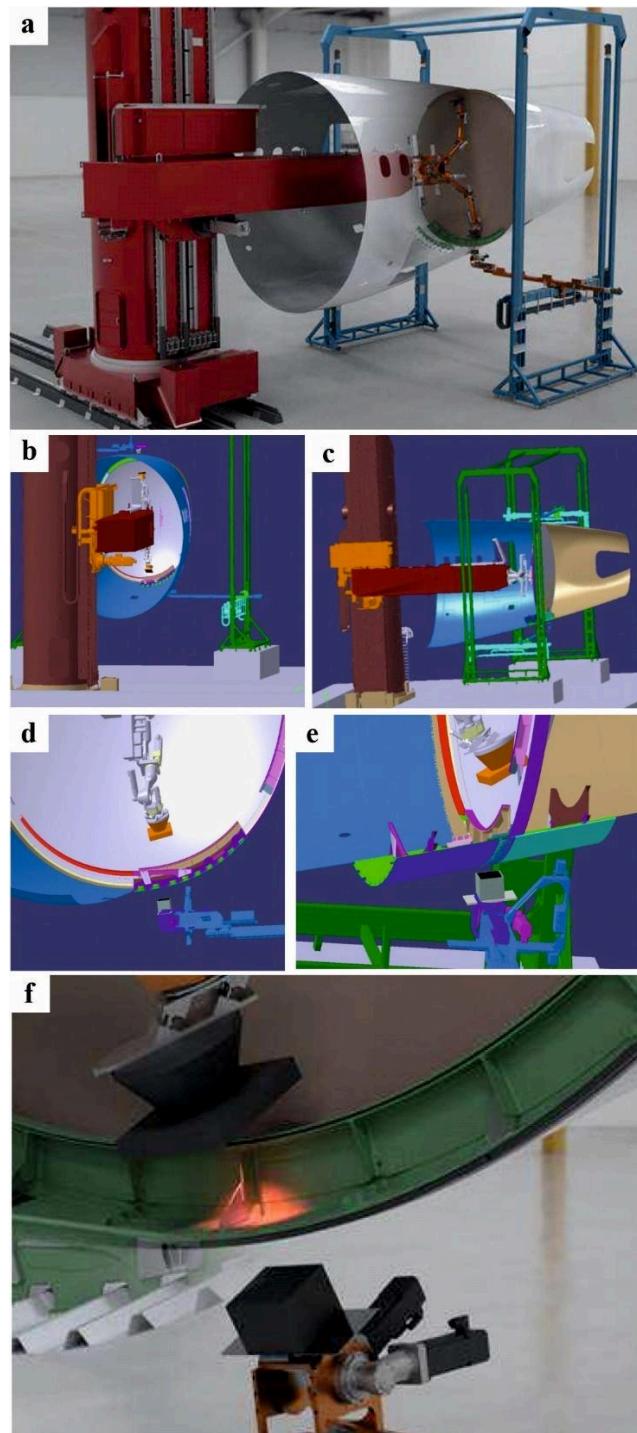
Figure 2: (a) Large size robotic scanner mobilized by a huge base on a rail system with multiple degrees of freedom to approach the inside of a plane fuselage (with 160 feet high and up to 120 foot reach capacity so it can approach the full length of large long and non-axisymmetric objects (plane wings, jet engines, fuselages, large vehicle components, pipes etc.); (b)-(e) show the leading scanning robots carrying emitters and detectors as they approach the part in the fuselage to actually scan i.e., a deep layered joint of the connection of the cockpit to the fuselage as shown in (f).

The "one-system-many-(potential) modalities" options ensure error free fusion of all the imaging modalities and co-registration of all the data in one unique robotic coordinate system (fig. 3), [27], [31], [32], [33], [34], [37], [38]. The last large-scale imaging modality for huge structures

is very important as the scanning logistics with large objects that normally do not fit in the gantries of traditional scanners can be extremely laborious and most of the times impossible. These modalities can be tuned to provide industrial CT and microCT damage inspection, porosity analysis, dimensionality analysis, failure analysis, reverse engineering, 2D radiography with panoramic large format and automatically stitched imaging for huge and non-axisymmetric objects, densitometry of composites and stereofluoroscopy in 3D. The last option is extensively tested here as it relates to dynamic imaging for characterizing the deformation of materials under linear and shear strain.
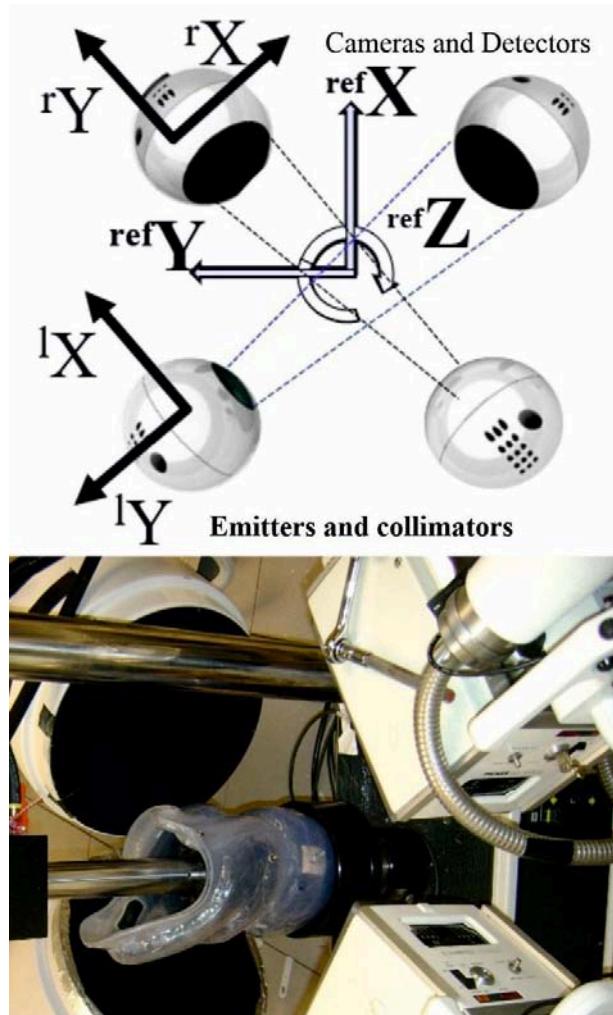
Figure 3: Top: The global reference coordinate system ^{ref}XYZ for the biplane system and two local coordinate systems (right single plane ^rXYZ and left single plane ^lXYZ) for normalizing the kinematics information; Bottom: close-up view of the actual leading "scanning head" of robotic system with two emitters and two intensifiers positioned by the robots to scan a composite structure;

2.2 Imaging Protocols-Variable Source to Object Distances (SOD) and Object to Imager Distances (OID)

The system adapts to meet the requirements of the scanning object, eliminating the need for extensive sample preparation. Programmable adaptable collimators control the exposure and manipulate the field of view (FoV) leading to an overall controlled and optimized emission, suitable for each application based on specially performed calibrations (fig. 4). Figure 4a illustrates the overall setup of the robotic radiographic system, including the X-ray emitter, detector, and a third robot dedicated to positioning calibration grids and phantoms.

Advanced Robotic Multimodal Imaging with Real-Time Motion Compensation for Dynamic Structural Health Monitoring

Figure 4b shows the multi-marker 3D calibration cubic phantom that contains a 1145-marker 3D micromachined grid made of polyvinyl chloride (PVC) with accurately (and orthonormally) embedded tantalum markers having diameters raging from 0.02 to 2 mm. This cubic phantom is used to determine the imaging geometry of the robotic radiographic system. This cube is also used to correct distortion introduced by the image intensifiers and associated optics [33], [34]. Figure 4c shows the head of one of the rods carrying two calibration markers; the micro-CT image in the background demonstrates the scanner's 10 μm resolution capabilities. In Figure 4d, each tantalum marker's position is calculated to determine the system's setup for 3D volumetric reconstructions, while Figure 4e provides a close-up view of a single-plane projection highlighting a tantalum marker's X-ray signature. The system employs geometric and optical magnification techniques with fixed, clearly defined coordinate systems to enhance imaging resolution (fig. 3).
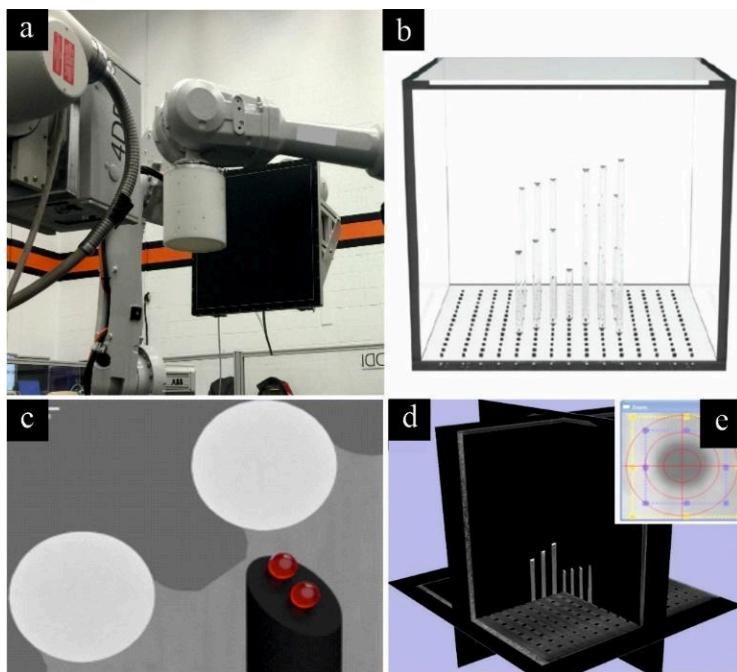
Figure 4: Overall controlled and optimized emission/detection approach using multiple robots and specialized phantoms: (a,b) System overview with programmable collimators; (c) Head of a rod carrying two calibration markers-beads, shown with a micro-CT background (10 μm resolution); (d) 3D reconstruction of the calibration cube with embedded tantalum markers; (e) Single-plane projection revealing the X-ray signature of a tantalum marker.

2.3 Emitters and Detectors

A selection of different emitters is available, ranging from low power systems to powerful X-ray generation grids for deep layer imaging. For reference we cite here the X-Ray generators that were mostly used in the present work but many more are part of the device options [35]: Max. Voltage 1-160kV with Max Power 300-1.2kW, Max mA 600. Note that a wide variety of focal spots are implemented (ranging for 0.063 to 7.5 mm and micro level applications with the microfocus focal spot sizes reaching 16 μm). In the high-energy X-ray CT production option up to 9 MeV, a fine energy bin width of less than 100keV is required with an optimized signal-to-noise ratio (SNR) when inspecting with appropriately tuned focal spot, large and dense parts in deep structures such as those associated with aerospace or automotive inspection work. Detectors include amorphous silicon (a-Si), indium gallium zinc oxide (IGZO), and CMOS sensor type panels, among others. Binning and automatic stitching of

images enhance appropriately the resolution and field of view (**fig. 3**). For reference we cite here detectors that were mostly used in the present work but many more were employed [38]: a) 16x16 to 43x43 cm, Pixel matrix 1536x1536 to 4288x4288, pixel size 45 to 200 μm resolution, Max frame rate 40 to 160 fps, 2x2 binning 280fps, PAN option 600 fps, active area; b) DC-TDI Photon counting, 102/78 mm- 1030/412 mm x 6, Pixel size 100 μm, Max frame rate 333-6000 fps, both single and dual Energy; [35]); c) Halide perovskites [39] were also employed due to their strong X-ray absorption and excellent optoelectronic properties (high spatial resolution of 12 lp mm^{-1} and excellent X-ray imaging properties under a remarkably low X-ray dose of ~50 μGyair, which is just half of the X-ray dose typically used in the traditional flat panel equipment. Coupled with the image intensifiers configuration are specially customized (CMOS) back side illuminated (BSI) camera sensors with 9.27 μm pixel size, 2560 x 1664 resolution and capacity for 9,350 fps data acquisition rate. A global electronic shutter with an extreme dynamic range (EDR) make these unique for dynamic imaging.

2.4 Motion Compensation Techniques

Resolving image artifacts (blurriness), motion detection and compensation has been always a huge challenge for both 2D and 3D imaging protocols, from the early days to the most recent stereovideoradiography research [40], [41], [42], [43], [44], [45], [46]. External fiducial markers attached on the surface of the object to be scanned were used in many stereovideoradiography approaches [30], [37], [47] to correct these motion artifacts. The present system employs motion compensation techniques to acquire high-quality images while the object is in motion, i.e., while the object is performing a high-speed load bearing task and is undergoing deformation. This is achieved here, through the accurate (robot's accuracy is 10 μm) positional-geometrical X-ray source-detector trajectory recording during the scan procedure [28], [29], [30], [34], [36], [37]. The relationships between all X-ray components, therefore, are also known with high precision (0.005mm is the robot's precision), allowing for an almost error-free fusion of all imaging modalities. Note that the accuracy and repeatability of the robots reported here is relevant to high speeds of operation at the manufacturing environment. Contrary to these speeds the operational envelop of speed for the robots used here never exceeds 10% of their maximum capacity. This was expected to improve their stabilization and repeatability parameters.

The open gantry mechanical architecture of the system allows 360° visibility so that the high-speed vision system produces highly accurate relationships between the moving object and the detector/emitter combinations i.e., the robotic arms. Practically, what this means is that unlimited trajectories in space between the emitter and the detector are feasible for the first time in tomography. Once the motion is known, the motion compensation is applied at the back-projection step. To minimize motion blur during rapid target movement, the system is also capable of synchronously acquiring 10000 fps from two cameras fixed at the two different robotic arms during movement of the object scanned. This configuration provides a large, open area suitable for either rail-assisted scanning of large sized objects by following them for part of their trajectory or scanning of free moving objects that cross the field of view.

The marker-based and markerless motion tracking techniques have been documented elsewhere, [23], [28], [29], [30], [31], [32], [33], [34], [36], [37], [47], [48], [49], [50], [51], but detailed TIC-related calibration and accuracy analyses for both techniques are given here. Experience with this system during these past different-size composite parts studies has shown that adequate data can usually be obtained with a minimum of 1 min X-ray duration, generating estimated entrance exposure of approximately 880 mR/test (times two for the stereotactic biplane mode of the device) for a typical aircraft engine part (turbine blade) study. Such study usually consists of three trials each of two different movement activities resulting in a total entrance exposure of approximately 4-5 R and up

to 10 times that magnitude if the blade is scanned through its entire cover, without disassembling. The system, however, can run for more than an hour to scan deep structures and allow for high-resolution, high-density data, depending on the composite structure and depth of the part in question. Although the radiation exposure can be monitored, it was not the case in the present study. A series of studies in the past have enabled for multiple assessments to minimize the total number of trials and Xray generation required for a specific target (type of material, size/dimensions of parts, composite structure, and distribution of material). This comprehensive imaging approach allows for accurate calibration and assessment of different target sizes and materials, while the system's flexibility supports varying scan durations and exposures based on the complexity of each component. The device's KINEDOSE manual, provides the user with numerous protocols (see sample image in fig. 8b) specifying parameters (FoV, dose, exposure etc.) multi-trial testing for several materials [35].
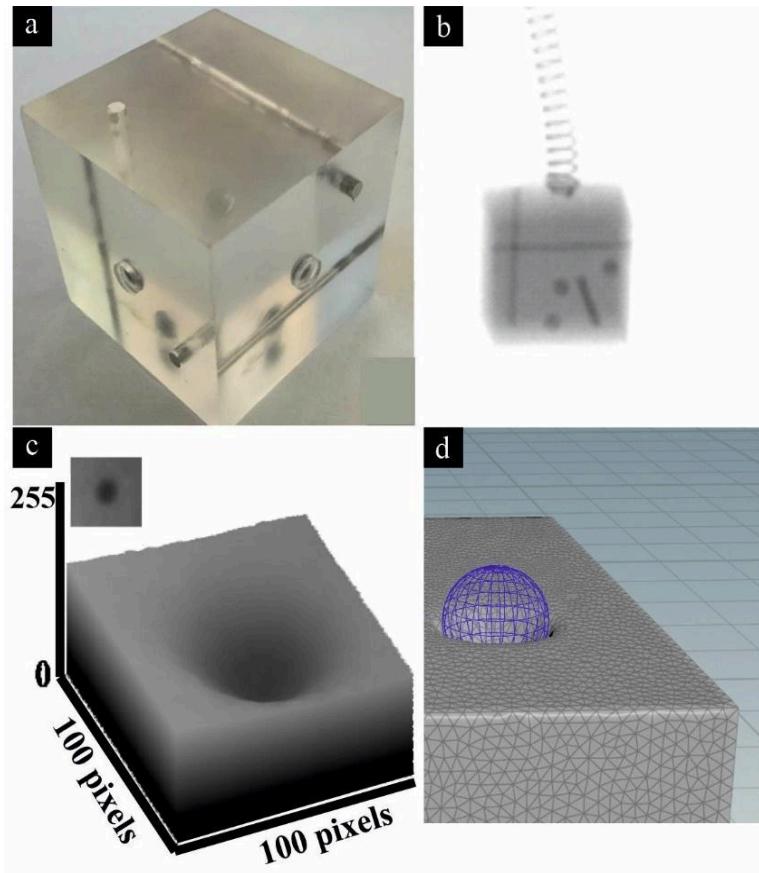
Figure 5: (a) Phantom cube showing embedded markers and rods; (b) Radiographic view of the cube; (c) Tantalum marker 3D surface plot illustrating intensity distribution; (d) 3D model overlay emphasizing internal geometry.

In addition, biplane radiographic high-resolution image sequences of a fixator from an aircraft wing component and from a phantom calibration cube of known geometry (fig. 5) were collected using the 3D CT modality to be used for calibration, development and testing. The calibration object (fig. 5a) is a Plexiglas cube with 30mm side and 0.6mm diameter tantalum spheres placed flush in the middle of the top surface of the three orthonormal cubic sides. In addition, tantalum cylindrical rods (0.3mm in diameter) placed flush and parallel to the surface of the three orthonormal sides at 8x8mm from the corners were used for geometric reference; Figure 5b illustrates a biplane radiographic image sequence of this phantom cube of known geometry,

acquired via the 3D CT modality for calibration and testing of marker-based and markerless tracking. Fig. 5b highlights how the cube's internal features appear under X-ray during high-speed movement while the cube is suspended from a spring; Fig. 5c provides a 3D surface plot derived from the scan, from a detector with 2304x2304 pixels resolution, demonstrating the gray level intensity distribution of a selected region with a tantalum marker. Fig. 5d shows a 3D surface model overlay, here visualized with a spherical mesh, to further emphasize the shape and positioning of key internal elements. The ANSA BETA CAE systems software [52] reconstruction of the volumetric cube using tetrahedra can clearly depict the tantalum market structure and can perform different type of volume and geometry measurements. These one-to-one voxel-to-element correlations are used by the meta-analysis to differentiate between composite layers. The distances between the tetrahedra centroids are also used to quantify geometrically the 3D micro level damages in the structure of the object in question (dimensionality) [33], [51].

The front part of the component and the cube had at least four radiopaque markers (1.6-mm tantalum markers-beads) glued to different areas (internal and external). This allows determination of six DOF motion parameters with high accuracy (errors of 0.01 mm for translation and 0.12 for rotation) using the previously developed marker-based method [27] A comparison was performed between the marker-based method and the 3D model-based markerless method for evaluation of accuracy on predefined known motion of the cube test. Initially, a CT scan of the target fixator within the aircraft wing structure and the phantom cube were obtained to generate their volumetric model. One thousand and four hounded 0.001-mm-thick transverse-plane slices (2560x1664 pixels resolution, capacity for 9,350 fps, and in different binning resolution could reach 4096x2304 at 1000fps) were acquired from the surface of the part and up to 55 cm below the wing part surface.

Segmentation of the CT-scanned target was performed by thresholding the slices to isolate the aircraft fixator from remaining structures. Radiopaque tantalum marker signatures were identified automatically by the software and an operator confirmed their selection (fig. 5, 7, 9). The software replaced voxel values with the mean values from surrounding voxels to eliminate influences of the markers (masking). The volumetric model was resampled using a bilinear interpolation function to the same resolution as radiographic images acquired with the biplane robotics system. The same process was repeated for the phantom cube.

The markerless motion tracking technique, i.e., the 3D model-based method assumes that a properly oriented projection through a 3D volumetric model will produce an image similar to the radiographic images. First, imaging geometry of the biplane radiograph system was determined based on a reference coordinate system (fig. 3) [43], [53]. The biplane system was simulated as two single-plane radiograph systems based on these parameters.

An overview of the tracking process for the single-plane radiograph system is provided in fig. 6. The algorithm consists of four major components: volume visualization (model projection), image preprocessing, similarity measurement, and optimization. In the volume visualization step, a 3D texture-mapping technique is used to project through the 3D target part volumetric model and generate a digitally reconstructed radiograph (DRR) (adopted from [44], [45]). During the preprocessing step, a set of image processing algorithms (edge extraction, image enhancement) is applied to extract the coarse edge of the target if necessary (fig. 7).

In other words, the 3D CT volumetric model collected with the CT modality of the robotic scanner is translated and rotated by 6 motion parameters (3 translations and 3 rotations) using an initial guess and projected to 2D image by the volume visualization method. The produced projected DDR requires some pre-processing (fig. 7) to be roughly segmented the component to be tracked from other parts.

Fig. 7a presents (a single X-ray image (out of thousands) from the dynamic stereovideo-radiography sequence showing internal structure undergoing strain; Fig 7b shows a Gaussian filter to identify the major object markers or landmarks to be assessed whereas fig. 7c is identifying the relative object localized strain by assessing the elongation/deformation (Δl) of the various object markers or object landmarks forming a mesh at different time instants; Figures 7d–7e illustrate a similar estimation of relative engineering shear strain by assessing the 3D skewness (departure from orthonormality in (e) or initial geometry in (d) of the object mesh; Fig. 7f illustrates how image processing of the grey signature of a cross-like structure at the object mesh in terms of grey level distribution, assists in identifying shear by comparing the mesh at rest (unloaded object, top) and the skewed mesh (loaded object, bottom) [33]; Fig. 7g indicates how the CT model projection is performed. The CT model is resampled with equally spaced planes along the viewing direction and a DRR is generated by summing pixel values along projected rays from the X-ray source to the image plane.

Similarity between the DRR and the radiographic image is determined with a correlation. An optimization algorithm iterates motion parameters until the maximum similarity is obtained. Once six DOF of the center point of the target model are estimated from each single-plane system, the absolute 3D position and orientation of the target part in the reference coordinate system are determined using a 3D line intersection method (fig. 10) and the known imaging geometry of the robotic system. Note that the correlation process between two images continues until this iterative optimization finds the optimal similarity.
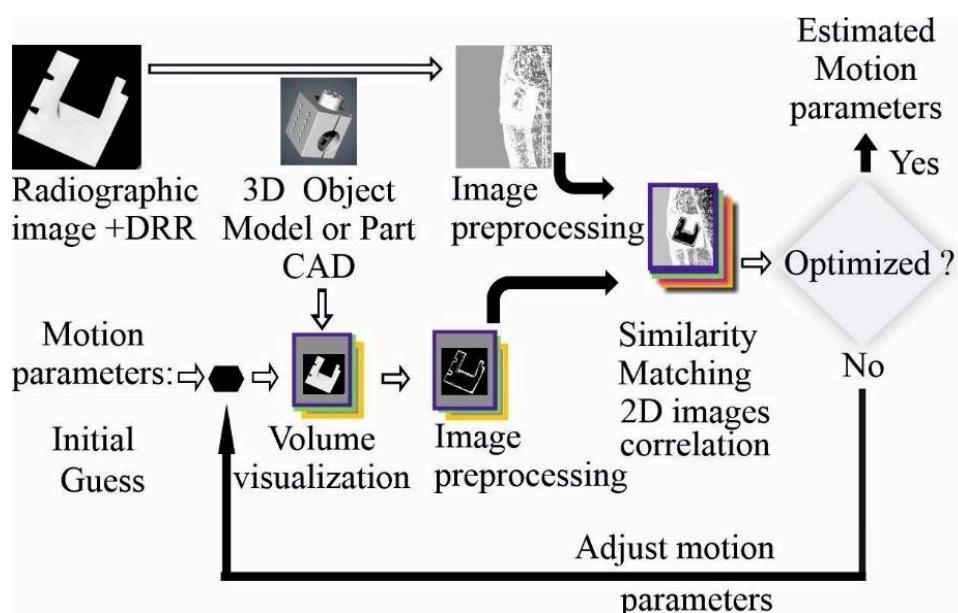

Figure 6: Overview of the process for measuring the object position and orientation from the single-plane radiograph system.
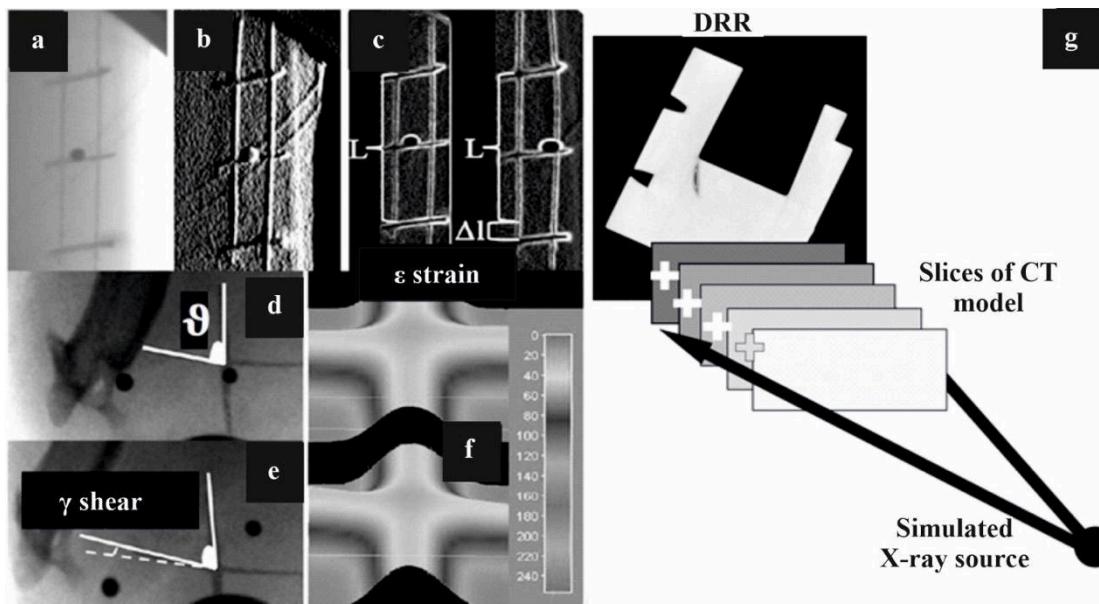
Figure 7: (a) A single X-ray image (one of thousands) from the dynamic stereovideoradiography sequence, showing the internal structure of a target under strain or shear; (b to f) show different image processing techniques to detect major markers or landmarks on the target so the resulting relative localized strain and shear can be calculated; (g) CT model projection, where the CT data is resampled into equally spaced planes along the viewing direction, generating a digitally reconstructed radiograph (DRR) by summing pixel values along projected rays from the X-ray source to the image plane.

2.5 Determination of Imaging Geometry

Imaging geometry was determined using the multi-marker 3D calibration cube presented earlier (fig. 5). The calibration cube was put in the view area of the biplane system, and biplane radiographs were acquired. Positions of each marker were calculated to determine the configuration of the robotic system relative to the global reference coordinate system using the direct linear transformation (DLT) method [43]. Each single-plane system, right and left (denoted by "r" and "l," respectively), of the robotic system was described with its extrinsic and intrinsic parameters. Extrinsic parameters consist of the position and rotation of the X-ray source of the single-plane system in the global reference coordinate system. For the right_(left) system, a position vector, $^{ref}P_{rs}$ ($^{ref}P_{ls}$), a rotation matrix, $^{ref}R^r$($^{ref}R^l$), were determined from the DLT method. Intrinsic parameters include the principal point and the principal distance of the single-plane system *(fig. 8a).*
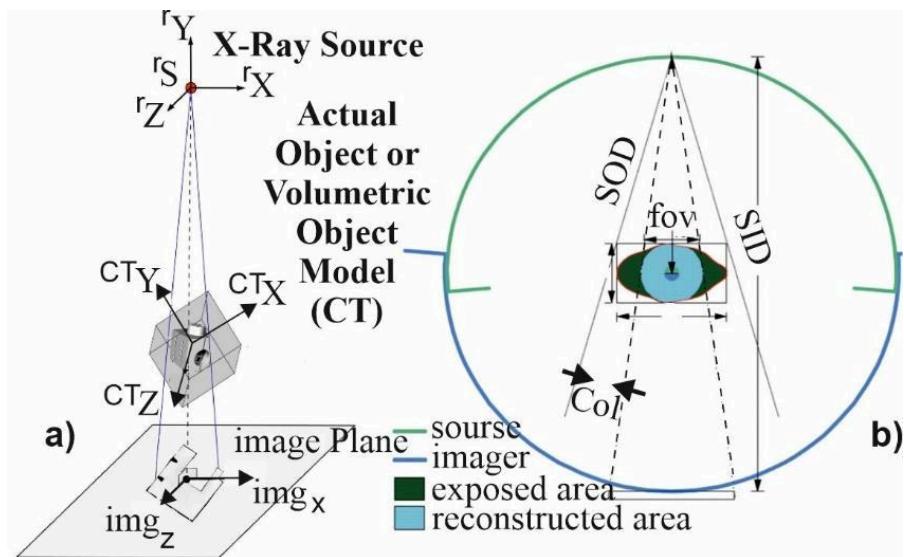
Figure 8: (a) Imaging geometry of the single-plane radiograph system (one of the two subsystems in the stereotactic configuration (b) Geometric magnification by adjusting the SOD and OID.

Principal distance (rPD), is from the X-ray source (rS) to the principal point (rPP) in the image plane and the principal point is the origin of the image plane. X axis and Z axis of the image plane are parallel to those of the X-ray source; Notice the projection of the 3D object at the image plane is expressed in an appropriate coordinate system. Geometric magnification is achieved by adjusting the SOD and OID (fig. 8b), while optical magnification uses specialty lenses to achieve different levels of magnification before the signal is recorded at the detector side imaging Protocol example 1: SOD = OID, concentric circular trajectories of source and detector about the object (for Cone and Fan-beam configurations). In blue and green solid line, the detector's and source's pathway are depicted respectively. The magnification factor is double and the FOV restricted; when SOD>OID, the concentric circular trajectories have different radii resulting in significant controlled magnification reduction (1<M<2) and increased FOV with larger volume captured and reconstructed; Collimators (Col) are used to limit beam size to the specific area of the object.

The principal point, $^{r}PP(^{l}PP)$, is the location in the image plane of the right_(left) system, perpendicular to the center of the X-ray beam. The principal distance, $^{r}PD(^{x}PD)$ is the distance from the X-ray source to the principal point of the right_(left) system. The intrinsic parameters, along with the size and resolution of the radiographic image, were sufficient to accurately simulate two single-plane radiograph systems. The extrinsic parameters were used to reconstruct the biplane system for determining the absolute 3D pose of the target in the global reference coordinate system of the robots.

2.6 Volume Visualization

With the geometry of the imaging system known, DRRs can be generated from the 3D target model using volume visualization methods [22], [23], [35], [43], [45], [46], [48], [54], [55], [56]. Perspective (rather than parallel, fig. 7g) projection rendering is required to accurately represent the cone-beam X-ray image formation process. Additive reprojection [54] or ray-casting methods [44], [48] are commonly used for this purpose. However, these methods are computationally intensive, particularly for iterative methods. Restriction of the CT target model to specific regions [22], [24] and/or precomputing a library of ray integral values have been proposed to accelerate the rendering process [23]. However, for tracking arbitrary orientations of large composite parts moving through significant volumes, the computational cost of precomputing the required number of rays approaches that of ray-casting. To significantly

reduce rendering time, perspective projections were generated using a hardware-accelerated 3D texture-mapped volume rendering method, implemented using the OpenGL graphics library [35]. The entire 3D model volume data was downloaded into texture memory once. To simulate a desired 3D orientation, the volume was rotated to orient the target properly and re-sampled in memory to create equally spaced planes perpendicular to the principal axis of the X-ray beam. Each pixel of the DRR was calculated by summing re-sliced pixels along a ray constructed from the X-ray source to the image plane *(fig. 7g)*. This reduces rendering time by a factor of about 60, at the cost of a slight reduction in the quality of the resulting DRR (relative to traditional ray-casting).

2.7 Image Preprocessing

The data acquisition rate varies from 1 to 10,000 frames per second (fps), with angular speeds of the robotic arms ranging from 1 to 20 degrees per second. The system processes 450 to 12,000 2D projections in real-time, depending on the application and mode, providing 3D reconstructions within seconds. Using the pulsing X-Ray capabilities, the accumulative exposure time can be less than a second (<1s) and up to several minutes in prolonged scans [32], [33], [38], [53]. The highest accuracy is obtained with the highest repeatability option of the robots tuned to 0.005 mm for translation of the robotic arms at less than 1 degree per second rotational speed. Relative to conventional fluoroscopic images commonly used for 2-D/3D image registration [22], [24], radiographic images obtained from high-speed video cameras are less noisy, but still the feature-extraction process can be complicated. This situation can be worsened by the inherent inhomogeneity and anisotropic nature of composite materials. Thus, it is desirable to extract a feature set using all available information on the target composite structure, rather than only external edges or intensity information. This was accomplished by using a combination of edge and intensity information (texture information projected through 3D volume of target model- see fig. 7) based on the assumption that even "imperfect" (i.e., highly or

less irregular) edge data can serve as useful features for improving matching between the DRR and actual radiographic images. Changing the robotic pathways during image acquisition alters the projection shapes which helps this matching step when dealing with composites.

Both the DRR and the radiographic images are preprocessed prior to matching, to maximize similarity. First, the DRR is inverted and contrast-enhanced using a histogram-equalization algorithm [55], [56] (see fig. 6). Then a simple edge algorithm (Sobel edge detector [55], [56] is applied to extract edges from both DRR and radiographic images. The edge information is then added back to the original images (see fig. 7), combining both edge and texture information. The edge information helps to drive the optimization toward the correct solution, improving initial algorithm convergence [57]. The addition of the intensity/texture information leads to more accurate matching than is possible with edge information alone.

2.8 Similarity Measurement for the marker-less tracking algorithm

To determine optimal position matching, a metric for similarity between two images is required. Pattern intensity [24], [58] and gradient difference methods [59] have been suggested for the DRR and fluoroscopic images. These studies assumed that image quality is high, and that composites structures have a relatively small role in the intensity distribution in fluoroscopic images. Because high-speed radiographs can be noisy and at areas contrast-limited, and there is a great deal of composite deformation during dynamic studies, detectable edges and features in the actual radiographs differ from those in the DRRs. Thus, these assumptions are no longer valid, and a different approach was required.

Evaluation of several different correlation strategies suggested that general normalized correlation [55], [56], applied to summed edge/intensity images, is robust even in the presence of these differences between actual radiographs and DRRs. The correlation equation used for this study is

$$V(x, y) = \frac{\sum\limits_{x,y}\left[r(x,y)-\overline{r_{u,v}}\right]\left[m(x-u),y-v)-\overline{m}\right]}{\left\{\sum\limits_{x,y}\left[r(x,y)-\overline{r_{u,v}}\right]^2 \sum\limits_{x,y}[m(x-u,y-v)-\overline{m})]^2\right\}^{\frac{1}{2}}} \quad (1)$$

r(x,y) radiographic image;

m(x,y) DRR generated from the 3D CT model;

m mean of the DRR;

$r_{u,v}$ mean of radiographic image in the region under the DRR.

However, this is computationally intensive, especially if the size of images to be compared is large (as is often the case with images of large composite materials). A new Quadtree-based normalized correlation method was employed to reduce search iterations and improve optimization efficiency. A predefined search space of the radiographic image is divided into four quadrants (fig. 9). Note how resolution affects the size of the acquired tantalum marker X-ray signature. Steps one to six of the process of isolating the high-resolution marker (shown in subgraphs 1-6): 1-2-3: Masking of the marker signature, 4-6: The 5x5 Laplacian filter applied on a small area around the marker's region to enhance the contrast and remove the useless information (background noise) close to the marker. Quadtree-based correlation is also shown. Correlation space is divided into four regions. The region with the best match is subdivided again. This process is repeated until the region size is reduced from thousands to 4 X 4 pixels.
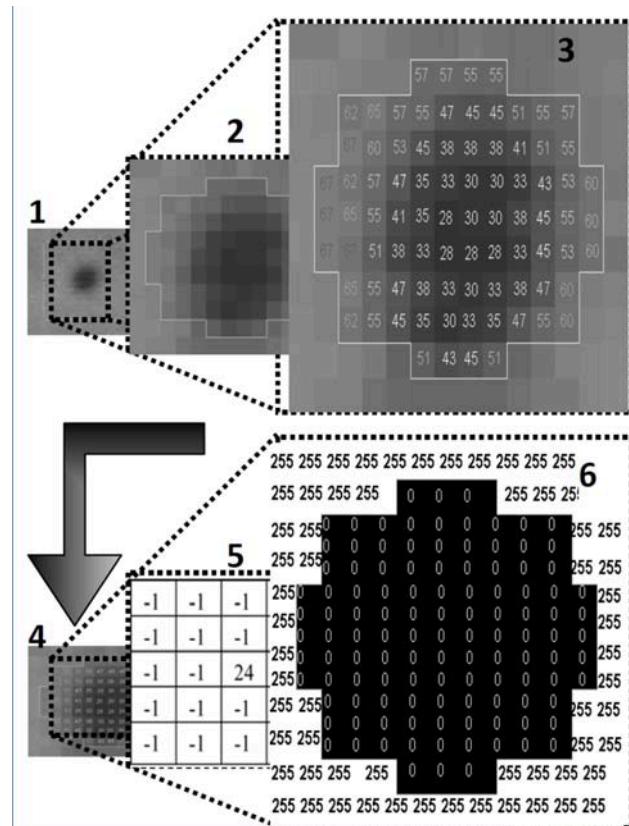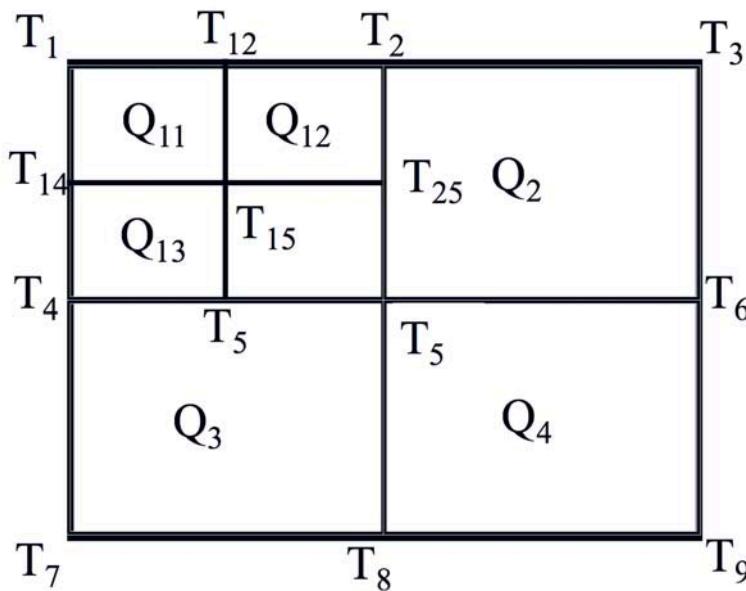
Figure 9: Top: Tantalum marker X-ray signature surface plots at 576 × 576 and 2304 × 2304 pixels, with subgraphs 1–6 showing the masking and Laplacian filtering steps. Bottom: The quadtree-based correlation, where the search space is repeatedly subdivided until a 4 × 4 pixel region remains.

The average correlation value (AT_{q1}, AT_{q2}, AT_{q3}, AT_{q4}) of each quadrant (Q1, Q2, Q3, Q4) is calculated from correlation values of four corner points of the corresponding quadrant (equation 2). The quadrant with the best correlation is further divided for the next step (equation 3). For example, if AT_{q1} is the optimal, AT_{q11}, AT_{q12}, AT_{q13}, and AT_{q14} are calculated. This procedure continues until the size of a quadrant reduces to 4x4 pixels. In the final step, all pixels of the optimal quadrant of the radiographic image are correlated with the DRR. The coordinate of the pixel with the best match is chosen as the location of the target center in the image plane ($^{ref}P_{rm}$ and $^{ref}P_{lm}$ see fig. 10).
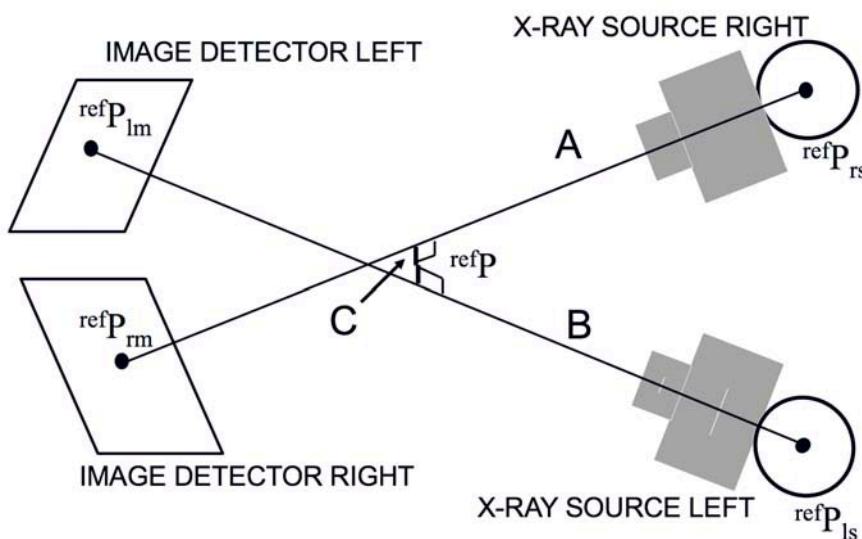
Figure 10: Determination of 3D target part position. refPrs(refPls) is the position of the X-ray source of the right_(left) system relative to the reference coordinate system. refPrm(refPlm) is the best-matching location in the right_ (left) image plane expressed in the reference coordinate system. The mid-point of the line segment "C" is chosen as the optimal 3D position.

The value of the correlation function at this point is used as an indicator of the quality of match for the optimization process described below. For a maximum expected frame-to-frame translation of 200 pixels (400x400 pixel search region), the efficiency of the Quadtree algorithm is clearly illustrated. Conventional sequential correlation would require 16000 image multiplications to find the best matching position, whereas the Quadtree-based correlation method requires only 400 multiplications. This is a significant detail when thousands of frames need to be tracked.

At the first iteration:

$$ATq1 = \frac{T1+T2+T4+T5}{4} \; for \; quadrant \; Q1$$
$$ATq2 = \frac{T2+T3+T5+T6}{4} \; for \; quadrant \; Q2$$
$$ATq3 = \frac{T4+T5+T7+T8}{4} \; for \; quadrant \; Q3$$
$$ATq4 = \frac{T5+T6+T8+T9}{4} \; for \; quadrant \; Q4 \qquad (2)$$

At the second iteration

$$ATq11 = \frac{T1+T12+T14+T15}{4} \; for \; quadrant \; Q11$$
$$ATq12 = \frac{T12+T2+T15+T25}{4} \; for \; quadrant \; Q12$$
$$ATq13 = \frac{T14+T15+T4+T45}{4} \; for \; quadrant \; Q13$$
$$ATq14 = \frac{T15+T25+T45+T5}{4} \; for \; quadrant \; Q14 \qquad (3)$$

2.9 Optimization

The downhill Simplex method [57], [60] is used to adjust estimated target part position and orientation until optimal similarity is obtained. The Simplex method requires N+1 points as starting points, where N is the number of DOFs of the function being optimized. Then the simplex method travels through the parameter space by reflection and contraction. Estimating 3D kinematics would typically require simultaneous optimization of all six motion parameters (three positions and three rotations).

The optimization routine began with six predefined vertices (as required for Simplex) as the starting points. An initial guess was determined manually for the first frame or selected as the optimal position of the previous motion frame. The remaining five vertices were selected to span the range of valid target orientations. DRRs for each vertex were generated from the 3D model using the known imaging geometry of a single-plane system and five DOF parameters controlled by the optimization process. Then two in-plane position parameters were determined from correlation between the DRRs and the radiographic images. Each reflection or contraction continued to update the three rotation parameters and the distance perpendicular to the image plane, based on the previous similarity calculations. The optimization routine was terminated when the distance of points moved in that step was fractionally smaller in magnitude than some tolerance.

To check for local minima, the Simplex routine then restarted from the optimized point and was allowed to converge again. If the new solution differed from the previous solution by more than a specified tolerance (typically, 1 for rotation), the original solution was rejected as a local (nonglobal) minimum, and the routine was restarted from the new optimum point.

2.10 Three-Dimensional Determination of Position and Orientation

Six motion parameters can be estimated from a single-plane system for each frame. However, the assessment of out-of-plane translations is unreliable with a single-plane system and the accuracy for measuring out-of-plane translations is poor relative to the accuracy for measuring in-plane translations [37], [59], [61]. Thus, only a projection ray passing from the X-ray source, through the center of the target model, to the best-matching location in the image plane was constructed from each single-plane system. This projection ray was represented as a line segment connecting the X-ray source (the origin of a single-plane system) and the best-matching location in the image plane ($^{r}P_{rm}$), for the right system and $^{l}P_{lm}$ for the left system).

For simulating the biplane system, line segments (actually, two end points) estimated from each single-plane system were transformed to the global reference coordinate system based on the information of the position and orientation of single-plane systems relative to the global reference system as follows.

- The position of the X-ray source is the origin of the single-plane system. Its location relative to the global reference coordinate system, $^{ref}P_{rs}(^{ref}P_{ls})$ for the right_(left) system, was already determined from the DLT method.
- $^{r}P_{rm}(^{l}P_{lm})$ was transformed to the reference coordinate system by a rotation and a translation (equation 4):

$$^{ref}P_{rm=}\ ^{ref}R^{r}\ ^{r}P_{rm} + ^{ref}P_{rs} \text{ (for the right system)}$$
$$^{ref}P_{lm=}\ ^{ref}R^{l}\ ^{l}P_{lm} + ^{ref}P_{ls} \text{ (for the left system)} \qquad (4)$$

where $^{ref}R^{r}$ ($^{ref}R^{l}$) is a 3x3 direction cosine matrix expressing the orientation of the right (left) system with respect to the reference coordinate system. $^{ref}P_{rm}(^{ref}P_{lm})$ is the best-matching location in the image plane of the right (left) system transformed to the reference coordinate system.

For example, two line segments within the reference coordinate system ("**A**" from $^{ref}P_{rs}$ to $^{ref}P_{rm}$ and "**B**" from $^{ref}P_{ls}$ to ($^{ref}P_{lm}$) were constructed, as shown in fig. 10.

Ideally, the two line segments "**A**" and "**B**" should intersect at a point because they pass through the same point of the target model. However, these lines generally do not intersect due to errors such as camera calibration, image noise, matching error, etc. To solve this problem, the 3D position of the target part was determined by finding the midpoint of the shortest line, "**C**", between these two-line segments using a 3D line intersection method [62], [63] (fig. 10).

Orientation of the target part (α, β, γ) could be determined from the estimated orientation $^{ct}R_b$ of the target model estimated in each single-plane system assuming body-fixed X-Y-Z rotations [64], [65], [66]

$$^{ref}R_{rb=}\ ^{ref}R^{r}\ ^{r}R^{ct}\ ^{ct}R_b \text{ for the right system or} \qquad (5)$$
$$^{ref}P_{rb=}\ ^{ref}R^{l}\ ^{l}R^{ct}\ ^{ct}R_b \text{ for the left system}$$

where

$^{ct}R_b$ constant 3x3 direction cosine matrix of the orientation of the anatomical target part relative to the CT model;

$^{r}R^{ct}(^{l}R^{ct})$ 3x3 direction cosine matrix representing the orientation of the CT model with respect to the right (left) system, determined from single-plane optimization;

$^{ref}R_{rb}(^{ref}R_{lb})$ 3x3 direction cosine matrix of the target part expressed in the reference coordinate system.

Final 3D orientation of the target part was determined by averaging the rotation angles obtained from the two single-plane views

$$= \frac{rm+lm}{2}$$
$$= \frac{rm+lm}{2} \qquad (6)$$
$$\gamma = \frac{\gamma rm+\gamma lm}{2}$$

2.11 Similarity Measurement for the landmark-based or marker-based tracking algorithm

The new MBT algorithm employs image-processing routines (Laplacian filter, Canny edge Detection [27], [44], [45], [55] and homegrown routines to the marker's geometry properties (shape and diameter) (fig. 9). A 5x5 Laplacian filter was applied on a small area around the marker's region in order to enhance the contrast (fig. 9) and remove the useless information (background) close to the marker (fig. 11).
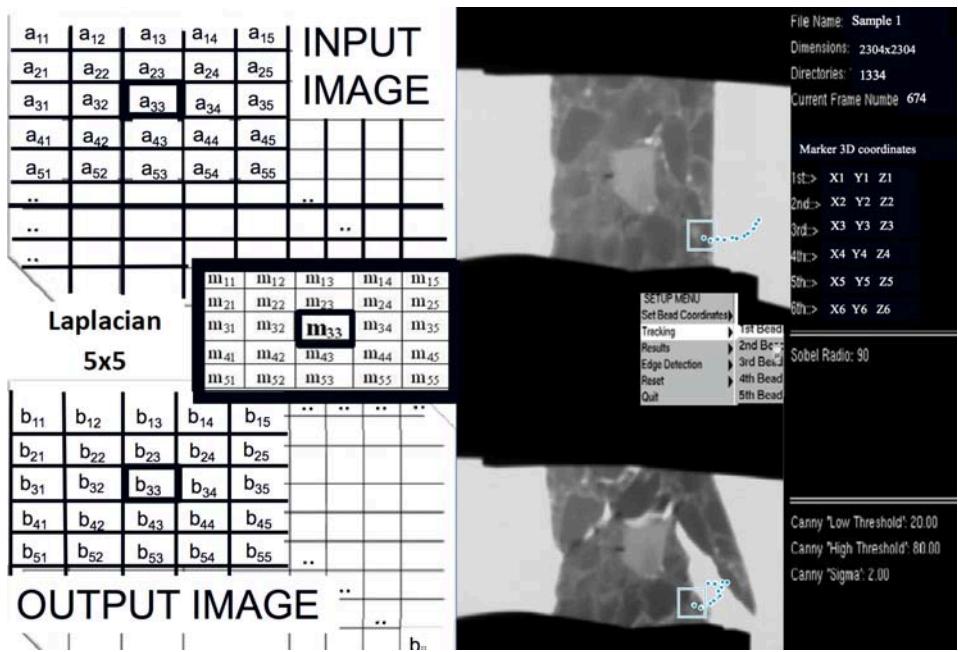
Figure 11: The 5x5 Laplacian mask (left) applied on the input image and the output image of the destructive compression granular composite asphalt test (two different views- stereo). The tracking kinematics procedure shows the results from the failed sample shown (right). The snapshot is during the marker tracking and synchronous displacement history of the selected grains from their respective images projected in real time. The plot diagram shown on the right is a collection of points from this tracking. There are approximately 1334 consecutive points during this entire catastrophic event that lie between the points shown here.

Figure 9 shows the Laplacian mask applied on an input image and how it manipulates each pixel in order to enhance the contrast. The output image is a result of summarized multiplications among the 5x5 mask values and the input image (Eq. 7).

$$\text{Output } (B_{ij}) = \Sigma(\text{input } A_{ij}) * \text{mask } (m_{ij}) \qquad (7)$$

Figure 11 shows the mask applied over the top left portion of the input image. The center of the mask is placed by the operator over the pixel that will be manipulated. For example the pixel m33 of the mask is applied on the a33 pixel of the input image and the b33 will be finally the new value of the pixel given by Equation (8).

$$b33 = a11 * m11 + \dots + a33 * m33 + agg * mgg \qquad (8)$$

This software also employs distortion correction and gray scale weighted centroid calculations to improve accuracy and provide sub-pixel resolution [27]. Three-dimensional reconstruction of the 2D biplane displacement history of the tantalum markers is performed with the help of 3D reconstruction software from Motion Analysis (Motion Analysis Corporation, Santa Rosa, CA USA). The algorithm tracks the sequences of images automatically and is an integrated part of the pre-processing toolkit of the robotic system.

Static and Dynamic performance of the biplane robotic radiographic system was assessed using the calibration plexiglas with 30mm side (**fig. 5**) presented earlier. Static precision (a function of system noise) was assessed with the cube positioned stationary in the center of the field of view. Dynamic errors were also assessed by suspending the objects from a spring and then dropping them (increased rotational motion) while allowing them to move freely throughout the field of view. A range of tests was performed using different combinations of acquisition rates, resolution, exposure i.e. 125-1900 images acquired at 400-5000 fps with exposure (shutter) times ranging from 50 to 3000 μs. X-ray system

protocols ranged from 90 to 320 kVp, 40 to 190 mA, 1-30s with low (1152x1152) and high resolution (4608x4608) tests. In the industrial objects tests 3D coordinates of markers were determined for high-speed compression tests using a materials testing machine.

III.   RESULTS

Dynamic tests were performed with a phantom target of known geometry (cube). Four tantalum spheres (0.6-mm diameter, fig. 4e) were accurately implanted in the cube to enable marker-based tracking. The texture and cube shape (with implanted parallel rods) were first used for the markerless tracking system. The cube was initially suspended by a spring and randomly moved in the field of view. Alternatively, it was held with a fixed vice attached to a computer-controlled stepper motor driven positioning system capable of two-and three axis linear movement and multi-axis rotation (0.006 35 mm/step, 0.02°/step). Three types of specific tests were performed: simple translation, simple rotation, and different combinations of translations and rotations. In the translation experiment, the cube phantom was positioned vertically (with one of its implanted rod long axis perpendicular to the ground) and controlled to move parallel to the ground (in the X-Y plane) in diagonal directions along a 100 mm square (smaller squares of 10x10 mm were sampled also). For the rotation experiment, the target was rotated ±10° internally/externally about its long Z axis (smaller rotations of ±2° were sampled also). In an example of combined translation and rotation, the target was moved diagonally in the X-Y plane with simultaneous ±10° rotation about the flexion/extension Y axis. From each experiment, a sequence of radiographic images (1000-2000) was acquired from the biplane robotic radiograph system.

For the first frame of each sequence, the six motion parameters were estimated using a window-based user interface to produce DRR that appeared similar to the actual radiographic image.

These parameters were used as an initial guess to start the optimization. The optimization routine took on average about 320 iterations for the initial guess and about 560 iterations for tracking the target from frame to frame. The average time taken by an iteration, is a few milliseconds with the biplane image sequences being tracked using the marker-based method described in methods. Our past human arthrokinematics studies have shown the accuracy of this marker tracking method to be 0.01 mm [27], [51], but we had never tested it with industrial applications. This marker-based tracking used the same calibration cube and distortion correction images as the 3D model-based method, providing a common global coordinate system for comparison. For three tests, the root mean square (rms) differences between methods in the cube experiment averaged 0.023 mm for translation and 0.06 for rotation. In detail, the room mean square errors for the cube experiment between the 3D Model-based (markerless) and the marker based method were in *translation (mm):* (XY translation: 0.013 in X-axis, 0.03 in Y-axis, 0.02 in Z-axis), (Z-axis rotation: 0.07 in X-axis, 0.13 in Y-axis, 0.06 in Z-axis), (XY translation and Y-rotation: 0.06 in X-axis, 0.05 in Y-axis, 0.12 in Z-axis); and in *Rotation (degrees):* (XY translation: 0.02 in X-axis, 0.1 in Y-axis, 0.05 in Z-axis), (Z-axis rotation: 0.05 in X-axis, 0.06 in Y-axis, 0.03 in Z-axis), (XY translation and Y-rotation: 0.02 in X-axis, 0.07 in Y-axis, 0.08 in Z-axis).

In the dynamic cube study, the calibration cube was randomly perturbed by a spring, causing marker movement through a 1500 cm³ volume (Fig. 5). During low-resolution imaging, each 0.6 mm marker covered at least 64 × 64 pixels, corresponding to a pixel size of approximately 0.086 mm/pixel. In the high-resolution setup, each marker spanned at least 200 × 200 pixels, reducing the pixel size to about 0.021 mm/pixel. For both static and dynamic tests, the 3D vector distances between pairs of markers were calculated in each frame. In the static high-resolution experiment, the mean measured distance was 29,992 μm, while under dynamic conditions, it was 29,988 μm (the true distance is

30,000 μm). Typical standard deviations (SD) from the mean distance were ±0.02 mm (static) and ±0.04 mm (dynamic). These results remained consistent across the field of view, although both low- and high-frequency noise components were observed in the raw error plots. Fig. 12 illustrates how unfiltered (total) errors, low-pass filtered errors (20 Hz cutoff), and residual high-frequency errors compare. The consistency of the mean distance between static and dynamic datasets suggests uniform error behavior, while the larger dynamic errors stem from factors such as motion blur, background gradients, and finite pixel-size effects.
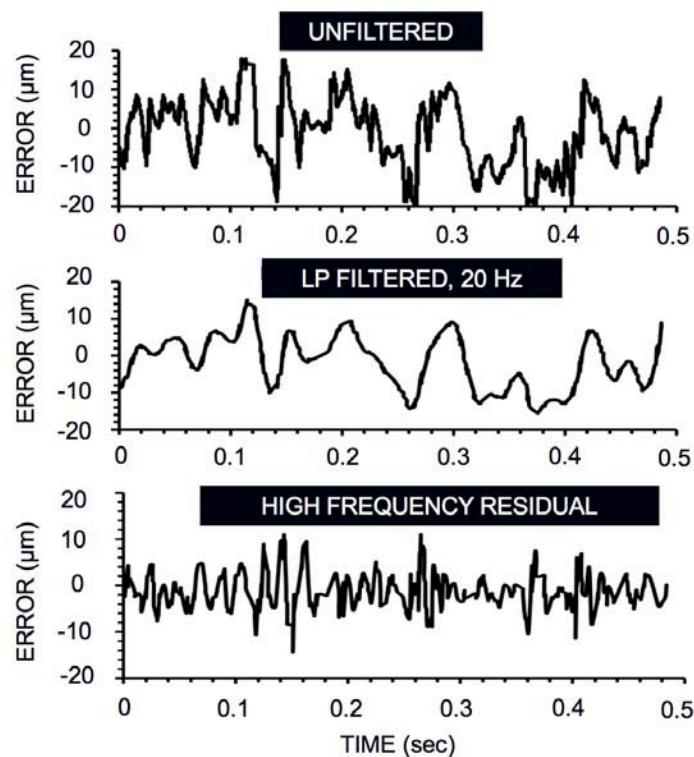
Figure 12: 3D errors in the dynamic cube study, shown as the difference between the inter-marker distance for each frame and the mean distance. Top: Unfiltered (total) errors; Middle: Errors after 20 Hz low-pass filtering; Bottom: Residual high-frequency errors.

Dynamic errors from all tests averaged ±0.015 mm (1/40th of the marker size), demonstrating the benefits of gray-scale centroids for finding marker centers with sub-pixel accuracy. 3D calibration and distortion correction were not significant factors, based on the uniformity of the errors across the field of view. Static errors (noise-dependent) were in the order of 0.01mm. Dynamic errors were higher than static errors. Motion blur, background effects and quantization errors due to the finite pixel size are the three most likely causes for this. Blur, caused by motion of the markers during the sampling interval, could shift the marker centroid positions. The 2D component of the error is a function of the relative velocity of the two markers parallel to the image plane – if they are moving at the same speed and direction in this plane, both marker centroids would be shifted by the same amount. The 3D distance between two of the test object markers was calculated for every frame in the movement sequence. Low frequency (LF) errors were determined by optimal low pass filtering (approx. 20 Hz) the raw errors. High frequency errors are the residual left after subtracting LF errors from the raw errors. The inter-marker distance would be zero. To estimate the error contribution from blur, the Z (vertical) component of the relative velocities of the two markers was calculated. This axis had the largest velocity component and is also parallel to both camera/intensifier image planes (maximizing the blur effect). The average

absolute difference in the Z component of velocity between the markers was 70 mm/s, causing a mean shift in the relative centroid positions of only 0.017 mm (at the 500 µs sample period). Dynamic error was also estimated for the compression testing described in figures 11, 13, 14. In this case dynamic error was expressed as gray level percentage difference of each marker's centroid gray level from frame to frame; this difference was found to be 2%. Centroid errors can also occur if the materials surrounding the marker are non-uniform in radiodensity. Each radiographic pixel represents the combined density of all objects along the path between the X-ray source and corresponding point on the image intensifier or panel. Thus, the surrounding composite materials will affect the intensity of each marker pixel. A background gradient (due to a curved composite surface or an oblique view of the cube) will shift the calculate ed centroid away from the true marker center. If the marker crosses a high-contrast object (metals or cube edge), the effect is greater. The low frequency (LF) errors appear to be due to this phenomenon. The frequency and timing of the spikes are similar to those seen in rotational movement plots – for example, the large "dip" in the LF error

corresponds almost exactly in time with a sudden 180° rotation about the Z axis, which then reverts to its previous angle in 0.3 s. Subtracting the LF errors from the total error produces a residual that resembles Gaussian noise. The magnitude of this noise is slightly higher than observed in the static test, due most likely to the finite pixel-size effects that cause small centroid shifts as the marker signature crosses pixel boundaries. The cube study represents the worst-case scenario, with a sharp-edged measurement object undergoing large rotations in all 3 axes and approaching the edges of the calibrated field. Even so, typical errors were in the order of 1/40th of the tantalum marker size. Errors appear to be dominated by the effects of changes in the radiographic background surrounding the marker. Thus, correction for background nonuniformity would appear to offer significant potential for improving accuracy. The other sources of error (noise and finite pixel size) were significantly improved by reducing the pixel size when we acquired higher-resolution images (fig. 13). The average marker area was apparently always greater in the high-resolution tests (fig. 13).
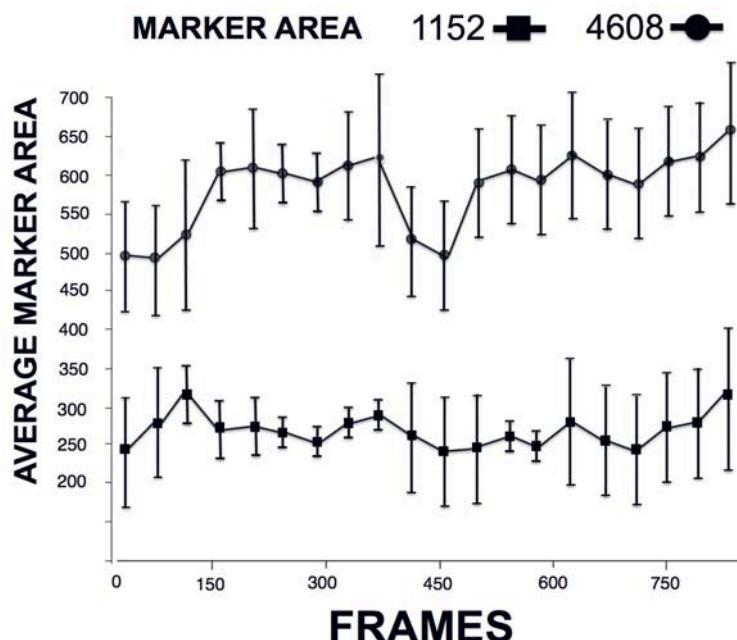
Figure 13: Comparison of average marker area between high-resolution (4608x4608-top) and low-resolution (1152x1152-bottom) tests, demonstrating improved centroid accuracy with smaller pixel sizes.

Dynamic imaging tests were conducted on various composite materials, ranging from small components to large, multipart assemblies, under destructive (DT) and non-destructive (NDT) conditions involving compression, tensile shocks, and strain experiments. Using the dynamic stereovideoradiography robotic tool, real-time deformation, strain, and shear behaviors were captured. Figures 7, 11, 14, and 15 illustrate these dynamic strain analyses, focusing particularly on the linear velocities and accelerations of individual grains in porous materials during DT and NDT compression (Figure 14). To complement these tests, 3D tomography was performed both before and after loading (Figure 15) to visualize any internal structural changes. In Figure 14, acceleration profiles of various grain structures (positions 1, 2, and 3 in blue, red, and green, respectively) demonstrate how impactful axial loading can produce initial high acceleration peaks (circled regions), which serve as early indicators of potential microcrack formation. A magnified view (middle) highlights these spikes in acceleration, pinpointing the region's most susceptible to crack initiation.

In the high-speed robotic dynamic imaging stereovideography destructive setup of fig. 14 a porous cement sample (approximately 70 × 30 × 10 mm) is placed under compression using an MTS 858 Bionix II testing device. By capturing stereo views of the sample, the system tracks individual grain movements and calculates 3D displacements with an accuracy of about 20 μm. This "4D" analysis combines real-time kinematic data with 3D tomography, enabling the measurement of localized strains, shear deformations, and potential microcrack initiation. High acceleration events (up to 500 cm/s²) are recorded, and initial acceleration peaks often signal areas prone to microcracking. Moreover, marker-based and markerless tracking methods can pinpoint the motion of tantalum (or lead) markers or distinct grain landmarks at speeds up to 20 m/s, achieving ±0.02 mm translational and ±0.18° rotational precision. These capabilities offer insights into how load magnitude, rate, and material composition collectively influence damage progression and structural integrity in composite systems [14], [27], [32], [53].
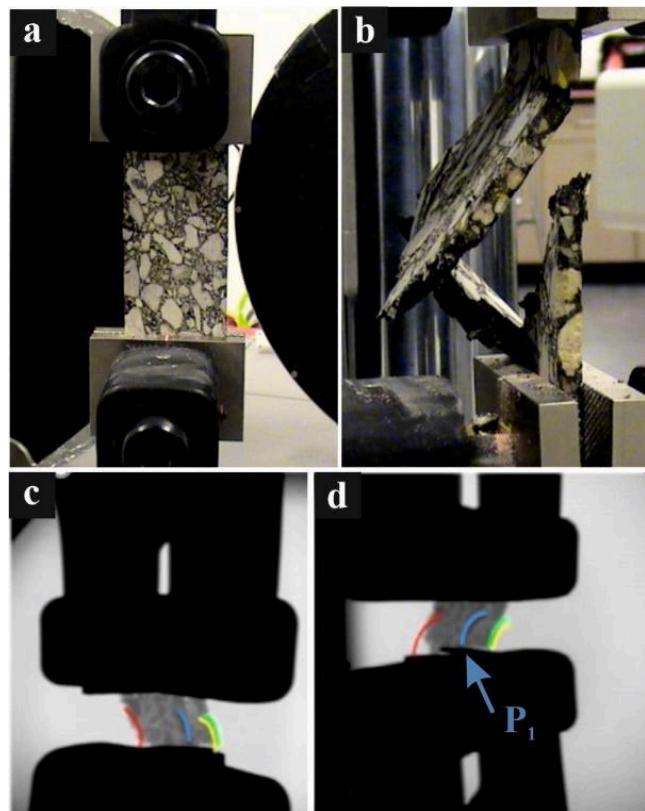
Figure 14: (A) High-speed robotic stereovideography imaging setup for DT/NDT compression testing (using an MTS 858 Bionix II device) on a porous cement sample (7 × 3 × 3 cm). (B) Close-up of the sample's grain structure, illustrating the variety of grain sizes. (C) and (D) Stereo-views of the sample, where individual grains can be tracked and their 3D displacements measured with approximately 20 μm accuracy.
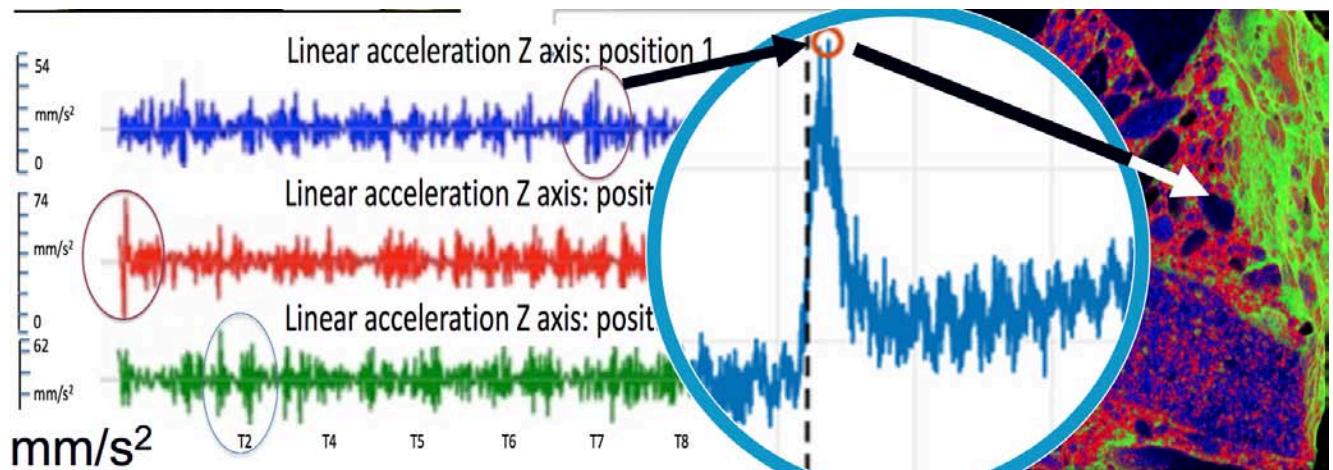
Figure 15: Left: Acceleration profiles identifying potential microcrack initiation sites; Right: color-coded map of internal microcrack formation in a composite sample.

Fig. 15 compares the acceleration profiles of various grain structures (left) with a color-coded map of microcrack initiation (right) in a composite sample subjected to impactful axial loading. The circled peaks in the acceleration signals highlight high-risk zones where microcracks are more likely to form. By fusing 3D CT data of the sample with the 3D kinematics of these high-acceleration regions, following the method presented in [21], [37], it becomes

Advanced Robotic Multimodal Imaging with Real-Time Motion Compensation for Dynamic Structural Health Monitoring

possible to generate an accurate map of internal microcrack initiation. The grains, represented as colored tetrahedra, correspond to areas of elevated acceleration and serve as indicators of potential microcrack nucleation sites. This integrated approach provides valuable insights into how loading parameters (magnitude, rate), part geometry, and material composition influence the onset and propagation of microcracks.

Fig. 16 illustrates a large-structure inspection and part-to-CAD comparison imaging approach applied to the outer exhaust duct of a jet engine—a component composed of synthetic fibers bound by resin. Because this large structure does not fit into conventional scanners, it must typically be disassembled and inspected part by part. The proposed method analyzes fiber anisotropy in high-strain regions, categorizing fibers according to their spatial orientation. In the *left* part of the figure, a plot shows the distribution of fiber orientations by angle (in degrees), indicating the proportion of fibers aligned at each angle. The *middle* part employs color-coding to highlight groups of fibers with different orientation angles, revealing areas where anisotropic behavior is most pronounced, and aiding in the detection of porosity, resin voids, or potential delamination. Finally, the *right* part focuses on the middle layer of fibers, demonstrating a perfectly aligned orientation. This analysis can be used in repetitive stress (fatigue/endurance) tests for these types of materials.
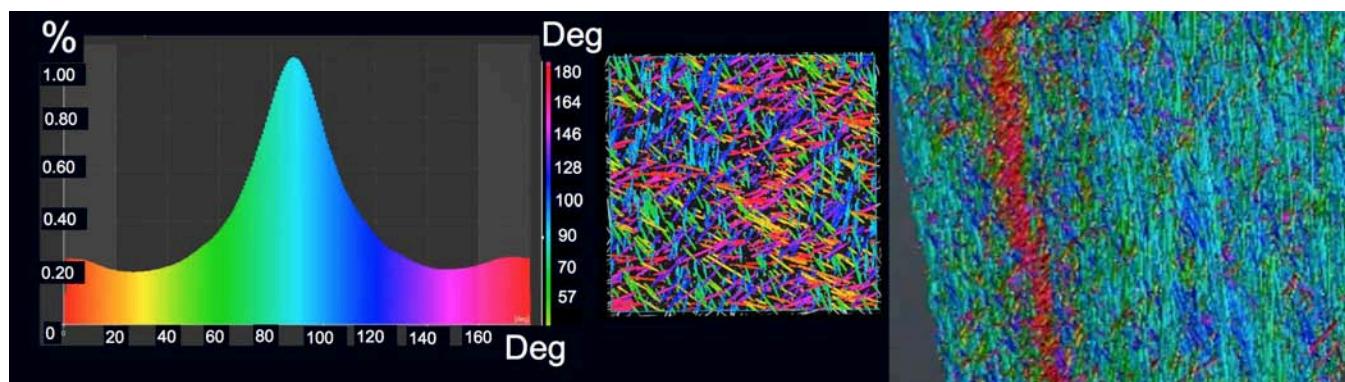
Figure 16: Fiber orientation distribution (left), color-coded orientations (middle), and magnified view (right) in a jet engine exhaust duct composite structure.

The Part-to-CAD (actual-to-nominal) comparison imaging mode was used to inspect large structures also without disassembling them. This enables the 3D CT scan data of a part to be overlaid with the original CAD model of the same part, allowing for detailed micro-comparisons. Fig. 17 provides a comprehensive illustration of the proposed non-destructive evaluation process. In fig. 17 (a), a single projection captured from a top view can be observed, which clearly shows the distribution of the fixators embedded within the airplane wing structure. Fig. 17 (b) presents a side projection of the same series of fixators, offering additional insight into their spatial arrangement and depth within the structure. The key advantage of this technique is that the 3D tomography scan can be conducted without disassembling the entire structure, meaning that each fixator can be evaluated in situ without the need to remove it for laboratory analysis. This enables to obtain detailed, accurate Geometric Dimensioning and Tolerancing (GD&T) reports that are critical for quality control and assurance. Fig. 17 (c) displays the 3D reconstructed geometry of each fixator, providing a precise model for further analysis. In fig. 17 (d), a close-up view highlights the differences at the edges between the nominal design and the actual manufactured parts, particularly at the threaded areas, with various colors used to indicate discrepancies. Finally, fig. 17 (e) demonstrates a dimensionality analysis where a specific option is exercised to compare the nominal dimensions to the actual measured values along the edges of the fixator. This analysis

is carried out with micro-tolerance precision (as fine as 10 µm), and the variability of these differences is presented as a plot along the edge of the material, offering a clear visual representation of the deviation profile.
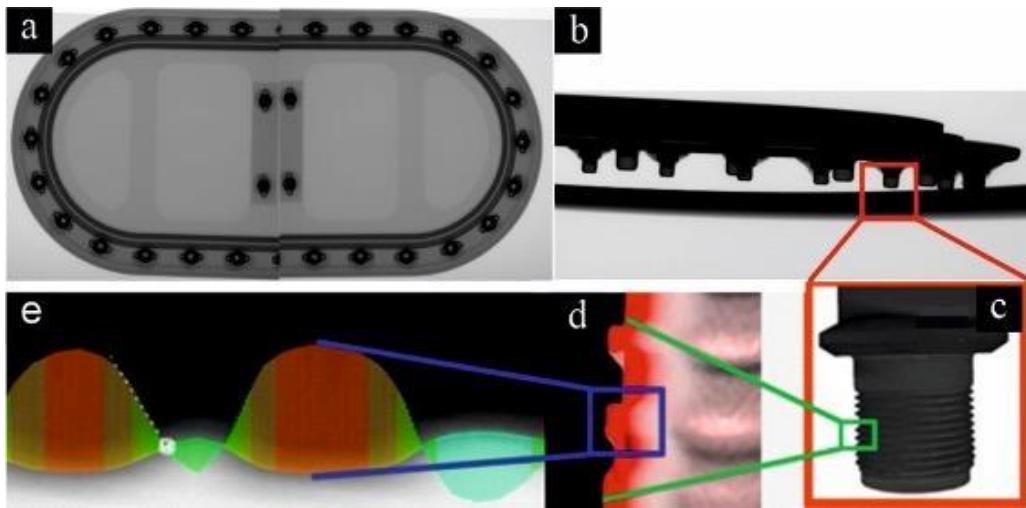
Figure 17: (a) Top view and (b) side view projections of a fixator deeply embedded in an airplane wing structure. (c) 3D reconstructed geometry of the fixator; (d) Close-up showing edge differences between nominal and actual parts (thread) with color indications; (e) Dimensionality analysis comparing nominal and actual edge dimensions with micro-tolerance (10 µm) precision, plotted along the edge.

Data acquisition was completed in approximately 30 seconds for objects within a 2 m³ field of view, with 3D reconstructions processed almost in real-time (5-8 seconds including raw data processing and storage). The logged time of previous handling and disassembly labor for that plane part (fig. 17) can take as much as ten days [23]. This initial robotic method for inspection dropped the time to less than half a day including handling and positioning of the robotic scanner around the target. It should be noted that for larger objects, such as a jet engine exhaust duct, inspection durations ranged from 30 minutes to three hours given the need for higher -out of plane resolution i.e., "data density"-, and the need for repeating the tests with alternative trajectories of the emitters/detectors to avoid missing parts of the object. These alternative trajectories were need for calculations for occlusion scenarios and exposure trial and error for optimization of SNR so there was the minimum trade-off and no reduction of spatial resolution. This significant multifold reduction in scan time, comparing to current procedures, is primarily due to the elimination of extensive sample preparation and disassembly. These procedures in conventional imaging techniques can last from several hours, to days or even months, as in the case of Maintenance, Repair, and Overhaul (MRO) A, B, C, D airplane checks [23], depending on the size and complexity of the target.

The perovskite detector option presented here has been reported to exhibit the lowest detectable dose rate of 13 nGyair s⁻¹ in previous studies, which is over 400-times lower than the medical diagnostic baseline without deterioration in the image quality [39]. Detection efficiency of 88% and noise-equivalent dose of 90 pGy air were also obtained with up to 18 keV X-rays, allowing single-photon-sensitive, low-dose and energy-resolved X-ray imaging. Array detectors like this demonstrate high spatial resolution up to 11 lp mm⁻¹ [60], [67]. Although we did not test these performance characteristics, we note that the detectors were used here in the same configurations and in additional configurations that the radiology dose was tripled or even quadrupled. However, we need to stress that we did not do radiographic dose calibration in the present study.

Advanced Robotic Multimodal Imaging with Real-Time Motion Compensation for Dynamic Structural Health Monitoring

IV.   DISCUSSION

CT is finding an increasing acceptance in the TIC landscape, largely due to the evolution of its components associated with resolution, focal point sizes, detector quality, all of which are need in advanced inspection processes. However certain problems still prohibit its widespread use in inspection related processes, including dynamic accuracy, workflow, gantry size as they translate in the inability to scan large sized assembled targets comprised of composite materials. Robotics-driven multimodal imaging is an alternative to traditional industrial CT scanning that can help resolve some these challenges. It can combine a series of different imaging modes in one device offering the opportunity to accurately fuse static 3D images (morphology) with deformation and strain data obtained during DT and ND imaging-based testing. This level of automation can help shine light on an actual part, even if it is of large size, resolving internal structures that can be viewed digitally. These internal parts can be visualized and measured with high accuracy, without sectioning or disassembling the actual part from the larger structure that contains it.

Inspection of aerospace components, welds in pipes, airplane engines, wings, landing gear and containers can be a demanding imaging task dealing with thick deep layered and/or very dense materials. Typically, hard-to-handle high-energy isotope sources are needed to produce sufficient image quality in reasonable time. Conventional X-ray imagers rely on thicker or specialized high energy scintillators. The trade-off is typically loss of spatial resolution and very laborious time-consuming processes to gather the images. The method presented here offers novel direct conversion technology that preserves spatial resolution even when using a thicker converter layer for improved efficiency in high energy inspection. The necessary geometric trajectory (placement) of this kind of panel detection, however, and its proximity to these highly irregularly shaped structures has been a challenge in the TIC industry. Other challenges include huge scanning times, inability to scan with load bearing and motion, accurate dynamic control of exposure/magnification, and laborious logistics to coordinate disassembly of large components so they can be brought into the laboratory. Even at the laboratory, conventional CT scanners have small-sized gantries for most of these structures. Some structures must also be studied under realistic working conditions. This means impact, vibration or motion at high speeds and load bearing conditions that alter the morphology of the object based on the rate and magnitude of loading, that eventually cause motion artifacts, blurry images, and exposure challenges during imaging.

The method presented here can inspect thicker or denser structures with high throughput and a multifold reduction in the scanning time) using the photon counting detectors and specialized emitting systems with optimized relationships between focal spot, exposure, detector binning and absorption. The most important solution however, is mainly the ability to control the dosage and compensate for the motion artifacts. Our future studies ought to investigate the interplay of these parameters so that this tool can be fully characterized for a variety of scanning protocols. Automation can help resolve this multiparametric characterization challenge. Robotics-driven imaging can offer combinations of different emitters and detectors in a unique "one-system-many-modalities" imager. The system, therefore, has the potential to unite all these old and new inspection methods in a common reference, both in terms of coordinate systems representing and normalizing the data (fig. 1, 3) and in terms of a hybrid comprehensive inspection platform. The X-Ray data acquisition rate varies, depending on the target and the modality, from 1 to 10000 fps and the angular speed of the robotic system may vary from 1 and up to 30 degrees per second. If we add the robotic arms positioning time that can take from a few minutes and up to an hour (based on target size) the total inspection time can be less than two hours with the actual scan duration ranging from 6 seconds to 30 minutes. In a worst-case scenario that multiple trajectories need to be employed for a complicated composite part like an aircraft structure, the total scanning duration can be half

a day including handling and positioning of the robotic scanner around the target. These durations, however, remove from the overall inspection logistics the many hours, and in some cases days, even months required for disassembling of large non-axisymmetric structures so that scanning is possible in conventional small gantry scanners. When imaging occlusion becomes a problem in the presented set-up, a different robotic arm trajectory is selected, and the occluded viewpoint can be bypassed. Fitting a system like this on a mobile robotic imaging station trailer in the future can make this system a mobile TIC facility with flexible open scanning architecture that can approach large structures (planes, pipelines etc.), significantly improving their inspection tasks.

A 3D model-based kinematics tracking method was presented in detail as it can help assess the kinematics of a composite target in motion with microlevel accuracy. The method can work for the deep layers of structures as they are visualized with high-speed sequences of biplane radiographs from specialty detectors. The method is based upon optimizing similarity between the radiographic image pairs and digitally reconstructed radiographs (DRRs) generated by projections through a 3D target (generated from CT). However, the matching between DRRs and actual radiographic images can never be exact. The radiographic images result from a combination of the extent of absorption of the different layers of the composite structures, and some the level of obstruction of some internal structure on the outmost edges of the target. In contrast, the exact outmost edges of the target can be obtained from the CT volume data, from which certain parts of the composite can be removed. This causes an apparent difference in size between real radiographic images and DRRs (the projected target looked bigger than the target in the radiographic images). This difference varies by frame and is difficult to correct unless we collect radiographic sequences using alternative trajectories which in turn is only possible with an alternative pathway taken by the robotic arms. The high-resolution capacity of the detector has a significant effect on the reduction of these

differences and need to be investigated more in a future study. Single-plane implementation of the algorithm resulted in target position estimates farther away from the X-ray source than the absolute position determined using stereo information or marker-based tracking (fig. 10). Thus, assessment of movement perpendicular to the image detector was unreliable with a single-plane system. In figure 10, the target was estimated 2 mm farther away from the X-ray source of the left system, causing 0.9 mm errors for X axis and 1.9 mm errors for Y axis in the reference coordinate system. By combining results from the two views or even more that two trajectories, errors in the beam axis direction are reduced to a level similar to those in the image plane.

The two-line segments connecting each projection source and the coordinates of its projections onto the corresponding image plane should theoretically intersect at a point. But these vectors can some times not cross, due to small errors from various sources (see fig. 10). During the controlled experiments with the cube described above, these two lines typically missed crossing by only about 0.01 mm in each axis. Single-plane systems may be somewhat better for estimating target rotation, since 3D rotations calculated separately for each system typically differed by only about 0.03° (after the estimated orientation from each single-plane system was transformed to the common reference coordinate system).

When information from both views was combined, the relative differences between model-based tracking and marker-based tracking data were approximately 0.02 mm for the cube experiment for all axes. These errors are similar in magnitude to the effective pixel size of the radiographic images. This suggests that radiographic image resolution may be a limiting factor for accuracy, and higher resolution cameras and/or the addition of subpixel matching techniques can improve performance.

It should be noted that this open system architecture enables also dynamic binning options, which in turn allow the same detectors to be used for different imaging modalities with

higher resolution results. Binning eventually improves the signal to noise ratio and provides better total image contrast resolution, with the trade-off being reduced spatial resolution. The two magnification modes however (geometrical and optical) can be applied with a tomosynthesis scan of the object in question at the exact same testing set up adding only 30s to 5 minutes of extra imaging time depending on the size of the target. Tomosynthesis provides however, the high-spatial microCT level resolution data that the previous scanning options could not deliver without having to disassemble the part, and/or move it to another scanner in a different laboratory site. More work in the future is required to demonstrate the effects of binning, optical magnification and tomosynthesis in industrial imaging.

The blur-motion artifact solution i.e., the capacity to directly measure the 3D morphology of a structure under loading/movement conditions (up to 20 m/s speeds) opens a new chapter in the hypotheses underlying the material characterization instrumentation. We believe that much more work is required to reach a golden standard of this methodologies for the plurality of objects and conditions that it can be applied to. An enormous calibration task lies ahead with regards to thickness of specific materials and their composition. Another advantage of controlling the exposure during different stages of the trajectory of the emitter/detector couple is that it offers an indirect way to control the frequency dependence on attenuation. Controlling dynamically the focal spot- combined with optical magnification with special lensing systems that in turn have dynamically controlled amplitude, delivers micro-CT capabilities for the first time outside the laboratory and for on-site inspection. More work ought to be performed to demonstrate this capability in detail in a separate study. The spatial resolution (sharpness) alternative is offered where contrast conditions are not ideal. Image "density" (out of plane resolution) can be drastically improved and several times greater than in a conventional system. This is possible because the robotic arms and data acquisition speed can be altered to collect hundreds of thousands of projections if needed. In the metanalysis only the projections need for proper reconstruction are selected, potentially removing the inappropriate motion error projections. The radiographic quantum mottle effects or noise can be tackled by having the grid system, tubes, and collimators of each emitter fire not in synchronicity but with time latencies so the signals from the two different tubes in the stereo system do not cross and do not collide [51]. Its assessment needs also quantification in a dedicated study.

A new challenge, however, is associated with the capacity for continuous, autonomous, and excessive use of the detectors and significant need for cooling structures on the tubes. The system literally "burns" very fast through detectors as it is using them at the top of their capacity all the time. That introduces panel disadvantages (as compared to image intensifiers -IIs) that include defective image elements, higher costs and lower spatial resolution if they do not get replaced on time (at least twice annually for a constantly scanning device).

The present alternative tool for non-destructive inspection, composition analysis and analysis of carbon fiber parts helps locate the exact axis and point of porosity, resin voids and delamination within complex geometries inside of carbon fiber. Alternatively, it offers reverse engineering and tolerance mapping methods when the CAD model of the part is not known and needs to be approximated from existing geometry. The new robotic imaging system demonstrated an alternative way to study fatigue, impact and any associated deformation, linear expansion or phase change that a material experiences due to the application of different forces at different loading rates using image-based NDT. The time savings of these new methods described here contribute to drastically lower labor requirements and can increase the capacity of a single system, so more parts could be inspected.

V. CONCLUSION

In conclusion, the proposed robotic multimodal imaging system presented in this study offers a transformative approach for inspecting large

aerospace structures and complex-shaped objects. By integrating advanced motion compensation and dynamic kinematics tracking, the system significantly reduces scan times, improves workflow efficiency, and lowers inspection costs while delivering high-resolution analyses of key material properties such as porosity, dimensionality, and failure modes.

The ability to automatically stitch 2D/3D radiographic images into panoramic views of large, non-axisymmetric objects further enhances its utility for reverse engineering and comprehensive quality control. Comparative evaluations between marker-based and markerless motion tracking methods indicate that the markerless approach achieves comparable accuracy, demonstrating its potential for more streamlined and less invasive inspections.

These findings have broad implications, with applications extending beyond aerospace to fields like defense, cargo safety, petrochemical logistics, and medical device manufacturing. Future studies will focus on validating the system using a library of standardized target models tailored to specific density and absorption characteristics. This effort aims to establish a simplified, expedited, and cost-efficient standard for dynamic inspection protocols in both laboratory and on-site environments.

ACKNOWLEDGEMENTS

REFERENCES

1. N. Michailidis, F. Stergioudi, H. Omar, and D. N. Tsipas, "An image-based reconstruction of the 3D geometry of an Al open-cell foam and FEM modeling of the material response," *Mechanics of Materials*, vol. 42, no. 2, 2010, doi: 10.1016/j.mechmat.2009.10.006.

2. S. Gholizadeh, "A review of non-destructive testing methods of composite materials," *Procedia Structural Integrity*, vol. 1, pp. 50–57, 2016, doi: 10.1016/j.prostr. 2016.02. 008.

3. B. Wang, S. Zhong, T.-L. Lee, K. S. Fancey, and J. Mi, "Non-destructive testing and evaluation of composite materials/structures: A state-of-the-art review," *Advances in Mechanical Engineering*, vol. 12, no. 4, p. 168781402091376, Apr. 2020, doi: 10.1177/ 1687814020913761.

4. S. C. Garcea, I. Sinclair, S. M. Spearing, and P. J. Withers, "Mapping fibre failure in situ in carbon fibre reinforced polymers by fast synchrotron X-ray computed tomography," *Compos Sci Technol*, vol. 149, pp. 81–89, Sep. 2017, doi:10.1016/j.compscitech.2017.06.0 06.

5. S. Borkowski and K. Knop, "Challenges Faced in Modern Quality Inspection," *Management and Production Engineering Review*, vol. 7, no. 3, pp. 11–22, Sep. 2016, doi: 10.1515 /mper-2016-0022.

6. N. Michailidis, F. Stergioudi, G. Maliaris, and A. Tsouknidas, "Influence of galvanization on the corrosion fatigue performance of high-strength steel," *Surf Coat Technol*, vol. 259, pp. 456–464, Nov. 2014, doi: 10.1016/ j.surfcoat.2014.10.049.

7. S. C. Garcea, Y. Wang, and P. J. Withers, "X-ray computed tomography of polymer composites," *Compos Sci Technol*, vol. 156, pp. 305–319, Mar. 2018, doi: 10.1016/j.comp scitech.2017.10.023.

8. J. E. See, C. G. Drury, A. Speed, A. Williams, and N. Khalandi, "The Role of Visual Inspection in the 21st Century," *Proceedings*

Advanced Robotic Multimodal Imaging with Real-Time Motion Compensation for Dynamic Structural Health Monitoring

of the Human Factors and Ergonomics Society Annual Meeting, vol. 61, no. 1, pp. 262–266, Sep. 2017, doi: 10.1177/ 15419312 13601548.

9. X. Xu *et al.*, "A systematic review of ultrasonic techniques for defects detection in construction and building materials," *Measurement*, vol. 226, p. 114181, Feb. 2024, doi: 10.1016/ j.measurement.2024.114181.

10. S. K. Dwivedi, M. Vishwakarma, and Prof. A. Soni, "Advances and Researches on Non Destructive Testing: A Review," *Mater Today Proc*, vol. 5, no. 2, pp. 3690–3698, 2018, doi: 10.1016/j.mat pr.2017.11.620.

11. E. Marble and T. Boles, "A Review of the Structural Characteristics of Aerospace Composites," *Science Insights*, vol. 41, no. 7, pp. 749–753, Dec. 2022, doi: 10.15354/ si.22.re102.

12. H. Kim, Y. Lin, and T.-L. B. Tseng, "A review on quality control in additive manufacturing," *Rapid Prototyp J*, vol. 24, no. 3, pp. 645–669, Apr. 2018, doi: 10.1108/RPJ-03-2017-0048.

13. Y. Fu and X. Yao, "A review on manufacturing defects and their detection of fiber reinforced resin matrix composites," *Composites Part C: Open Access*, vol. 8, p. 100276, Jul. 2022, doi: 10.1016/j.jcomc.2022.100276.

14. N. Baka *et al.*, "Evaluation of automated statistical shape model based knee kinematics from biplane fluoroscopy," *J Biomech*, vol. 47, no. 1, pp. 122–129, Jan. 2014, doi: 10.1016/j.jbiomech.2013.09.022.

15. M. Jolly *et al.*, "Review of Non-destructive Testing (NDT) Techniques and their Applicability to Thick Walled Composites," *Procedia CIRP*, vol. 38, pp. 129–136, 2015, doi: 10.1016/j.procir.2015.07.043.

16. ASTM E2033-17, "Standard Practice for Radiographic Examination Using Computed Radiography (Photostimulable Luminescence Method)."

17. C. Tuloup, W. Harizi, Z. Aboura, Y. Meyer, K. Khellil, and R. Lachat, "On the use of in-situ piezoelectric sensors for the manufacturing and structural health monitoring of polymer-matrix composites: A literature review," *Compos Struct*, vol. 215, pp. 127–149,

May 2019, doi: 10.1016/j.compstruct .2019 .02.046.

18. P. F. Tavares, S. C. Leemann, M. Sjöström, and Å. Andersson, "The MAX IV storage ring project," *J Synchrotron Radiat*, vol. 21, no. 5, pp. 862–877, Sep. 2014, doi: 10.1107/ S1600577514011503.

19. ASTM E2662: 2015, "Standard practice for radiographic examination of flat panel composites and sandwich core materials used in aerospace applications," 2015.

20. Herman. J. Woltring, P. van Roy, M. Hebbelinck, M. Osteaux, and L. Verbruggen, "3-D knee joint kinematics by magnetic resonance imaging," *J Biomech*, vol. 23, no. 4, p. 384, Jan. 1990, doi: 10.1016/0021-9290 (90)90127-O.

21. G. Papaioannou, A motion correction method for the moving target in robotic radiographic 2D and 3D imaging and robotics-driven computed tomography and other imaging modalities: Patent #20130100820, May 15, 2024.

22. L. Lucchetti, A. Cappozzo, A. Cappello, and U. Della Croce, "Skin movement artefact assessment and compensation in the estimation of knee-joint kinematics," *J Biomech*, vol. 31, no. 11, pp. 977–984, Nov. 1998, doi: 10.1016/S0021-9290(98)00083-9.

23. L. Lemieux, R. Jagoe, D. R. Fish, N. D. Kitchen, and D. G. T. Thomas, "A patient-to-computed-tomography image registration method based on digitally reconstructed radiographs," *Med Phys*, vol. 21, no. 11, pp. 1749–1760, Nov. 1994, doi: 10.1118/1.597276.

24. J. Weese, G. P. Penney, P. Desmedt, T. M. Buzug, D. L. G. Hill, and D. J. Hawkes, "Voxel-based 2-D/3-D registration of fluoroscopy images and CT scans for image-guided surgery," *IEEE Transactions on Information Technology in Biomedicine*, vol. 1, no. 4, pp. 284–293, 1997, doi: 10.1109/ 4233.681173.

25. W. Burton, C. Myers, M. Stefanovic, K. Shelburne, and P. Rullkoetter, "Scan-Free and Fully Automatic Tracking of Native Knee Anatomy from Dynamic Stereo-Radiography with Statistical Shape and Intensity Models,"

Ann Biomed Eng, vol. 52, no. 6, pp. 1591–1603, Jun. 2024, doi: 10.1007/s10439 -024-03473-5.

26. B. Prentice et al, "OliverWyman (2024), 'Global fleet and MRO market forecast (2024-2034)', accessed in 2025 in www.oliverwyman.com.

27. G. Papaioannou, G. Nianios, C. Mitrogiannis, D. Fyhrie, S. Tashman, and K. H. Yang, "Patient-specific knee joint finite element model validation with high-accuracy kinematics from biplane dynamic Roentgen stereogrammetric analysis," *J Biomech*, vol. 41, no. 12, pp. 2633–2638, Aug. 2008, doi: 10.1016/j.jbiomech.2008.06.027.

28. G. Papaioannou, M. Bottum, and G. Fiedler, "Menisci displacement under joint load," *J Biomech*, vol. 40, no. 2, p. S158, 2007.

29. G. Papaioannou *et al.*, "Finite Element Modeling of the osteochondral defects in the human knee: Influence of defect size on cartilage rim stress and load redistribution to adjacent cartilage," in *Advances in Scattering and Biomedical Engineering*, WORLD SCIENTIFIC, Jul. 2004, pp. 541–549. doi: 10.1142/9789812702593_0057.

30. P. Beillas, "A new method to investigate in vivo knee behavior using a finite element model of the lower limb," *J Biomech*, vol. 37, no. 7, pp. 1019–1030, Jul. 2004, doi: 10.1016/S0021-9290(03)00435-4.

31. G. Papaioannou, C. K. Demetropoulos, and Y. H. King, "Predicting the effects of knee focal articular surface injury with a patient-specific finite element model," *Knee*, vol. 17, no. 1, pp. 61–68, Jan. 2010, doi: 10.1016/j.knee.2009.05.001.

32. G. Papaioannou, *et al.* (2011). Dynamic Radiography Imaging as a Tool in the Design and Validation of a Novel Intelligent Amputee Socket. In: Tavares, J., Jorge, R. (eds) Computational Vision and Medical Image Processing. Computational Methods in Applied Sciences, vol 19. Springer, Dordrecht. https://doi.org/10.1007/978-94-007-0011-6_5.

33. G. Papaioannou, C. Mitrogiannis, G. Nianios, and G. Fiedler, "Assessment of amputee socket–stump–residual bone kinematics during strenuous activities using Dynamic Roentgen Stereogrammetric Analysis," *J Biomech*, vol. 43, no. 5, pp. 871–878, Mar. 2010, doi: 10.1016/j.jbiomech.2009.11.013.

34. G. Papaioannou, "Automated radiographic imaging system and method for multimodal imaging protocols with motion correction system," Patent #2013,010,0811, May 25, 2023.

35. J. Neider, T. Davis, and M. Woo, *OpenGL Programming Guide. Reading MA*. 1998.

36. Papaioannou, G. A Robotics-driven Multimodal Imaging System for Quality Inspection. Proceedings of the Plenary Technical Invited Talk and Paper at the 73rd College International pour la Recherche en Productique (CIRP) General Assembly in Thessaloniki, Thessaloniki, Greece, 18–24 August 2024.

37. G. Papaioannou, "Robotic multi-mode radiological scanning system and method," Patent #15/082,854, May 06, 2016.

38. "KINEMAGINE Helios Robotic Imaging system, Brochure and KINEDOSE Operating manual," 2022.

39. X. Lu *et al.*, "High-Performance Flat-Panel Perovskite X-ray Detectors Enabled by Defect Passivation in Ruddlesden–Popper Perovskites," *ACS Appl Mater Interfaces*, vol. 16, no. 11, pp. 14006–14014, Mar. 2024, doi: 10.1021/acsami.4c00232.

40. J. Fuller, L.-J. Liu, M. C. Murphy, and R. W. Mann, "A comparison of lower-extremity skeletal kinematics measured using skin- and pin-mounted markers," *Hum Mov Sci*, vol. 16, no. 2–3, pp. 219–242, Apr. 1997, doi: 10.1016/S0167-9457(96)00053-X.

41. S. Tashman, K. DuPre, H. Goitz, T. Lock, P. Kolowich, and M. Flynn, "A digital radiographic system for determining 3D joint kinematics during movement," in *19th Ann. Meeting Amer. Soc. Biomech.*, Stanford, CA: ASB Press, 1995.

42. S. Tashman, W. Anderst, and P. Kolowich, "Severity of OA related to magnitude of dynamic instability in ACL-deficient dogs," in *roc. 46th Annu. Meeting Orthop. Res. Soc.*, Orlando, FL, 2000, p. 257.

43. H. J. Woltring, "Planar control in multi-camera calibration for 3-D gait studies," *J Biomech*, vol. 13, no. 1, pp. 39–48, Jan. 1980, doi: 10.1016/0021-9290(80)90006-8.

44. N. W. John, "Volume Rendering," 2002, pp. 35–41. doi: 10.1007/978-3-642-59438-0_5.

45. W. Schroeder, K. Martin, and B. Lorensen, *The VTK Book*. Kitware, 2006.

46. D. LaRose, J. Bayouth, and T. Kanade, "Transgraph: interactive intensity-based 2D/3D registration of x-ray and CT," in *Proc. SPIE Med. Imag. '2000 Image Processing*, K. M. Hanson, Ed., Jun. 2000, pp. 385–396. doi: 10.1117/ 12.387700.

47. G. Papaioannou, "Method for the control of collimation, penumbra, dynamic exposure, and dosage in a number of robotics-driven 2D radiology and 3D computer tomography and other multimodality imaging," Patent #2013,010,0822, May 25, 2024

48. B. Clark, *Data Visualization Toolkit: Using JavaScript, Rails™, and Postgres to Present Data and Geospatial Information*. New York: Pearson Education, Inc., 2017.

49. W. O. Thompson, F. L. Thaete, F. H. Fu, and S. F. Dye, "Tibial meniscal dynamics using three-dimensional reconstruction of magnetic resonance images," *Am J Sports Med*, vol. 19, no. 3, pp. 210–216, May 1991, doi: 10.1177/ 036354659101900302.

50. J. G. Tamez-Pena, S. Totterman, and K. J. Parker, "Kinematic analysis of musculoskeletal structures via volumetric MRI and unsupervised segmentation," in SPIEMed.Imag.'99: Physiology and Function from Multidimensional Images, San Diego, CA, Feb. 1999.

51. Papaioannou, G.; Mitrogiannis, C.; Schweitzer, M.; Michailidis, N.; Pappa, M.; Khosravi, P.; Karantanas, A.; Starling, S.; Ruberg, C. Towards the Performance Characterization of a RoboticMultimodal Diagnostic Imaging System. J. Imaging 2025, 11, 147 https://doi .org/10.3390/jimaging110 50147

52. ANSA BETA CAE systems software suite, Switzerland, https://www.beta-cae.com/, 2024."

53. G. Papaioannou, C. Mitrogiannis, G. Nianios, and G. Fiedler, "Tracking high speed arthrokinematics using a new and high resolution Biplane Dynamic Roentgen Stereogrammetric method," *International Journal of Imaging 2. A09*, vol. 2, no. A09, pp. 66–85, 2009.

54. B. Preim and C. P. Botha, *Visual Computing for Medicine, 2nd Edition*. 2013.

55. M. K. Bhuyan, *Computer Vision and Image Processing: Fundamentals and Applications*. Routledge, 2019.

56. M. Sonka, V. Hlavac, and R. Boyle, *Image Processing, Analysis and Machine Vision*, 4th ed. Stamford, CT, USA: CENGAGE Learning, 2015.

57. G. R. Sinha, *Modern Optimization Methods for Science, Engineering and Technology*. UK: IOP Publishing, 2020.

58. S. Ghafurian, D. N. Metaxas, V. Tan, and K. Li, "Fast generation of digitally reconstructed radiograph through an efficient preprocessing of ray attenuation values," in *SPIE Medical Imaging*, 2016.

59. G. P. Penney, J. Weese, J. A. Little, P. Desmedt, D. L. G. Hill, and D. J. hawkes, "A comparison of similarity measures for use in 2-D-3-D medical image registration," *IEEE Trans Med Imaging*, vol. 17, no. 4, pp. 586–595, 1998, doi: 10.1109/42.730403.

60. W. H. Press, S. A. Teukolsky, W. T. Vetterling, and B. T. Flannery, *Numerical Recipes in C: The Art of Scientific Computing*, 3rd ed. Cambridge University Press, 2007.

61. S. A. Banks and W. A. Hodge, "Accurate measurement of three-dimensional knee replacement kinematics using single-plane fluoroscopy," *IEEE Trans Biomed Eng*, vol. 43, no. 6, pp. 638–649, Jun. 1996, doi: 10.1109/10.495283.

62. W. J. Suntay, E. S. Grood, M. S. Hefzy, D. L. Butler, and F. R. Noyes, "Error Analysis of a System for Measuring Three-Dimensional Joint Motion," *J Biomech Eng*, vol. 105, no. 2, pp. 127–135, May 1983, doi:10.1115/1.31 38396.

63. P. Bourke, "The shortest line between two lines in 3D. Availiable:http://www. swin.edu. au/astronomy/pborke/geometry/lineline3d/."

64. J. J. Craig, *Introduction to Robotics Mechanics & Control*, 4th ed. Pearson, 2017.

65. T. R. Kane, P. W. Likins, and D. A. Levinson, *Spacecraft Dynamics*. New York: McGraw-Hill, 1983.

66. B. Siciliano and O. Khatib, *Springer Handbook of Robotics*. Cham: Springer International Publishing, 2016. doi: 10.1007/978-3-319-32552-1.

67. K. Sakhatskyi *et al.*, "Stable perovskite single-crystal X-ray imaging detectors with single-photon sensitivity," *Nat Photonics*, vol. 17, no. 6, pp. 510–517, Jun. 2023, doi: 10.1038/s41566-023-01207-y.

This page is intentionally left blank

Enhancing Learning Through Game Flow: A Case Study for Epistemic Game "Working with Water"

Dr. Mengfan Zou

ABSTRACT

Epistemic video games, interpreted as video games pursuing new knowledge through the mechanism that concatenates practices and cognition, grab numerous attention on account of their extensive implementation since COVID-19. The corresponding academic explorations into the players, especially indicating the students, have largely integrated in game enjoyment and the principals exerted. Understanding the essential factors that promote game enjoyment that aligns with educational purposes is crucially important for clarifying the mechanism of epistemic games. Consequently, the present study adopts the GameFlow model presented by Sweetser and Wyeth (2005), whose accuracy has been verified and yields to evaluate enjoyment of video games by examining specific criteria under eight elements: concentration, challenge, player skills, control, clear goals, feedback, immersion, and social interaction of the model. The highly acclaimed epistemic game "Working with Water" is elected to conduct a case study by implementing the GameFlow model. The result indicates that the overall values for GameFlow cohere with the performance, usability, and potentiality of the epistemic games. The model performs well in the evaluation of epistemic games to a large extent. but simultaneously limited to the intrinsic harshness of the specific genre that differs from others in the degree of enjoyment. As a result, the evaluating model based on GameFlow is worthy of inquiry in an educational context for further investigation.

Keywords: epistemic games, learning, gameflow, case study, game evaluation.

Classification: LCC Code: LB1029.G3

Language: English

Enhancing Learning Through Game Flow: A Case Study for Epistemic Game "Working with Water"

Dr. Mengfan Zou

ABSTRACT

Epistemic video games, interpreted as video games pursuing new knowledge through the mechanism that concatenates practices and cognition, grab numerous attention on account of their extensive implementation since COVID-19. The corresponding academic explorations into the players, especially indicating the students, have largely integrated in game enjoyment and the principals exerted. Understanding the essential factors that promote game enjoyment that aligns with educational purposes is crucially important for clarifying the mechanism of epistemic games. Consequently, the present study adopts the GameFlow model presented by Sweetser and Wyeth (2005), whose accuracy has been verified and yields to evaluate enjoyment of video games by examining specific criteria under eight elements: concentration, challenge, player skills, control, clear goals, feedback, immersion, and social interaction of the model. The highly acclaimed epistemic game "Working with Water" is elected to conduct a case study by implementing the GameFlow model. The result indicates that the overall values for GameFlow cohere with the performance, usability, and potentiality of the epistemic games. The model performs well in the evaluation of epistemic games to a large extent. but simultaneously limited to the intrinsic harshness of the specific genre that differs from others in the degree of enjoyment. As a result, the evaluating model based on GameFlow is worthy of inquiry in an educational context for further investigation.

Keywords: epistemic games, learning, gameflow, case study, game evaluation.

I.   INTRODUCTION

Confronted with challenges caused by COVID-19, conventional education in classrooms has been hindered by geographical constraints during the quarantines. In response to the circumstances, increasing recognition of the urgent demand for supportive technologies is advocated to complement and enhance the learning experience. Among all the alternatives, epistemic games stand out owing to their incomparable accessibility and brilliant performance (Parviainen et al. 2021).

Explorations to epistemic games have been a common interest in the academy in recent years, students who   identify with players create unprecedented opportunities and challenges, sequestered education has gradually   been substituted by virtual schooling (Shaffer et al., 2005). To better understand the mysterious enchantment of video games, numerous studies have focused on the concept of player enjoyment.

The GameFlow model proposed by Sweetser and Wyeth (2005) is adopted in the present study, evaluating an epistemic game "Working with Water", aiming to evaluate the serious genre of games, meanwhile providing an illusion for promoting a comprehensive model, particularly for educational games.

II.   LITERATURE REVIEW

2.1 Evaluation of game enjoyment

Player enjoyment has been the central focus of game study since the past decade. In the interactive context, challenge and accomplishment are major cognitive yet sentimental appeals reasoning an individual's

choice of gaming, the judgment is proved as the result of the configuration of in-game competence degrees that concentrate on gamers' involvement (Vorderer et al., 2004). Addedly, Vorderer et al. (2004) refer to the disparities in patterns of entertainment, indicating that the procedures of being entertained differ in gamer and game genres. Specifically, in regard to educational games' enjoyment features, Gee (2005) insists on establishing adequate challenge and accomplishment for performing better in enjoyable learning procedures, video games composed of moderate difficulties, decent guidance, and skills acquisition align with the level of challenge and support provided are necessitated for replenishing conventional structure of schooling. Aiming to explain the satisfying experience, flow theory was created and developed by Csikszentmihalyi (1990) for over forty years, it provides a universal system regardless of styles of activities and participants for evaluating the optimal experience. The flow principles comprise eight elements including availability, concentration, clear goal, feedback, control, engagement, immersion, and simulation; moreover, challenge and corresponding achieved skill are indispensable (Csikszentmihalyi, 1990). The notion is extended by Sweetser and Wyeth (2005), who develop an adaptive model GameFlow to evaluate the enjoyment of players by which specific elements such as concentration, challenge, player skills, control, clear goals, feedback, immersion, and social interaction are examined by detailed criteria. The GameFlow theory establishes on the basis that video games strive to prolong the flow experience, hence a balance of challenge and ability is obliged to maintain (Chen, 2007).

The availability of the GameFlow model by Sweetser and Wyeth (2005) has been endorsed by Bernhaupt et al. (2007), who assert GameFlow model is a heuristic theory for measuring gaming experience. In a practical aspect, Inal and Cagiltay (2007) employ this model to resolve essential traits of computer games, Fu et al. (2009) elaborate an EGameFlow scale to assess players' enjoyment derived from the GameFlow model.

2.2 Fulfilling educational principles through epistemic video games

Collins and Ferguson (1993) introduce the concepts of epistemic forms and epistemic games that interpret how novel knowledge is constructed and acquired by the structure of games. In the opinion of Collins and Ferguson (1993), scientific investigations into specific phenomena are guided by the fundamental structure supporting known as epistemic forms, meanwhile, these inquiries are specified under rules and strategies which constitute epistemic games. Building on the epistemic structure theory, Shaffer (2006) extends epistemic frames beyond the technical sense to principles of practice involving inquiry establishing, information accumulation, and evaluation, concluding that the entire mechanism concatenates practices and cognitive modalities through simulation realized via virtual gaming.

Coherent to the core pursuit of deep learning implementation by referring to the construction and acquisition of new knowledge via epistemic games practices, Gee (2004) proposes well-established learning principles with what good epistemic video games incorporate to enhance cognition in the process of learning in classrooms. In discussing his principles, Gee (2004) describes how epistemic games realize educational purposes. Gee (2004) emphasizes that the information conveyed in the context provided by good epistemic video games is supposed to meet the exact educational object of school, moreover, adequate time arrangement for guaranteeing maximum memory and availability of information subsequent to the game playing is crucially important. In addition, Gee (2004) promotes "good games" largely due to the interaction enabling players to resolve gradually more complex levels by which expertise is mastered throughout the game cycle, as a result, deep learning for educational purposes is positively motivated in classrooms. In this respect, Shaffer (2006) explains the benefits of immersive participation from an interest-oriented dimension, which deems that the more interested a child is in a topic, the deeper expertise he/she will develop. This theory, named

islands of expertise, reminds us of the usability of epistemic games combining knowledge and educational content. When confronting challenges such as improving the performances of disciplines' grades, the acknowledgment of expertise is simultaneously compiled (Shaffer, 2006).

As a new model encouraging transformation for learning, epistemic games allow students to extend their learning experience beyond the confines of the classroom by organizing their own virtual communities sharing identical values (Shaffer et al., 2005). Their varying contexts yield students the opportunity to explore heterogeneous identities in parasocial experience, in turn, motivations for learning are evoked while experiencing the powerful identities (Shaffer et al., 2005; Gee, 2004).

III. METHODOLOGY

In the present research, the GameFlow model (Sweetser and Wyeth, 2005) is applied to understand to what extent the design practices of Working with Water support improve learning performance with respect to flow experience (see Figure 1).
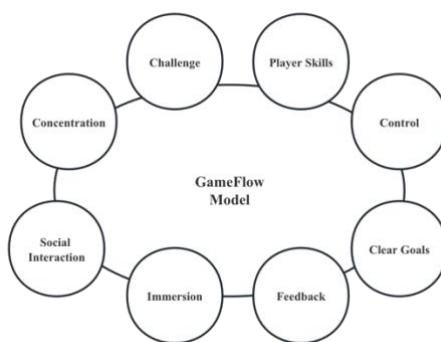
Figure 1: GameFlow experience model

3.1 Case study

Committed to enhancing awareness among students aged 11 to 16 about the management of water resources of the Central Coast Council, the Chaos Theory team designed the educational game Working with Water. This game has been continually rewarded with the Australian Game Developer Awards for Best Serious Game from 2019 to 2021. This game is highly recognized as a consequence of its parallel usability to the central criteria of GameFlow elements.

IV. RESULTS

4.1 Concentration

Working with Water (WW for abbreviation in the following) stimulates players with the combined aesthetic design in the versions of vision and sound (see Figure 2). The semi-realistic casual style featuring cute cartoonish greatly bonds the adolescent students and the game (Rocket Brush Studio, 2022), which at the same time soothes the seriousness of the serious issue the game conveys. The background music simulating the coast implemented by WW constructs an intricate multimedia case that statistically obviously enhances memory in virtual learning (Fassbender et al., 2012).
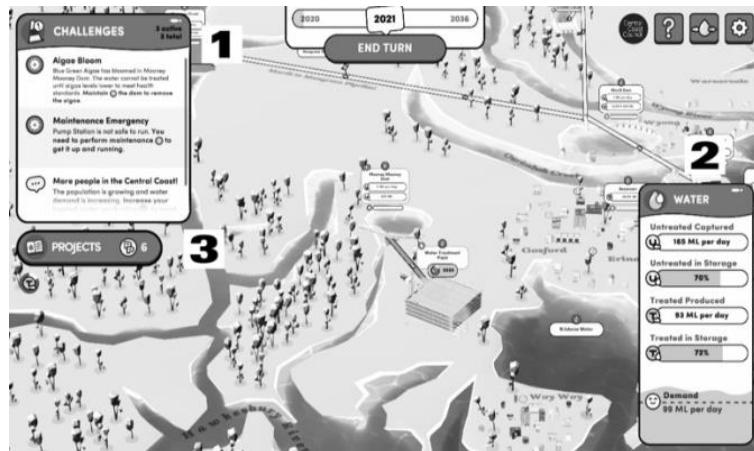
Figure 2: The aesthetic design of WW

Nevertheless, possibly considering the targeted audiences cannot allocate much time to video games, stimuli are limited to overcome a consistent goal of increasing treated water production. Paradoxically, limited stimuli that indicate an identical goal in turn accord with the criteria of concentration, as they shape moderated tasks that perfectly coincide with players' actual cognition system. The stimuli are proved effective, students are focused on exploring the intricate water supply system, aligning with the designers' intention to enhance their level of concentration while learning.

4.2 Challenge

Challenges in WW are comprised of two main aspects: 1. the round-based challenge that dynamically varies depending on the current context, incorporating climatic change such as drought or torrential downpours, maintenance and construction of facilitates, and suddenness occurring along the Central Coast. 2. the underlying task revolves around the resolution of the increasing provision of water. Both of these challenges can be effectively tackled by following the tutorial and evoking strategies that conform to the cognitive flexibility strategies of targeted adolescents.

The demand for water increases per round of the game, which produces the corresponding development of the game difficulty. During this period, taking both increments of skill level and refraining from unnecessary frustration into consideration, WW ensures the balance by introducing challenges that are admitted to the students' expertise.

4.3 Player skills

Adaptive to students aged 11 to 16, WW introduces an engaging cartoon character named Whizzy portrayed upon the water droplet, who guides the students in getting familiar with the interface and tacking with round based challenges providing a comprehensible tutorial throughout the game (see Figure 3).
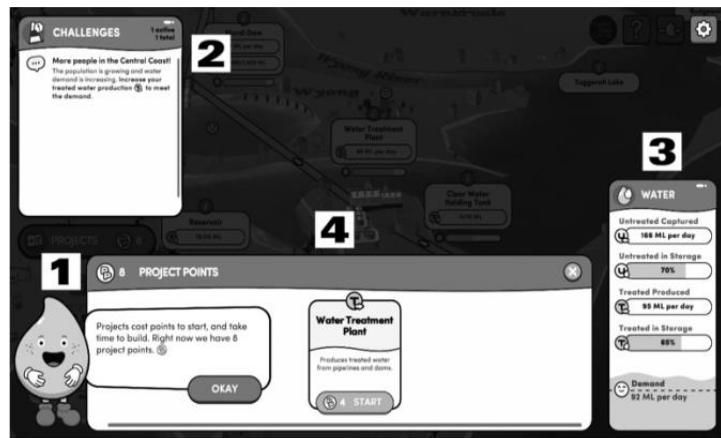
Figure 3: WW exhibits the Central Coast Water Supply System by delivering detailed instructions. (1) Whizzy contextualizes the context and provides explanations for each panel by responding to the students' clicks: (2) challenges of each round (3) actualization of the completion level (4) supportive resources for challenges

The tutorial by Whizzy facilitates the comprehension of water management issues relating to game challenges and practices for solving increasing water demand that resembles reality. Players are taught to operate with the help of concise hints in the challenge panel, their mission is to build up projects that help to overcome challenges. Students' skills are improved with adequate resources equipped with the projects at a moderate pace, which is realized by the demanding construction period during which students are accommodated with academic information presenting the project. Once completing each turn, level-up functional facilities are rewarded which immediately serve for the next turn, players are instantly satisfied and upgrade their knowledge.

4.4 Control

Players are encouraged to domain the whole management of the water system, through allocating the project points proportioned following their personal organization, players in WW identify themselves with the director of water resource management. The interface system authorizes the player to inspect the general view and also zoom in for meticulous inspection by scrolling and moving the mouse, this interaction likewise legitimizes the sense of control over the movements, engagement, and interface manipulation.

In spite of that, WW can be improved by fixing the saving and loading protocol. At present, the historical progress is discarded once the students exit the game, as known that replicated gaming experience is frustrating, a virtual storage space may bring forward better enjoyment by allowing players to continue their progress across game sessions.

On the other hand, WW is relatively supportive in benefiting from committing errors, even if the actual challenge requirements are not satisfied, gentle admonition is displayed by transforming a smiling face into a crying one in the water panel (Figure 3 (3)). Conversely, in case of succeeding in achieving the goal, a smiling face is ready to be retrieved.

WW stands out as a successful serious game for contributions that meet the educational objectives with regard to comprehending the measures maintaining the sustainable development of drinking water, they are trained for further practices with which the world will be better.

Furthermore, multiple combinations of infrastructures make the player's own strategies implementable, the player determines what propels the progress of his/her own project and assesses the usability of it during gameplay.

Enhancing Learning Through Game Flow: A Case Study for Epistemic Game "Working with Water"

4.5 Clear goals

The overriding goal of WW has been advocated in a comprehensive way across the gaming experience (see Figure 2). Notably, the challenge panel (2) keeps alerting that the accelerating population is in great need of water. Besides, what will happen will also be forecasted in the challenge panel.

WW also rightly takes the conformance of the game advance presentation (see Figure 2), by which the clarity of goals is guaranteed by perceiving all the relevant information. Firstly, the challenge panel (1) pended in the upper left of the interface perpetually keeps the players informed of their tasks. Besides, the water panel (2) correlating to the challenge provides additional messages revealing the completion status. Finally, projects panel (3) denotes the resources for sequent movements and interactions that directly determine the result of each round.

4.6 Feedback

In the game, students are allowed to establish their projects by choosing from multiple options of facilities. WW motivates better performance in each round which equals enhanced game skills, afterward, more advanced establishments are unlocked (see Figure 4).
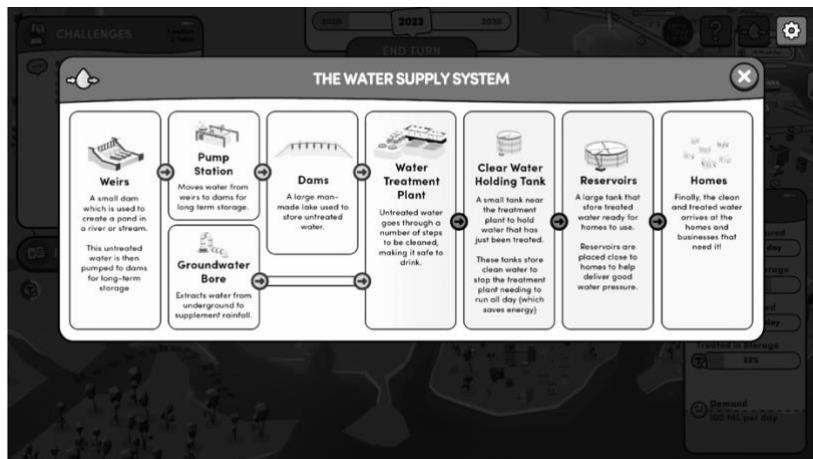
Figure 4: The feedback as a reward system regarding water management

The feedback of WW is immediately redeemed for empowering higher efficiency in the posterior stages of challenges, players are able to check it at any time during the game.

The richness of feedback is combined (see Figure 5), the establishments represent the first modality, and the progress achieved after proceeding turns of games is also visible in the interface, which inspires sustained involvement with games from students' perspectives.
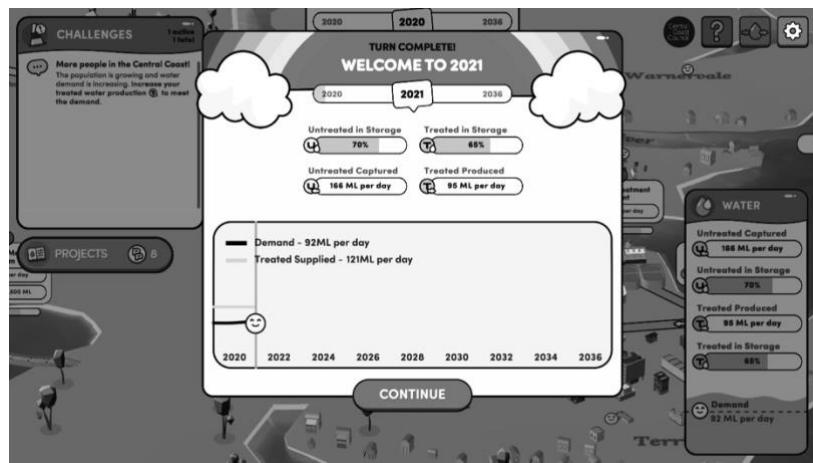
Figure 5: Feedback describing the achievement of each round

4.7 Immersion

Regarding the game experience that makes players engaged, WW relates students to the virtual world exerting the realistic map encompassing water management facilities and the sketch depicting buildings, rivers, and geographic features. The familiarity with the simulation provided simplifies the immersion sense, the game triggers students to feel responsible for dealing with the water deficit, confident in resolving the problem, and personally connected to the fate of Central Coast.

Visceral involvement tightly attaches to concentration, which implies that the sense of reduced worries and perception of reality heightens fluent involvement in the game. WW strives to reach the goal, but due to the prior explanation of limited genre features, an absolute immersion is pending to be realized technically.

4.8 Social interaction

WW is created for single-person, focusing on improving individual's learning and practicing skills. The absence of competition and cooperation between players encourages students to explore and establish strategies on the basis of their knowledge acquired through school and the game independently.

This feature promotes the construction of personal reflective space, accrediting students from 11 to 16 years old more possibilities to enhance their self-organized ability.

V.   CONCLUSION

WW is an online turn-based web strategy game, whose preliminary purpose is to surpass the obstacle the traditional classroom education faced that is brought by COVID-19, whose performance in changing education location from offline to online undoubtedly extends the knowledge transformation mechanism.

The results of the evaluation of WW reveal certain aspects of its linkage to elements including concentration, challenge, player skills, control, clear goals, feedback, immersion, and social interaction, it has been proved that the positive evaluation indicates the usability of WW as been an educational instrument for enhancing learning efficiency.

The study highlights the aesthetic design that contributes to concentration but also to limited stimuli. Challenges that gradually increase in difficulty allow students to develop their skills. The guidance provided by Whizzy and the availability of resources improve players' skills. Control over the water system and the provision of immediate feedback enhance the gaming experience. While immersion is fostered through realistic simulations, social interaction is limited to individual learning.

Nevertheless, a significant flaw is witnessed which relates to the nuance regarding the ranking of enjoyment towards various genres of games. For epistemic games, which weighs more, the knowledge transmission or the flow experience?

The answer is not hard to answer for other genres of games. When modifying the overriding issue, the accuracy of the evaluating model GameFlow is in doubt when applied for educational purposes. This pending curiosity could furnish inquiry for further investigation.

The insights gained from this study intend to give rise to future educational games, further enhancing their effectiveness and impact on student learning outcomes.

REFERENCES

1. Bernhaupt, R., Eckschlager, M., & Tscheligi, M. (2007). Methods for evaluating games. ACE '07: Proceedings of the international conference on Advances in computer entertainment technology. https://doi.org/ 10.1145/ 1255047.1255142

2. Chen, J. (2007). Flow in games (and everything else). Communications of the ACM, 50(4), 31–34. https://doi.org/10.1145/ 1232743.1232769

3. Collins, A. J., & Ferguson, W. (1993). Epistemic forms and Epistemic Games: Structures and Strategies to Guide Inquiry. Educational Psychologist, 28(1), 25–42. https://doi.org/10.1207/s15326985ep2801_3

4. Csikszentmihalyi, M. (1990). Flow: The Psychology of Optimal Experience. Harper Perennial.https://opus4.kobv.de/opus4-Fro mm/frontdoor/index/index/docId/27641

5. Fassbender, E., Richards, D., Bilgin, A., Thompson, W. R., & Heiden, W. (2012). VirSchool: The effect of background music and immersive display systems on memory for facts learned in an educational virtual environment. Computers & Education, 58(1), 490–500. https://doi.org/10.1016/j.comp edu.2011.09.002

6. Fu, F., Su, R., & Yu, S. (2009). EGameFlow: A scale to measure learners' enjoyment of e-learning games. Computers & Education, 52(1), 101–112. https://doi.org/10.1016/j. compedu.2008.07.004

7. Gee, J. C. (2004). What Video Games Have to Teach Us about Learning and Literacy. Journal of Education and Training, 46(4). https://doi.org/10.1108/et.2004.00446dae.0 02

8. Gee, J. P. (2005). Learning by Design: Good Video Games as Learning Machines. E-learning and Digital Media, 2(1), 5– 16. https://doi.org/10.2304/elea.2005.2.1.5

9. Inal, Y., & Cagiltay, K. (2007). Flow experiences of children in an interactive social game environment. British Journal of Educational Technology, 38(3), 455–464. https://doi.org/10.1111/j.1467-8535.2007.007 09.x Parviainen, J., Koski, A., & Torkkola, S. (2021). 'Building a Ship while Sailing It.' Epistemic Humility and the Temporality of Non-knowledge in Political Decision-making on COVID-19. Social Epistemology, 35(3), 232–244.https://doi.org/10.1080/02691728. 2021.1882610

10. Rocket Brush Studio. (2022, April). How to Choose The Art Style That Fits Your Game. Rocket Brush Studio. https://rocketbrush. com/blog/how-to-choose-art-style-for-your-g ame

11. Shaffer, D. W. (2006). Epistemic frames for epistemic games. Computers & Education, 46(3), 223–234. https://doi.org/10.1016/j. com pedu.2005.11.003

12. Shaffer, D. W., Squire, K., Halverson, R., & Gee, J. C. (2005). Video Games and the Future of Learning. Phi Delta Kappan, 87(2), 105–111.https://doi.org/10.1177/0031721705 08700205

13. Sweetser, P., & Wyeth, P. (2005). GameFlow. Computers in Entertainment, 3(3), 3. https://doi.org/10.1145/1077246.1077253

14. Vorderer, P., Klimmt, C., & Ritterfeld, U. (2004). Enjoyment: At the Heart of Media Entertainment. Communication Theory, 14(4), 388–408. https://doi.org/10.1111/ j.1468-2885. 2004.tb00321.x

Smart Safety Solutions: Real-Time SMS Alerts for Gas Leakage and Fire Detection using IOT

Ebole Alpha Friday, Tiamiyu Olalekan Sorlihu & Aremu I Abiodun

Lagos State University

ABSTRACT

Security issues are becoming increasingly important in today's environment, necessitating heightened attention to detail due to the rising dangers of infiltration and hazardous situations. Gas leaks and fires are among the most urgent hazards to residential and commercial safety as they may cause a devastating loss of life and property. Conventional alarm systems that just use sound signals frequently fail to guarantee prompt human reaction, particularly in situations where inhabitants are not present. Using Internet of Things (IoT) devices that are coupled with GSM (Global System for Mobile Communications) technology, this study suggests a real-time gas leak and fire detection system that sends timely SMS notifications. To identify anomalies, the system uses an Atmega644P microprocessor that is interfaced with gas and fire sensors, relays, and buzzers. Through the SIM548C GSM module, which notifies pre-designated emergency contacts via SMS in real time, the system instantly sounds an alarm in the event of a gas leak or fire. This rapid communication mechanism ensures faster response and mitigates potential damage. The increasing importance of intelligent, real-time safety systems in tackling contemporary security issues is highlighted by this review.

Keywords: gas leaks and fires, Internet of Things and Global System for Mobile Communications.

Classification: FOR Code: TK7895.E42

Language: English

Smart Safety Solutions: Real-Time SMS Alerts for Gas Leakage and Fire Detection using IOT

Ebole Alpha Friday[α], Tiamiyu Olalekan Sorlihu[σ] & Aremu I Abiodun[ρ]

ABSTRACT

Security issues are becoming increasingly important in today's environment, necessitating heightened attention to detail due to the rising dangers of infiltration and hazardous situations. Gas leaks and fires are among the most urgent hazards to residential and commercial safety as they may cause a devastating loss of life and property. Conventional alarm systems that just use sound signals frequently fail to guarantee prompt human reaction, particularly in situations where inhabitants are not present. Using Internet of Things (IoT) devices that are coupled with GSM (Global System for Mobile Communications) technology, this study suggests a real-time gas leak and fire detection system that sends timely SMS notifications. To identify anomalies, the system uses an Atmega644P microprocessor that is interfaced with gas and fire sensors, relays, and buzzers. Through the SIM548C GSM module, which notifies pre-designated emergency contacts via SMS in real time, the system instantly sounds an alarm in the event of a gas leak or fire. This rapid communication mechanism ensures faster response and mitigates potential damage. The increasing importance of intelligent, real-time safety systems in tackling contemporary security issues is highlighted by this review.

Keywords: gas leaks and fires, Internet of Things and Global System for Mobile Communications.

*Author*α σ ρ: Department of Computer Science, College of Basic Sciences, Lagos State University of Science and Technology, Lagos, Nigeria.

I. INTRODUCTION

Among the most destructive risks that both residential and commercial buildings must deal with are gas leaks and fires. In addition to posing major risks to human life, these occurrences have the potential to cause significant property damage, environmental contamination, and financial loss. The World Health Organization (WHO, 2022) states that gas leaks and other forms of indoor air pollution are major causes of health issues and deaths annually. According to the National Fire Protection Association [NFPA], 2023, fire outbreaks cause billions of dollars' worth of damage and hundreds of fatalities per year.

Conventional safety devices, like gas leak detectors or smoke alarms, frequently use sound signals to warn people of danger. These systems can have limitations, though, especially when there are a lot of noise around or when inhabitants are not there or are sleeping. Disaster risk increases when emergency action is delayed due to these systems' incapacity to instantly alert external parties (Al-Khateeb & Saadeh, 2020). Modern safety systems are moving toward intelligent, networked technology to overcome these constraints. The SMS-based gas leak and fire alarm detection system is one example of an invention that uses wireless communication and sensor technologies to deliver real-time notifications. When dangerous situations are identified, the system may immediately send SMS alerts to pre-specified phone numbers by using GSM technology. This guarantees that vital notifications may reach building managers, emergency services, or homeowners even when no one is physically there, allowing for quick action (Kumar et al., 2021). For instantaneous local and remote notifications, the suggested system combines high-sensitivity gas and flame sensors with an Atmega644P microprocessor and a SIM548C GSM module, backed by relays and buzzers. The technology immediately sends SMS

notifications to numerous recipients as soon as a fire or gas leak is detected, greatly enhancing emergency awareness and reaction times.

This system is perfect for deployment in a variety of locations, including office buildings, industrial facilities, and private dwellings, since it is affordable, scalable, and easy to use. Additionally, even in contexts with limited resources, its use of off-the-shelf components guarantees maintainability and simplicity of deployment. This research intends to minimize damage and casualties from gas and fire-related incidents, decrease emergency response times, and create a better living and working environment by putting such an IoT-based alert system into place.

2.1 Problem Statement

The possibility of gas leaks and fire occurrences presents serious risks to home and company safety in today's quickly changing metropolitan landscapes. Conventional detection systems frequently have poor communication capabilities, which causes delays in emergency responses and raises the risk of disastrous consequences. Injuries, deaths, and property damage may result from evacuation attempts and emergency interventions being hampered by the lack of real-time notifications.

The goal of this project is to create a Smart Safety Solution that uses Internet of Things devices to deliver real-time SMS warnings for fire and gas leak detection. The system will provide instant communication to specified emergency contacts by combining high-sensitivity sensors and GSM technology, enabling prompt response and enhancing general safety. Through improved detection accuracy, fewer false alarms, and a scalable, user-friendly interface, the suggested approach aims to overcome the drawbacks of traditional systems. The ultimate goal of this project is to provide a strong safety framework that considerably lowers the risks related to fire dangers and gas leaks.

1.2 Scope

The scope of the Smart Safety Solution includes deploying Internet of Things (IoT) sensors to

monitor gas leaks and fire threats in real-time, sending instant SMS warnings to specified emergency contacts for prompt action. Its advantages include an easy-to-use interface, scalability for different contexts, and integration with pre-existing alarm systems. The possibility of sensor errors, reliance on cellular network availability for SMS notifications, and upfront setup expenses, which can put off some customers, are some drawbacks. Furthermore, to guarantee maximum performance, constant maintenance is necessary, and user setup errors may result in ineffective alarms, jeopardizing safety.

1.3 Limitations of the Study

The accuracy of sensors, which can be impacted by external variables and result in missed detections or false warnings, is one of the limitations of the Smart Safety Solution research. Furthermore, because the system depends on cellular network availability to provide SMS messages, communication may be delayed or fail in places with weak connections. Widespread adoption may be hampered by cost issues, especially for low-income homes, and users lacking technical knowledge may find it difficult to maintain and calibrate sensors on a regular basis. Errors in user settings may also reduce the efficacy of alerts, and the system's performance in bigger or more complicated contexts may necessitate extra infrastructure. Lastly, strong security measures are required to safeguard user data from unwanted access due to data privacy issues.

1.4 Objectives

The primary objectives of the proposed SMS-based gas leakage and fire alarm detection system are:

i. Enhance Safety through Timely Detection:

ii. Real-Time Notification:

iii. Integration with Existing Systems:

iv. Scalability and Flexibility:

v. Reliability and Accuracy:

II. LITERATURE REVIEW

2.1 Introduction

Several technologies are integrated in the creation of an SMS-based gas leak and fire alarm detection system to improve safety in commercial, industrial, and residential settings. This study of the literature looks at recent research and developments in fire alarm systems, SMS-based warning systems, and gas detection technologies. Finding technological deficiencies and laying the groundwork for the suggested system that guarantees real-time hazard warnings and reaction are the objectives.

2.2 Gas Leakage Detection Systems

Gas leak detection systems play a critical role in preventing accidents caused by hazardous and combustible gases such as carbon monoxide (CO), propane (C_3H_8), and methane (CH_4), with researchers exploring various sensor technologies and system architectures to enhance reliability. The MQ-series sensors, including MQ-2, MQ-5, and MQ-9, are widely used due to their affordability and sensitivity to multiple toxic and flammable gases; they detect leaks by converting changes in electrical resistance—triggered by gas exposure—into analog signals for processing (Sharma & Agrawal, 2014). To expand monitoring coverage and ensure reliable detection across large areas, wireless sensor networks (WSNs) are employed, offering real-time data sensing and transmission ideal for industrial safety applications (Yick, Mukherjee, & Ghosal, 2008). Furthermore, integrating Internet of Things (IoT) platforms transforms gas detection systems into intelligent networks, enabling real-time alerts, visual analytics, and remote decision-making through mobile apps and cloud dashboards (Zhao, Li, & Da Xu, 2018).

2.3 Fire Alarm Detection System

The evolution of fire alarm detection systems has integrated various advanced sensors to improve early fire detection and response. Key among these are smoke detectors, which come in two main types: photoelectric detectors that are more effective at sensing smouldering fires, and ionization detectors that are more responsive to flaming fires, as noted by Bukowski et al. (2008). Heat detectors, which trigger alarms based on rapid temperature increases or fixed thresholds, are preferred in environments prone to dust or smoke that could trigger false alarms in optical systems (Jones, 2007). Additionally, flame sensors detect the ultraviolet (UV) and infrared (IR) radiation emitted by flames, making them highly suitable for high-risk areas such as fuel stations and industrial sites due to their rapid response capabilities (Kumar, Narayan, & Singh, 2015).

2.4 SMS-Based Notification Systems

GSM modules play a vital role in SMS-based alert systems by enabling real-time notifications even in the absence of internet connectivity. Modules such as the SIM800L and SIM900 are widely adopted due to their low power requirements and ease of integration with microcontrollers, supporting functions like GPRS data transfer, voice calls, and text messaging (Rahman, Hossain, & Rahman, 2016). SMS alerts are considered highly reliable during emergencies, as they do not depend on mobile apps or Wi-Fi infrastructure; Kumar and Sinha (2011) highlighted their effectiveness in disaster-prone areas where internet-based systems often failed. Furthermore, integrating GSM modules with IoT platforms allows systems to transmit sensor data to the cloud while sending SMS alerts for immediate human intervention, enhancing both system redundancy and responsiveness (Zhu, Leung, & Shu, 2018).

2.5 Combined Systems for Gas and Fire Detection

Multi-sensor systems that integrate gas and fire detection technologies significantly enhance safety coverage by providing more accurate and reliable threat identification. These systems combine various sensors—such as MQ-series gas sensors, smoke detectors, flame sensors, and heat detectors—with microcontroller units (MCUs) that analyze input data to determine the appropriate alert response (Lee & Park, 2016). The integration of GSM modules allows for real-time notifications through both local alarms

(e.g., buzzers) and remote SMS alerts to users and emergency services, ensuring prompt action in critical situations (Ahmed, Rahman, & Khan, 2017). Additionally, these systems are designed with flexible user interfaces or mobile applications that allow users to configure alarm settings, sensor thresholds, and contact numbers, making them adaptable to different safety needs (Hussain, Khan, & Rahim, 2015).

III. SYSTEM DESIGN AND ARCHITECTURE

The system design of the SMS-based gas leakage and fire alarm detection system incorporates multiple hardware components integrated to achieve real-time detection and alert capabilities. The design emphasizes accuracy, responsiveness, and reliability through carefully selected sensors and microcontroller interfacing.

3.1 Components

Gas Detectors: Gas sensors such as MQ-2, MQ-5, and MQ-9 are employed to detect the presence of combustible and toxic gases like methane, propane, and carbon monoxide. These sensors work by changing their internal resistance in response to gas concentration, generating an analog voltage output [1].

Fire Detectors: Smoke, heat, and flame sensors are used to detect different fire indicators. Smoke detectors operate on photoelectric or ionization principles, heat sensors detect temperature rises, and flame sensors respond to ultraviolet (UV) or infrared (IR) emissions [2].

Microcontroller Unit (MCU): The central control is handled by a microcontroller such as Arduino Uno or ESP32, which processes input signals from sensors and controls output responses, including SMS alerts and buzzer activation [3].

GSM Module: A SIM800L or SIM900 GSM module is integrated to send SMS notifications to predefined phone numbers. These modules support standard AT commands for SMS transmission over 2G networks [4].

Power Supply: The system is powered by a 5V or 12V DC supply with optional battery backup to ensure continuous operation during power outages.

User Interface: A basic interface for setting recipient phone numbers and system reset functions may be included using buttons, an LCD, or serial input [5].

3.2 System Workflow

1. Detection: The sensors continuously monitor environmental conditions. If gas leakage or fire conditions are detected, the sensor outputs change accordingly.

2. Processing: The MCU receives the analog/digital signals and compares them against pre-defined thresholds.

3. Notification: If conditions exceed safe levels, the MCU activates the GSM module to transmit an SMS alert.

4. Alerting: The system can also trigger a buzzer, turn on LED indicators, and display messages on an LCD screen to notify locally.

3.3 Detailed System Design

3.3.1 Circuit Design

The circuit design for the SMS-based gas leakage and fire alarm detection system integrates various components to detect hazardous environmental conditions and initiate appropriate response mechanisms. The design prioritizes safety, modularity, and ease of implementation using widely available hardware components.
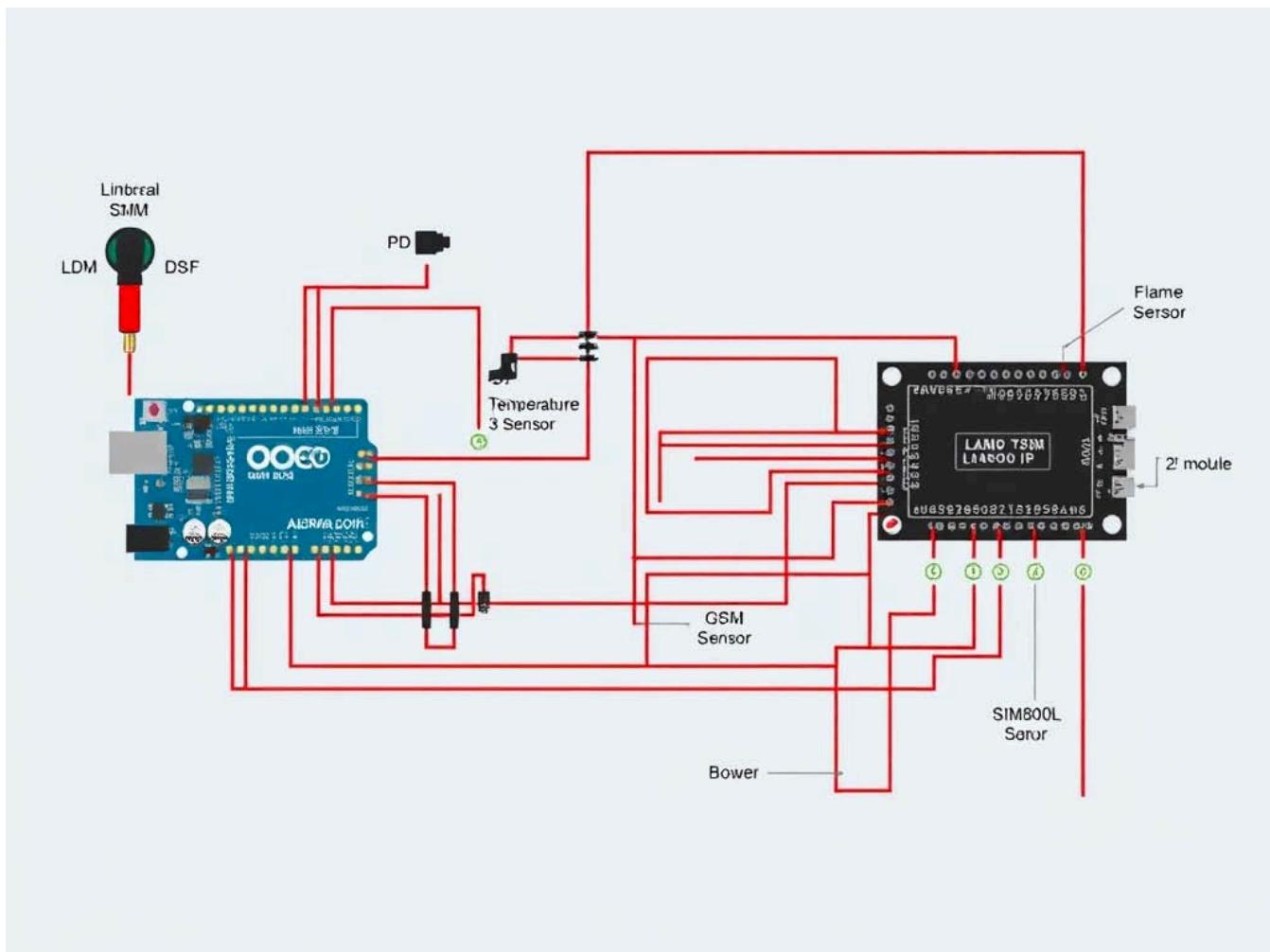
Figure 3.1: Circuit Diagram of Real-Time SMS-Based Gas Leakage and Fire Alarm Detection System Using IOE Devices

Overview

The system consists of three core functional blocks:

1. Sensing Unit – Comprising gas and fire detectors to monitor environmental conditions.
2. Control Unit – A microcontroller (e.g., Arduino Uno or ESP32) processes sensor signals and manages outputs.
3. Alert and Notification Unit – Includes a buzzer for local alarms and a GSM module (SIM800L/SIM900) for remote SMS alerts.

An optional user interface consisting of an LCD and LED indicators provides local system status updates.

Component List

S/N	Component	Description
1	MQ-2 / MQ-5 / MQ-9	Gas sensors for detecting methane, LPG, and carbon monoxide
2	Smoke Sensor	Detects presence of smoke (fire indicator)
3	Heat Sensor	Detects abnormal temperature rise

S/N	Component	Description
4	Flame Sensor	Detects flame using IR/UV light
5	Arduino Uno / ESP32	Microcontroller for control logic
6	SIM800L / SIM900	GSM module for sending SMS alerts
7	16x2 LCD Display (optional)	Displays system status and alerts
8	Buzzer	Emits sound in case of hazard
9	LEDs (optional)	Visual indication for gas leak or fire
10	Resistors & Capacitors	Supporting passive components
11	Power Supply (5V/12V)	Main power source with optional battery backup

3.4 Functional Design Description

The SMS-based gas leakage and fire alarm detection system utilizes a microcontroller, such as an Arduino, to monitor environmental conditions through various sensors, including a gas sensor for detecting harmful gases, a temperature sensor for monitoring heat levels, and a flame sensor for fire detection. When any of these sensors detect unsafe conditions, the system triggers an alarm using a buzzer and LED indicators, while simultaneously sending an alert via SMS through a GSM module like the SIM800L. This system is designed for safety and quick response, making it essential in environments where gas leaks or fires pose significant risks.

3.5 Design Considerations

Here's a concise overview of the key considerations for your SMS-based gas leakage and fire alarm detection system:

1. Power Regulation: Ensure a stable 5V supply, particularly for the GSM module, which is sensitive to voltage fluctuations.
2. Isolation: Use opto-isolators or separate power supplies for high-power modules or relays to prevent interference.
3. Noise Reduction: Incorporate decoupling capacitors near the VCC lines of sensors and the GSM module to minimize noise and enhance stability.
4. Sensor Calibration: MQ sensors should be pre-heated and calibrated in a clean environment to ensure accurate detection of gas levels.

3.3.2 Circuit Connections
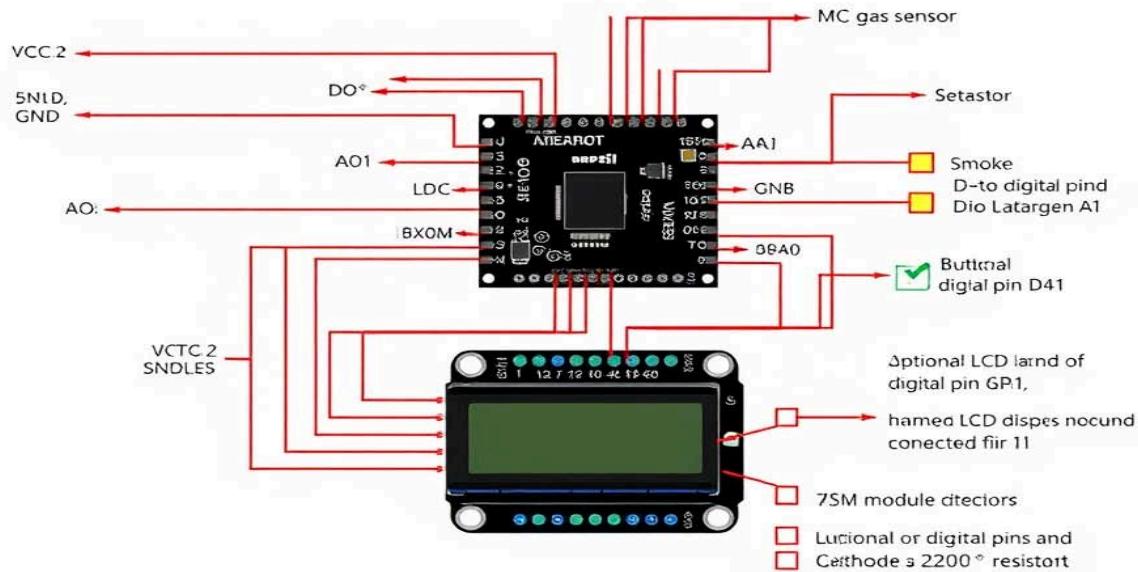
Figure 3.2: Circuit Connection of Real-Time SMS-Based Gas Leakage and Fire Alarm Detection System Using IOE Devices

i. Gas Sensor (e.g., MQ-2)

- VCC → 5V (MCU)
- GND → GND (MCU)
- A0 → Analog input (e.g., A0)

ii. Smoke Detector (Digital Output)

- VCC → 5V
- GND → GND
- DO → Digital pin (e.g., D2)

iii. Heat Sensor

- VCC → 5V
- GND → GND
- AO → Analog pin (e.g., A1)

iv. Flame Sensor (Digital Output)

- VCC → 5V
- GND → GND

- DO → Digital pin (e.g., D3)

v. GSM Module (SIM800L)

- VCC → 5V

- GND → GND

- TX → MCU RX (e.g., D10)

- RX → MCU TX (e.g., D11)

vi. Buzzer

-

o → Digital pin (e.g., D4)

- – → GND

vii. LCD Display (16x2) – Optional

- Connected via I2C/SPI or direct digital pins

viii. LED Indicators – Optional

- Anode → Digital pins (e.g., D5, D6)

- Cathode → GND through 220Ω resistor

Below is a simple schematic representation:
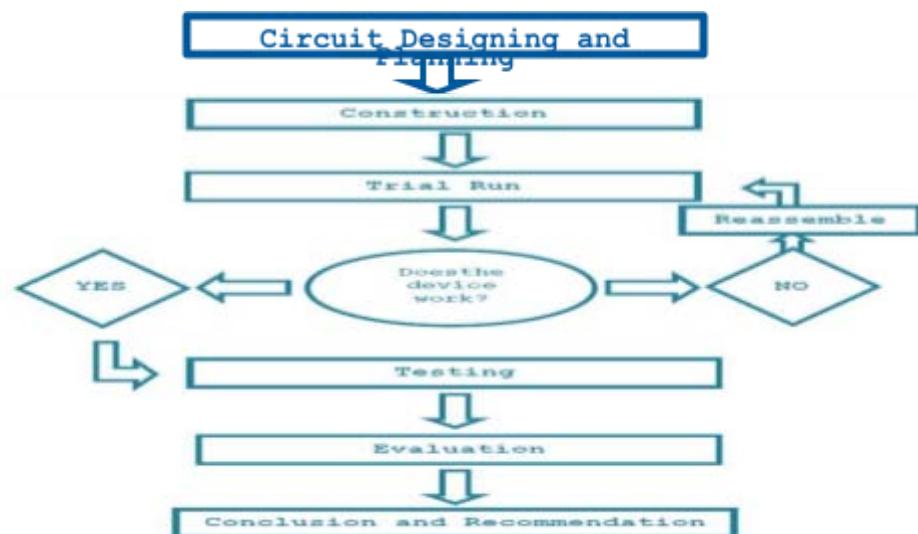
Figure 3.3: Flow chart of Real Time SMS-Based Gas Leakage and Fire Alarm Detection System Using IOE Devices
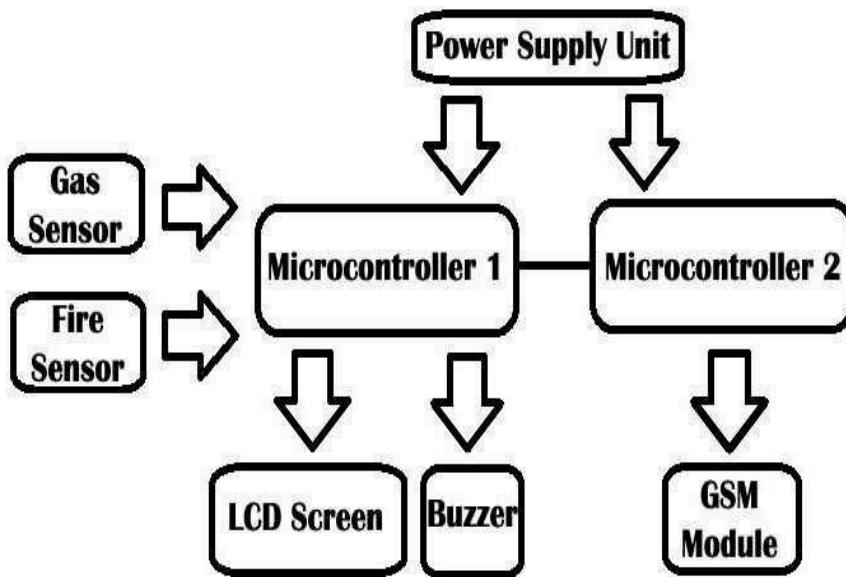
Figure 3.4: Block diagram of a Real Time SMS-Based Gas Leakage and Fire Alarm Detection System Using IOE Devices

Arduino Code

```
#include <SoftwareSerial.h>
// GSM module connected to pins 7 (TX) and 8 (RX)
SoftwareSerial gsm(7, 8);
const int gasSensorPin = A0;    // MQ-2 Gas sensor connected to A0
const int flameSensorPin = 2;   // Flame sensor connected to digital pin 2
const int buzzerPin = 3;  // Buzzer connected to digital pin 3// Thresholds
const int gasThreshold = 300;   // Adjust as needed
const int flame Threshold = LOW;  // Flame sensor gives LOW when fire is detected
bool gasAlertSent = false;
bool flameAlertSent = false;
void setup() {
 pinMode(gasSensorPin, INPUT);
 pinMode(flameSensorPin, INPUT);
 pinMode(buzzerPin, OUTPUT);
 Serial.begin(9600);
 gsm.begin(9600);
 delay(1000);
 Serial.println("System Initialized");}
void loop() {
int gasValue = analogRead(gasSensorPin);
int flameValue = digitalRead(flame Sensor Pin);
```

```
Serial.print("Gas: ");
Serial.print(gasValue);
Serial.print(" | Flame: ");
Serial.println(flameValue);
// Gas leak detection
if (gasValue > gasThreshold && !gasAlertSent) {
sendSMS("WARNING: Gas leak detected!");
 digitalWrite(buzzerPin, HIGH);
 gasAlertSent = true;
 } else if (gasValue <= gasThreshold) {
 gasAlertSent = false;
 digitalWrite(buzzerPin, LOW);
 }
 // Flame detection
 if (flameValue == flameThreshold && !flameAlertSent) {
 sendSMS("WARNING: Fire detected!");
 digitalWrite(buzzerPin, HIGH);
 flameAlertSent = true;
 } else if (flameValue != flameThreshold) {
 flameAlertSent = false;
 digitalWrite(buzzerPin, LOW);}
 delay(1000); // Delay between readings}
void sendSMS(String message) {
 gsm.println("AT+CMGF=1"); // Set GSM to text mode
 delay(1000);
 gsm.println("AT+CMGS=\"+234XXXXXXXXXX\""); // Replace with your phone number
 delay(1000);
 gsm.print(message);
 delay(500);
 gsm.write(26); // ASCII code for Ctrl+Z to send message
 delay(3000);
}
```

Explanation

- Gas Sensors (MQ-2, MQ-5, MQ-9): These sensors detect gas leaks and output analog signals proportional to the gas concentration. The analog signals are read by the MCU.

- Fire Sensors (Smoke, Heat, Flame): These sensors detect various fire indicators and send digital signals to the MCU.

- Microcontroller (MCU): The central unit that processes sensor data, checks thresholds, and triggers alerts.
- GSM Module: Used to send SMS alerts. The MCU communicates with the GSM module using serial communication (TX/RX).
- LCD Display (Optional): Shows system status and sensor readings.

This setup provides a comprehensive monitoring system for gas leaks and fire incidents, ensuring that alerts are sent out immediately via SMS and locally through buzzers and LEDs.

3.3 Communication Protocol

- Sensor to MCU: Sensors communicate with the MCU using analog or digital signals, which the MCU processes to determine the presence of gas leaks or fire.
- MCU to GSM Module: The MCU uses serial communication to send commands to the GSM module, instructing it to send SMS messages.
- SMS Notification: The GSM module sends SMS notifications to the configured phone numbers, ensuring that recipients are promptly informed of any incidents.

IV.   IMPLEMENTATION PLAN

The implementation of the SMS-based gas leakage and fire alarm detection system follows a structured, multi-phase approach designed to ensure a robust, reliable, and user-friendly solution. Each phase addresses a critical aspect of system development and deployment.

4.1 Phase 1: Planning and Requirements Gathering

This phase establishes a solid foundation for the system design and deployment by conducting a thorough assessment of the environment where the system will be implemented, such as kitchens, factories, fuel depots, or laboratories. It involves selecting appropriate gas detectors, like the MQ-2 for LPG, MQ-6 for propane, or MQ-135 for air quality, and fire detectors, including flame and temperature sensors, tailored to the specific risks of the environment. Additionally, it requires compiling a list of emergency contact numbers,

such as property owners, fire departments, and security personnel, which will be pre-programmed into the system to ensure timely SMS alerts in case of emergencies.

4.2 Phase 2: System Design and Prototyping

This phase centers on constructing the system's core through design and prototype development. It begins with creating a circuit schematic that integrates essential components, including the microcontroller (such as NodeMCU or Arduino), GSM module (like the SIM800L), gas and flame sensors, buzzer, and relay. Following the circuit design, a compact and practical prototype is assembled using breadboards or printed circuit boards (PCBs). The final step involves firmware development, where the microcontroller is programmed to read sensor data, detect hazardous thresholds for gas and fire, send AT commands to the GSM module for SMS alerts, and activate alarms and relays upon detection, ensuring a responsive and functional safety system.

4.3 Phase 3: Testing and Calibration

This phase is critical for ensuring that the system performs accurately and reliably across various conditions. It begins with controlled testing, where gas leaks and flame scenarios are simulated in a safe environment to evaluate the system's responsiveness and accuracy. Sensor calibration follows, adjusting sensitivity levels to minimize false positives and enhance detection precision. Finally, SMS validation is conducted to confirm that alerts are sent promptly, formatted correctly, and successfully reach the designated recipients, ensuring effective communication during emergencies.

4.4 Phase 4: Deployment and Training

Once verified, the system is deployed in the actual environment, accompanied by comprehensive user training. The installation process involves securely mounting sensors and the controller in critical areas, such as gas pipes and stove locations. Training sessions educate users on essential aspects, including system operation, alarm response procedures, updating contact

numbers, and performing regular system checks and resets. To ensure preparedness, emergency drills are conducted, allowing users to practice their responses and evaluate the system's efficiency during simulated emergencies, fostering confidence and readiness in real situations.

4.5 Phase 5: Maintenance and Support

To ensure long-term effectiveness, a comprehensive maintenance and support framework is established. This includes routine maintenance, where periodic checks are scheduled to clean, test, or replace sensors and verify GSM functionality. Additionally, system updates are conducted to upgrade firmware as needed, enhancing features and improving reliability. Support services are also provided to assist users with troubleshooting, configuration, and component replacements, ensuring the system remains operational and effective over time.

4.6 Benefits of the Proposed System

The system brings together IoT, embedded systems, and GSM technology to create a high-impact safety solution with multiple benefits. The system offers immediate notification through real-time SMS alerts to emergency contacts upon detecting gas or fire, enabling rapid intervention to minimize hazards. It enhances safety with early detection capabilities, increasing the chances of preventing injuries and catastrophic damage. Cost-effective by utilizing affordable components like Arduino and GSM modules, it incurs minimal overhead, making it sustainable for households and small businesses. Its scalability allows for adaptable coverage in larger buildings or industrial sites, while user-friendly operation ensures easy installation and configurable settings. With reliable detection from high-sensitivity sensors and robust engineering to reduce false alarms, the system can integrate with existing alarm systems and smart home technologies. Additionally, it supports emergency preparedness through regular drills and provides dependable communication via SMS, even during internet outages or power failures, ensuring comprehensive safety.

V. CONCLUSION, RECOMMENDATION AND CONTRIBUTION TO KNOWLEDGE

This indicates significant advancements in gas leakage and fire detection technologies, emphasizing the importance of integrating multiple sensors and real-time notification systems. The proposed SMS-based gas leakage and fire alarm detection system builds on these advancements, leveraging affordable and reliable components to provide enhanced safety through timely alerts and comprehensive monitoring. This approach will ensure that critical information reaches the right people quickly, facilitating prompt action and potentially preventing significant harm.

Implementing an SMS-based gas leakage and fire alarm detection system will offer a robust solution for real-time incident detection and notification. By integrating reliable sensors with GSM technology, this system will ensure immediate awareness and facilitate quicker response times, potentially saving lives and reducing property damage. The proposed system is cost-effective, scalable, and user-friendly, making it suitable for a wide range of applications.

5.1 Recommendation

It is highly advised that residences, labs, and industrial facilities install a Real-Time SMS-Based Gas Leakage and Fire Alarm Detection System employing IoT devices as a preventative safety measure. This system detects dangerous gas leaks or fire breakouts and instantly sends SMS notifications to authorized persons or emergency responders using gas and flame sensors that are connected to IoT microcontrollers (such as Arduino or ESP32) and GSM modules. It ensures quick reaction and reduces any harm by operating in real time, without requiring internet access, and offering both local alerts and remote notifications. It is a sensible option for improving safety in areas with significant fire and gas threats because to its affordability, scalability, and efficacy.

5.2 Contribution to knowledge

This research advances knowledge by showcasing a creative way to use IoT and GSM technology to solve important safety issues in real-time fire and gas leak monitoring. This method guarantees instant, location-independent SMS notifications, even in places without internet connection, in contrast to traditional alarm systems that only use sound or internet connectivity. It provides an affordable, scalable, and energy-efficient solution that can be used in both commercial and residential settings. A useful resource for next studies and advancements in smart safety and Internet of Things-based emergency response technologies, the project also contributes to the practical knowledge of sensor calibration, microcontroller programming, and real-time warning systems.

REFERENCES

1. Ahmed, M., Rahman, M. A., & Uddin, M. (2020). *IoT-based smart gas leakage detection system with real-time notification*. International Journal of Scientific & Engineering Research, 11(6), 128–134.

2. Kumar, V., & Sahu, M. (2018). *Fire and gas leakage detection system using IoT*. International Journal of Computer Applications, 180(43), 1–4. https://doi.Org/10.5120/ijca2018917356

3. Patil, D. D., & Shinde, A. R. (2017). *GSM based gas leakage detection system using Arduino*. International Research Journal of Engineering and Technology (IRJET), 4(6), 2611–2614.

4. Sharma, N., & Tripathi, R. C. (2019). *Development of IoT-based fire and gas detection system*. Proceedings of the International Conference on Computing, Communication and Automation (ICCCA), 1–5. https://doi.org/10.1109/CCAA.2019.00012

5. MQ-2 Gas Sensor Datasheet. (n.d.). *Components101*. Retrieved from https://components101.com/sensors/mq2-gas-sensor

6. SIM800L GSM Module Datasheet. (n.d.). *SIMCom Wireless Solutions*. Retrieved from https://cdn.sparkfun.com/datasheets/Cellular/GSM_SIM800L.pdf

7. Arduino. (n.d.). *Arduino Uno Rev3*. Retrieved from https://store.arduino.cc/products/arduino-uno-rev3

8. Balaji, N., & Sundararajan, M. (2018). *A review on gas leakage detection and smart alerting system using IoT*. International Journal of Engineering & Technology, 7(2.8), 166–169.

9. Basha, S. M., & Ravi, B. (2019). *Design and implementation of smart LPG gas detection and alert system using IoT*. International Journal of Scientific Research in Computer Science, Engineering and Information Technology, 5(2), 102–108.

10. Manikandan, R., & Kumar, V. (2017). *Smart fire alert system using Arduino and GSM module*. International Journal of Advanced Research in Electrical, Electronics and Instrumentation Engineering, 6(5), 3735–3739.

11. Chaitanya, M. A., & Patil, S. R. (2020). *IoT based fire detection and notification system using GSM module*. Journal of Emerging Technologies and Innovative Research (JETIR), 7(3), 591–595.

12. Dursun, D., & Ozdenizci, B. (2019). *Internet of Things (IoT) for fire safety and gas leakage detection*. In Proceedings of the 7th International Symposium on Digital Forensics and Security (ISDFS), 1–5. https://doi.org/10.1109/ISDFS.2019.8757544

London Journal of Research in Computer Science & Technology

Great Britain Journal Press Membership

For Authors, subscribers, Boards and organizations

Great Britain Journals Press membership is an elite community of scholars, researchers, scientists, profess-sionals and institutions associated with all the major disciplines. Great Britain memberships are for indivi - duals, research institutions, and universities. Authors, subscribers, Editorial Board members, Advisory Board members, and organizations are all part of member network.

Read more and apply for membership here:
https://journalspress.com/journals/membership

For Authors

For Institutions

For Subscribers

Author Membership provide access to scientific innovation, next generation tools, access to conferences/seminars/ symposiums/webinars, networking opportunities, and privileged benefits. Authors may submit research manuscript or paper without being an existing member of GBJP. Once a non-member author submits a research paper he/she becomes a part of "Provisional Author Membership".

Society flourish when two institutions Come together." Organizations, research institutes, and universities can join GBJP Subscription member-shipor privileged "Fellow Membership" membership facilitating researchers to publish their work with us, become peer reviewers and join us on Advisory Board.

Subscribe to distinguished STM (scientific, technical, and medical) publisher. Subscription member-ship is available for individuals universities and institutions (print & online). Subscribers can access journals from our libraries, published in different formats like Printed Hardcopy, Interactive PDFs, EPUBs, eBooks, indexable documents and the author managed dynamic live web page articles, LaTeX, PDFs etc.

GO GREEN AND HELP
SAVE THE ENVIRONMENT

JOURNAL AVAILABLE IN

PRINTED VERSION, INTERACTIVE PDFS, EPUBS, EBOOKS, INDEXABLE
DOCUMENTS AND THE AUTHOR MANAGED DYNAMIC LIVE WEB PAGE
ARTICLES, LATEX, PDFS, RESTRUCTURED TEXT, TEXTILE, HTML, DOCBOOK,
MEDIAWIKI MARKUP, TWIKI MARKUP, OPML, EMACS ORG-MODE & OTHER

support@journalspress.com
www.journalspress.com

*THIS JOURNAL SUPPORT AUGMENTED REALITY APPS AND SOFTWARES